

TECHNISCHE UNIVERSITÄT MÜNCHEN

Ingenieur fakultät Bau Geo Umwelt

Engineering Risk Analysis Group

Time-dependent Probabilistic Assessment of Rainfall-induced Slope Failure

Ji Yuan

Vollständiger Abdruck der von der Ingenieur fakultät Bau Geo Umwelt der Technischen Universität München zur Erlangung des akademischen Grades eines

Doktor-Ingenieurs (Dr.-Ing.)

genehmigten Dissertation.

Vorsitzender:

Univ.-Prof. Dr. rer. nat. Michael Krautblatter

Prüfer der Dissertation:

1. Univ.-Prof. Dr. sc. techn. Daniel Straub

2. Ao. Univ.-Prof. Dr. techn. Helmut Schweiger

Technische Universität Graz, Österreich

Die Dissertation wurde am 12.07.2016 bei der bei der Technischen Universität München eingereicht und durch die Ingenieur fakultät Bau Geo Umwelt am 18.10.2016 angenommen.

Declaration

With this statement, I declare that I have independently completed this PhD's thesis. The thoughts taken directly or indirectly from external sources are properly marked as such. This thesis was not previously submitted to another academic institution and has also not yet been published.

04.11.2016, Munich

Ji Yuan

Prenome Surname

Abstract

Rainfall-induced landslides pose a significant risk in many areas of the world. Transient heavy rainfall can cause a pore water pressure redistribution within surficial soil layers. An increase in the pore water pressure reduces the effective resistance of slopes and thus can lead to a loss of slope stability. This is regarded as the main cause of shallow landslides that occur during a rainfall event or soon afterwards. Due to the fact that the redistribution of pore water pressure is highly time-dependent, the slope stability evaluation must be performed in function of time.

In this thesis, a time-dependent stochastic model is developed for the study of slope stability under heavy rainfall. The model accounts for the uncertain nature of rainfall events and the spatial variability of soil permeability. The focus is on the 1D-infiltration-failure model, which is motivated by the fact that in shallow slope failure events, the failure surface is often approximately parallel to the slope surface. The slope failure mechanism is modeled by combining a subsurface infiltration model with an infinite slope model with layering parallel to the ground surface. Hence, the classical equation for infinite slope stability analysis can be utilized for evaluating the time-dependent behavior of the factor of safety of the slope. The stochastic behavior of the rainfall event is considered by the application of self-similar random process theory, while the random spatial variability of the saturated hydraulic conductivity is modeled with homogeneous non-Gaussian random fields.

The developed model is employed to assess slope reliability under random rainfall events with subset simulation. The latter is an adaptive sampling method that is especially efficient for estimating small failure probabilities in problems with a large number of random variables, which is typically the case when discrete representations of random processes/fields are involved. In addition, Bayesian analysis is applied to learn the stochastic model of the saturated hydraulic conductivity with measurement data obtained from the on-site investigation. Using the updated stochastic model, one can obtain posterior predictions of the slope stability and reliability conditional on the data.

Numerical examples are presented for studying the influence of the scale of fluctuation and the parameters of the stochastic model of the random rainfall event on the slope reliability. Additionally, the impact of measurement data on the posterior statistics of the factor of safety is investigated. The case studies show that a decrease in the scale of fluctuation has a significant influence on the transient behavior of the factor of safety and thus the probability of failure. By decreasing the scale of fluctuation, the mean factor of safety decreases faster with time elapsed, due to larger pore water pressure build-up at shallow depths, which favors shallow slope failure. Moreover, it is shown that more uniform rainfall patterns lead to higher infiltration volume and result in higher pore water pressure buildup that increases the probability of failure of the infinite slope.

Acknowledgements

First and foremost, I would like to extend my sincere gratitude to my supervisor, *Dr. Iason Papaioannou*, for his abundant professional help and patient guidance throughout my four years of PhD studies. I am deeply grateful to him in the completion of this thesis.

Special thanks to *Prof. Dr. Daniel Straub* for providing me the opportunity to pursue my doctoral degree in Technical University of Munich and financial support during my last phase of the PhD. The first two years were hard for me as a beginner with only geological background. Due to his patience and encouragement, I made big progress during my PhD studies. Thanks also to *Dr. Chin Man Mok* for his professional advice on the modeling.

Additionally, thanks to all members of ERA Group for the friendly atmosphere during my PhD studies. Particularly, I would like to say thanks to *Karen Arlt*, who helped me a lot with arranging my life in Munich.

Finally, I must express my very profound gratitude to my beloved family who unremittingly supported me without a word of complaint.

Ji Yuan

04.11.2016, Munich

TABLE OF CONTENTS

DECLARATION	I
ABSTRACT	III
ACKNOWLEDGEMENTS	V
CHAPTER 1 INTRODUCTION AND LITERATURE REVIEW	1
CHAPTER 2 1D-INFILTRATION-FAILURE MODEL	11
2.1 FAILURE MODEL BASED ON LIMIT EQUILIBRIUM METHOD	11
2.1.1 MOHR-COULOMB FAILURE CRITERION	12
2.1.2 INFINITE SLOPE MODEL	13
2.2 1D INFILTRATION-FAILURE MODEL	16
2.2.1 EXTENDED GREEN AND AMPT MODEL	17
2.2.2 RICHARDS EQUATION	23
CHAPTER 3 MODELING UNCERTAINTIES	29
3.1 RANDOM VARIABLES AND RANDOM VECTORS	29
3.1.1 RANDOM VARIABLES	29
3.1.2 RANDOM VECTORS	31
3.2 RANDOM FIELDS AND RANDOM PROCESSES	33
3.2.1 DEFINITIONS	34
3.2.2 ONE-DIMENSIONAL CORRELATION MODEL	36
3.2.3 GAUSSIAN RANDOM FIELDS	37
3.2.4 NON-GAUSSIAN RANDOM FIELDS AND TRANSFORMATION	37
3.2.5 DISCRETIZATION OF RANDOM FIELDS	38
3.3 MODELING PERMEABILITY OF SOIL LAYERS AS RANDOM FIELDS	41
3.4 MODELING RAINFALL EVENTS AS RANDOM PROCESSES	44
CHAPTER 4 RELIABILITY ANALYSIS	49
4.1 BASIC DEFINITION	50

4.2 PROBABILISTIC TRANSFORMATION	52
4.3 MONTE CARLO SIMULATION	54
4.4 SUBSET SIMULATION	55
4.5 TIME-DEPENDENT RELIABILITY ANALYSIS OF INFILTRATION-FAILURE MODEL	57
4.5.1 EXTENDED GREEN AND AMPT MODEL	57
4.5.2 RICHARDS EQUATION	61
CHAPTER 5 BAYESIAN UPDATING	63
5.1 BAYESIAN ANALYSIS	63
5.1.1 BAYES' THEOREM	63
5.1.2 LIKELIHOOD FUNCTION	65
5.2 BUS APPROACH	66
5.2.1 BASIC IDEA	66
5.2.2 SUBSET SIMULATION-BASED BUS APPROACH	68
5.2.3 ADAPTIVE SUBSET SIMULATION-BASED BUS APPROACH	69
5.2.4 LIMITATION OF THE SUBSET SIMULATION-BASED BUS APPROACH	70
CHAPTER 6 NUMERICAL INVESTIGATIONS	73
6.1 CASE DESCRIPTION	73
6.2 APPLICATION OF EXTENDED GREEN AND AMPT MODEL TO TIME-DEPENDENT RELIABILITY ANALYSIS	73
6.2.1 WETTING FRONT DEVELOPMENT	74
6.2.2 PORE WATER PRESSURE BUILDUP	76
6.2.3 MEAN FACTOR OF SAFETY	77
6.2.4 PROBABILITY OF FAILURE	80
6.3 APPLICATION OF RICHARDS EQUATION TO TIME-DEPENDENT RELIABILITY ANALYSIS	82
6.3.1 PORE WATER PRESSURE REDISTRIBUTION	83
6.3.2 PROBABILITY OF FAILURE	89
6.4 BAYESIAN UPDATING	92
CHAPTER 7 CONCLUSIONS	101

7.1 CONCLUSIONS	101
7.2 DISCUSSION AND OUTLOOK	103
<u>ANNEX A. NUMERICAL SOLUTIONS FOR RICHARDS EQUATION</u>	<u>107</u>
<u>ANNEX B. VALIDATION OF THE EXTENDED GREEN AND AMPT MODEL</u>	<u>109</u>
<u>ANNEX C. COMMONLY USED DISTRIBUTIONS</u>	<u>113</u>
<u>LIST OF TABLES</u>	<u>117</u>
<u>LIST OF FIGURES</u>	<u>119</u>
<u>REFERENCES</u>	<u>121</u>

Chapter 1 Introduction and literature review

Landslides are a major natural hazard in many parts of the world and pose serious threats to cities and infrastructure, particularly in mountainous areas. Each year, heavy damages caused by the run-out of landslides are reported, leading to severe economic losses and fatalities (Petley 2012; Papathoma-Köhle et al. 2015). Nevertheless, because of population growth and economic development, there is an ever-growing demand on land and increasing urbanization in mountainous areas, e.g. in the city developments of Hong Kong, Singapore, or Chongqing. In these regions, landslides are inevitable hazards and hence mitigation strategies against landslides are necessary (Choi and Cheung 2013).

Slope failures are typically triggered by external factors in slopes with unfavorable geological conditions, such as earthquakes (García-Mayordomo et al. 2009; Chen et al. 2012), heavy rainfall (Schuster et al. 2002; Lepore et al. 2012), and human activities (Malgot and Baliak 2002; Huang and Chan 2004), among others. This thesis focuses on rainfall-induced landslides, which most of them frequently take place in tropical regions (e.g. Rahardjo et al. 2005; Sahis et al. 2014). In tropical regions, rainfall events can have very high intensities combined with long persistence. This occurs particularly in wet seasons. For instance, in South America, catastrophic slope failures occur most commonly in the Andes Mountains of the northern and western parts of the continent, due to the fact that many parts of the area are subjected to precipitation that exceeds 1500mm/yr (Schuster et al. 2002).

Rainfall has two major effects that change the geomorphology of soil slopes: a small portion of rainwater forms runoff along the sloping surface (Crăciun et al. 2009) and washes away small particles of the soil mass, causing erosion (Assouline and Ben-Hur 2006; Defersha et al. 2011). The remaining rainwater penetrates into the soil and alters the pore water pressure distribution time-dependently (e.g. Perrens and Watson 1977; Iverson 2000), and this process is known as “infiltration”. It can lead to excessive slope displacements or even cause catastrophic failure, since an increase of pore water pressure reduces the effective resistance force of the slope (Fredlund 1995; Rahardjo et

al. 2005). This effect is regarded as the dominant failure mechanism of slopes under transient intense rainfall events (Lan et al. 2003). In contrast, erosion is usually associated with long-term rainfall events and is not considered in this thesis.

The effect of the increase of the pore water pressure depends on the location of the ground water table: in the unsaturated zone, the infiltrated rainwater can reduce the matric suction of the soil mass (Fredlund 1995), whereas in the saturated zone, the increase is caused by a rise of the ground water table that leads to the pore water pressure building up with respect to the water depth (Ray et al. 2010). Either effect makes a negative contribution to the slope stability.

For the transient behavior of the infiltration, failure surfaces most often take place within the unsaturated zone, since the surficial soil layers are more likely influenced by an intense rainfall event (Crosta and Frattini 2003; Zhang et al. 2005; Enrico and Antonello 2012). Therefore, for rainfall-induced landslide prediction, the key is to establish an appropriate model for representing this type of failure mechanism. In addition, the failure surface within the unsaturated zone is often approximately parallel to the sloping surface (Dietrich et al. 2007). In response to the rainwater infiltration, the time-dependent behavior of the pore water pressure redistribution should also be taken into consideration when modeling rainfall-induced landslide. Consequently, to describe the infiltration-failure phenomenon as precisely as possible, the entire model should include at least three parts, the rainfall, the infiltration and the slope stability model.

Hitherto, most relevant studies focused on the latter two parts for studying the slope stability in function of time. A series of research studies have been performed in recent years, and both analytical and numerical solutions are available (e.g. Borga et al. 1998; Iverson 2000; Muntohar and Liao 2010; Enrico and Antonello 2012). However, in order to analyze the slope stability in real time scale and to enhance real time decision making for mitigating losses, the three parts should ideally be integrated into a single model. In the literature, only a few studies have combined the three models to describe the rainfall-induced landslide as a systematic process (e.g. Cho and Lee 2002; Zhang et al. 2005; Huang et al. 2013; Cho 2014).

According to the limit equilibrium method, slope failure occurs when the driving forces exceed the resistance forces. The ratio of resistance forces over driving forces is termed factor of safety (FS). Hence, the slope is no longer stable once FS is less than unity (e.g. Griffiths 2011). To some extent, the limit equilibrium method regards the soil mass as a rigid body until it reaches the ultimate stress and starts to move towards the downslope. Therefore, the slope stability analysis with limit equilibrium methods is suitable for slopes with nearly no movement before a “sudden” failure.

It should be pointed out that in reality soils behave as elastic-plastic materials. In most cases, slopes usually form large cumulative deformations before a catastrophic failure event. This phenomenon has been verified both in the field and in controlled experiments (Petley 2004; Orense et al. 2004). However, modeling of progressive slope failure is intricate, and the advantage of the limit equilibrium method is its simplicity and efficiency. It is often employed for identifying the state of soil slopes regardless of soil deformation. As an efficient estimation method, this approach has been found wide application in slope stability analysis.

For slope stability analysis, it is often reasonable to employ an infinite slope model with layering parallel to the ground surface to represent subsurface infiltration as well as the shallow slope failure mechanism (Iverson 2000; Wu and Abdel-Latif 2000; Muntohar and Liao 2010; Santoso et al. 2011a). Since subsurface infiltration is predominately driven by gravitation, the soil slope is often simplified in practice as a column subject to one-dimensional flow (Muntohar and Liao 2010; Santoso et al. 2011b; Yuan et al. 2013; Yuan et al. 2015a). It can be assumed that the soil slope is governed by the vertical infiltration in cases with a relatively small slope angle. In cases with steep topography, it is better to assume that infiltration flows perpendicular to the sloping surface (Chen and Young 2006; Enrico and Antonello 2012).

The type of “sudden” effect failure considered in this study is the one caused by the pore water pressure building up during the rainwater infiltration process. In order to capture the time-dependent behavior of slopes, it is necessary to simulate the infiltration process. One possibility is to apply the Green and Ampt model (1911) for modeling one-

dimensional saturated flow through the homogeneous coarse soil (Muntohar and Liao 2010; Dou et al. 2015). However, the classical model needs to be modified for cases with heterogeneous soil, such as multi-layered soils. Another approach is to apply the solution of Richards equation, which can make more accurate evaluation for either one or two dimension infiltration cases (Chen and Young 2006; Enrico and Antonello 2012). The latter method can approach both saturated and unsaturated flow within the soil layers. In this work, the performance of both models is investigated.

According to the Green and Ampt model (1911), a well-defined wetting front separates the soil column into two parts, the saturated and unsaturated zones. The water flow advances like a piston flow through the soil column pulling down by the suction head at the wetting front. The infiltration process in the multi-layered soil is modeled by assuming that the flow rate remains constant within the wetted zone during the infiltration process (Chu and Marino 2005; Liu et al. 2008). The classical model can then be extended for application to the case with multi-layered soils. However, the extended Green and Ampt model still has some limitations. For instance, this model is only valid for the case subjected to non-stop and sufficiently large precipitation. Otherwise, the explicit ordinary difference equation (ODE) takes on a more sophisticated form whose solution is less straightforward.

Richards equation (1931) involves two dependent variables, the pressure head and the volumetric water content. The relationship is often described by the Van Genuchten model (1980). By solving Richards equation, one obtains the complete time-dependent behavior of the pore water pressure redistribution throughout the infiltration process. Since the governing equation is highly nonlinear, it is difficult to solve it analytically. Numerical solutions are available, e.g. by application of the finite difference, finite element and finite volume method; and are implemented in open source and commercial software, e.g. HYDRUS-1D or Seep/W (Šimůnek et al. 2009). Compared to the Green and Ampt model, an advantage of this model is that it can deal with arbitrary precipitation boundary conditions other than the assumption of a sufficiently large. Moreover, the solution of Richards equation provides more accurate and reliable information about the pore water pressure redistribution within the unsaturated zone. In

short, the application field of Richards equation (1931) is wider, yet it is computationally more costly than the extended Green and Ampt model (Yuan et al. 2013).

The temporal distribution of rainfall can be idealized by a uniform, triangle or other deterministic shape as shown in Figure 1.1 (Zhang et al. 2005; Yeh et al. 2008; Huang et al. 2013; Ali et al. 2014). These rainfall models are usually parameterized by the rainfall intensity and duration (Menabde and Murugesu 2000). For the extended Green and Ampt model, the non-stop rainfall event can be represented by a rainfall event with sufficiently large intensity; for Richards equation, the prescribed precipitation can be applied at the upper boundary.

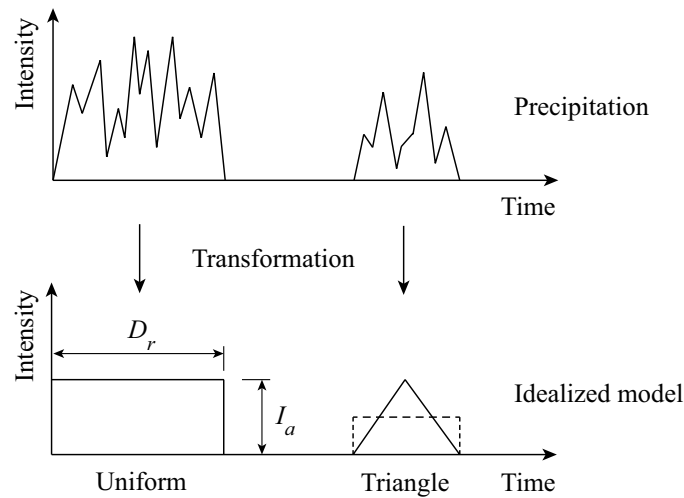


Figure 1.1 Two typical idealized rainfall events, in which D_r is the rainfall duration and I_a is the average rainfall intensity

A time-dependent slope stability model is then established based on the adopted models for the slope stability assessment, temporal rainfall distribution and rainwater infiltration. The input and output of the entire model are rainfall events and the slope stability. The state of soil slopes can be expressed as a temporal function of the factor of safety. However, the physical input parameters of the model, such as the properties of the soil mass and rainfall patterns, are highly uncertain. For instance, the strength and hydrogeological parameters of the soil vary randomly in space (Vogel et al. 2000; Zlotnik et al. 2007). Therefore, deterministic parameters are insufficient for analyzing and understanding the variability of soil slopes. Many applications based on the deterministic

slope stability model merely reflect one possible state of the soil slope and fail to take all possible states into account. In proper slope stability assessment, the uncertain nature of input parameters is accounted for through performing a slope reliability analysis. Thereby, the safety of the slope is assessed through the probability of slope instability, known as probability of failure.

Input uncertainties can be classified into uncertainties in time and space, modeled respectively by random processes and random fields. These two types of uncertainties are discussed in the following.

Hydrogeological parameters are highly heterogeneous, even within a lithological zone that appears to be homogeneous, due to the inherent variability of the soil formation process (Phoon and Kulhawy 1999; Vogel et al. 2000). Such spatially variable quantities are commonly modeled by continuous random fields. Recent studies that applied random field theory to model the soil permeability have shown that the spatial variability of permeability has significant influence on the stochastic behavior of slope stability (Santoso et.al. 2011*b*; Yuan et.al. 2015*a*).

In this thesis, the inherent vertical variability of two hydrogeologic parameters is included in the analysis with the extended Green and Ampt model: saturated hydraulic conductivity and suction head. These two parameters are modeled as one-dimensional, stationary, and cross-correlated random fields. Continuous random fields consist of infinite number of random variables and their numerical treatment requires their discretization into a finite number of random variables. Through discretization of the random fields, the soil column is represented by a multi-layered system with uniform values in each layer, which are described by correlated random variables (Li and Der Kiureghian 1993).

Temporal uncertainty is associated mainly with precipitation. Deterministic approaches to model precipitation work well for simulating short time periods or extreme rainfall events, yet do not reflect the stochastic nature of the rainfall patterns. A more realistic representation of the effect of rainfall on the reliability can be obtained through a random process modeling of rainfall events (Menabde and Murugesu 2000; Onof et al.

2000). The parameters of the random process model can be estimated from rainfall data. Characteristic rainfall patterns from the region of interest can be obtained through simulating the random rainfall process.

In the analysis with Richards equation model, we assess the reliability of infinite slope subject to random rainfall events and account for the spatial variability of soil. We model the rainfall event by a self-similar random process (Menabde et al. 1997; Menabde and Murugesu 2000). We also apply a one-dimensional statistically homogeneous random field to describe the spatial variability of the saturated hydraulic conductivity (Santoso et al. 2011a; Yuan et al. 2015a; Yuan et al. 2015b).

The failure criterion of the slope is modeled by the factor of safety concept for both models, which implies a linear Mohr-Coulomb yield surface. The probability of failure is then evaluated with reliability methods, e.g. approximation methods such as the first order reliability method (FORM) or simulation techniques based on the Monte Carlo method (Ditlevsen and Madsen 1996; Lemaire 2009). For each realization of the rainfall pattern and saturated hydraulic conductivity, the pore water pressure with respect to the time and depth is obtained by a numerical solution of Richards equation. The stability analysis is evaluated by substituting the pore water pressure into the equation of the factor of safety for the infinite slope failure model.

Efficient estimation of the probability of failure in relatively high dimensional problems can be achieved by application of Subset Simulation (Au and Beck 2001). Subset Simulation is an adaptive Monte Carlo method that estimates probabilities of rare events efficiently independent of the number of random variables. This is achieved by expressing the rare event as an intersection of more frequent events that are estimated by application of Markov chain Monte Carlo (MCMC) sampling (Papaioannou et al. 2015).

From a practical point of view, the prior hypothesis on the stochastic description of uncertain input greatly depends on initial site investigations. This process is often constrained by limited information collected from the field and hence it is difficult to ensure whether the original description is in accordance with the real distribution of soil properties. The stochastic description of the soil properties can be updated with new data

through application of Bayesian analysis (e.g. Beck and Katafygiotis 1998). Pressure and deformation data is often collected by means of remote sensing technology during the last decades (Tofani et al. 2013). In Bayesian analysis, data is described by the likelihood function. The distribution of the soil properties conditional on the data can be obtained by application of Bayes' rule, which states that the posterior distribution is proportional to the product of the prior and the likelihood function.

Samples from the posterior density can be obtained by application of MCMC methods (Beck and Au 2002; Straub and Papaioannou 2014). An alternative approach is to transform the Bayesian updating problem to an equivalent reliability problem. This approach, termed Bayesian Updating with Structural reliability methods (BUS) allows application of methods developed for structural reliability analysis for sampling the posterior distribution (Straub and Papaioannou 2015). In this study, the BUS approach with Subset Simulation is applied to sample the distribution of the hydrogeological properties of the soil slope conditional on pressure data.

The general framework of this thesis is illustrated in Figure 1.2. The time-dependent model will be presented in Chapter 2. Modeling uncertainty will be presented in Chapter 3. Chapter 4 interprets the basic theory of reliability analysis and Chapter 5 discusses about the Bayesian updating algorithm. Subsequently, a numerical example will be present and results will be discussed in Chapter 6. Finally, the conclusion is reached in Chapter 7, together with a discussion and an outlook on future work.

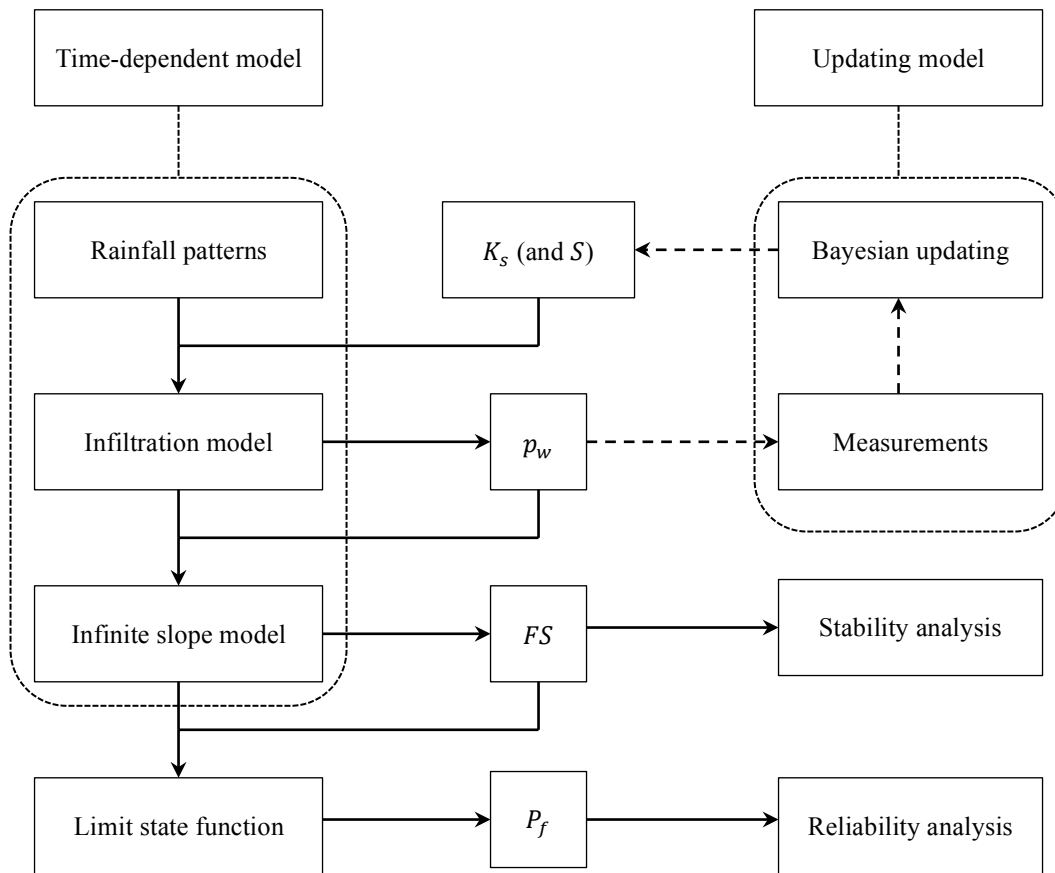


Figure 1.2 Flow chat of the approach developed in this thesis, in which K_s is the saturated hydraulic conductivity; S is the suction head; p_w is the pore water pressure; FS is the factor of safety; P_f is the probability of failure.

Chapter 2 1D-infiltration-failure model

Infiltration significantly influences the pore water pressure redistribution within surficial soil layers (Enrico and Antonello 2012) and hence the stability of soil slopes. The infiltration-failure model is widely applied to evaluating the slope stability subjected to rainfall events (e.g. Zhan and Ng 2004; Lu and Godt 2008; Chae et al. 2015). This study focuses on failure events triggered by 1D flow (Muntohar and Liao 2010; Dou et al. 2015), since the rainwater flow is predominantly driven by gravity and it mainly forms a one dimensional flow in hillsides unless the topography is too steep. Additionally, the infiltration process is highly time-dependent. It is therefore of interest to capture its influence on the slope stability by establishing the 1D-infiltration-failure model.

To model the rainwater infiltration through heterogeneous soils, two approaches are examined. The first is based on an extension of the classical Green and Ampt model (Green and Ampt 1911) for the multi-layers case. The second is based on the numerical solution of the Richards equation (Richards 1931; Fred 2011), which is a common approach for modeling infiltration in heterogeneous soils (Iverson 2000; Santoso et al. 2011*a*). The accuracy of the former model is examined in Annex B, through a comparison with the latter (more accurate) model based on Richards equation.

Soil failure in this thesis is modeled according to the limit equilibrium method (e.g. Zhang et al. 2005; Santoso et al. 2011*a*). It should be pointed out that, the progressive failure event is often triggered by the soil deformation (e.g. Petley et al. 2005). However, accurate modeling of this phenomenon would require a full mechanical analysis of the slope, which is beyond the scope of the 1D model developed in this chapter.

2.1 Failure model based on limit equilibrium method

According to the limit equilibrium method, a slope failure along a certain slip surface occurs if the driving stress exceeds the resistance in this layer. The resistance is

2.1 Failure model based on limit equilibrium method

determined by application of the Mohr-Coulomb failure criterion, which is widely used for estimating the allowable shear stress within soils. The driving stress of slopes is due to the weight of overlaying soils. Considering the influence of the pore water pressure, the stability of the slope is expressed by the factor of safety (FS), which is defined as the effective resistance divided by driving stress.

2.1.1 Mohr-Coulomb failure criterion

The Mohr-Coulomb failure criterion describes the linear relationship between shear strength of the soil and the effective applied normal stress [see Fig. 2.1(a)]. It reads (Terzaghi et. al. 1996):

$$\tau_f = c' + \sigma'_n \tan \varphi' \quad (2.1)$$

in which c' is the effective cohesion of soil mass; φ' is the effective friction angle of soil mass, σ'_n is the effective normal stress, defined as $\sigma'_n = \sigma_n - p_w$. Here, σ_n is the normal stress and p_w is the pore water pressure.

It is known that the soil strength depends on the shear stress. The limit equilibrium method refers to a limit state of soil mass, in which the shear stress τ reaches the failure value τ_f under a given effective normal stress σ'_n and which is assumed to initiate deformations at the slip surface. The soil mass is regarded as a rigid body until it fails. Therefore, the limit equilibrium method provides a straightforward way to identify the soil state, namely stable or non-stable, regardless of the strain within the soil mass.

According to the limit equilibrium method, the failure value of the soil mass τ_f is assumed equal to the peak value τ_p , i.e. $\tau_f = \tau_p$. However, laboratory tests have shown that this failure condition is not entirely realistic. In fact, the catastrophic failure event might occur far away from this peak value τ_p during the post peak phase before the residual shear stress τ_r is reached, with $\tau_r < \tau_p$ [see Fig. 2.1(b)]. It should be pointed out that the ultimate value of shear strength also relies on the strain of soil mass. The principle of this progressive failure mode is sophisticated and somewhat non-conservative, e.g. strain-softening mode (Zhang et al. 2013). Considering the large

uncertainties in natural geological condition, it is reasonable to make the conservative assumption in engineering design. Due to this reason, the limit equilibrium method is still commonly employed for slope stability analysis (Ugai and Leshchinsky 1995).

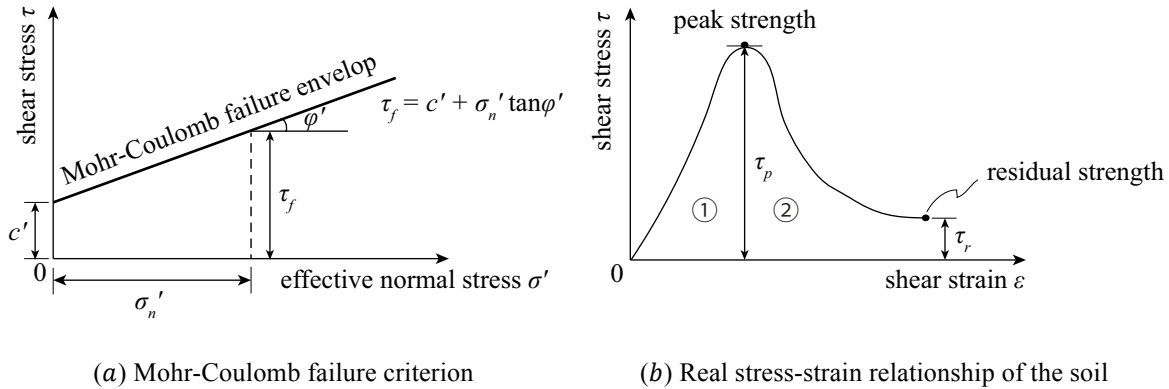


Figure 2.1 Failure modes of the soil, in which ① represents the pre-peak phase and ② represents the post-peak phase in figure (b).

2.1.2 Infinite slope model

An infinite slope model represents a simplified natural slope bounded by a stress-free surface (Iverson and Major 1986). This semi-infinite body is often combined with one-dimensional or two-dimensional seepage models (e.g. Iverson 2000; Chen and Young 2006) for analyzing slope stability (e.g. Muntohar and Liao 2010) or movement problems (e.g. Conte and Troncone 2012). In general, the depth of soil slope is relatively small in comparison with the length of sloping surface (Iverson 2000). Therefore, the infinite slope is often applied to represent shallow slope failure mechanism of hillsides in cases with gentle inclination angle.

Each potential slip surface along the depth of the soil profile can be reasonably assumed parallel to the ground surface, since this corresponds to the common behaviour of real shallow slope failures (Conte and Troncone 2012). The critical slip surface is found among all potential slip surfaces as the one whose factor of safety has the minimum value. This concept can be further applied to the stability evaluation of slopes in multiple soil layers.

2.1 Failure model based on limit equilibrium method

Rainwater infiltration often has a significant influence on the pore water pressure redistribution within surficial soil layers of slopes. Therefore, the critical slip surface is most likely to be located at shallow depths (Enrico and Antonello 2012). We thus concentrate on the unsaturated zone of soil slopes and ignore the initial ground water table prior to rainfall infiltration.

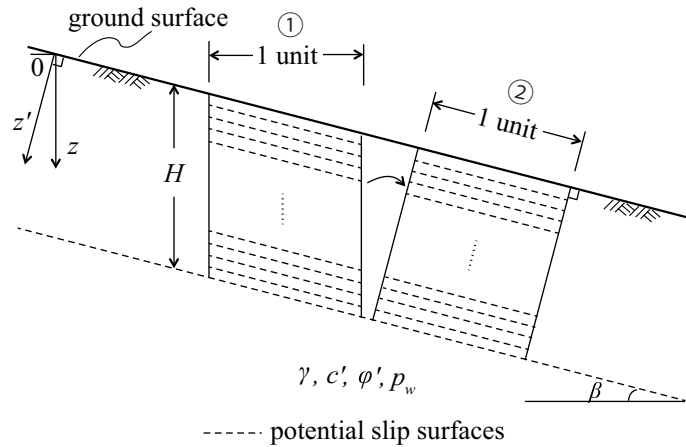
A slice with unit width can be abstracted from the infinite slope model and used to represent the entire semi-infinite sloping body. Typically, there are two fundamental ways to obtain the unit slice: the boundary of two sides is either taken in the vertical direction (e. g. Griffiths et al. 2011) or perpendicular to the sloping surface (e.g. Chen and Young 2006; Conte and Troncone 2012). Figure 2.2(a) illustrates an infinite slope model and (b) and (c) show the two types of unit slices taken from the infinite slope.

In the following, the unit slice is taken with vertical boundaries. The forces acting on the side boundaries can be ignored, since their values are approximately equal and can be eliminated during the computation, i.e. $T = T'$ [see Fig. 2.2(b) and (c)]. The applied normal force N on the potential slip surface equals the projection of the gravity of the unit slice perpendicular to the potential slip surface, i.e. $N = \gamma z \cos \beta$ [see Fig. 2.2(b)], in which γ is the average unit weight of the soil mass above the slip surface and β is the slope inclination. A potential slip surface can be defined at any depth within the range $z \in [0, H]$ and $z' \in [0, H \cos \beta]$, respectively. It is assumed that the change of unit weight of soil mass γ during the rainwater infiltration is negligible. Taking the contribution of the pore water pressure during the rainwater infiltration into account, the effective normal stress at the potential slip surface at depth z is obtained as $\sigma'_n = \gamma z \cos^2 \beta - p_w$. Substituting into Eq. (2.1), namely utilizing the linear Mohr-Coulomb failure criterion, one can obtain the resistance stress R [see Fig. 2.2(b) and (c)]:

$$R = (\gamma z \cos^2 \beta - p_w) \tan \varphi' + c' \quad (2.2)$$

Following Figure 2.2a, the deepest potential slip surface is located at depth H in the vertical direction z . The downslope driving stress is caused by the soil gravity, i.e. the projection of the soil gravity along the slip plane:

$$D = \frac{\gamma z \sin \beta}{\cos \beta} = \gamma z \sin \beta \cos \beta \quad (2.3)$$



(a) Infinite slope model: ① and ② are two ways to take one unit slice, and the corresponding mechanical analysis is presented in (b) and (c), respectively.



(b) One unit slice with vertical boundaries.

(c) One unit slice with boundaries perpendicular to the ground surface.

Figure 2.2 Unit slice in an infinite slope.

The soil shear strength in the slip surface is a function of the effective cohesion c' , the effective friction angle ϕ' , and the pore water pressure p_w . The factor of safety of a homogeneous slope is defined as the ratio between resistance force and driving force (e.g. Griffiths et al. 2011):

$$FS = \frac{R}{D} = \frac{(\gamma z \cos^2 \beta - p_w) \tan \phi' + c'}{\gamma z \sin \beta \cos \beta} \quad (2.4)$$

Let z' be the axis perpendicular to the sloping surface (see Fig. 2.2a). It is $z' = z \cos \beta$. Replacing z with $z' / \cos \beta$ in Eq. (2.4), one can obtain the factor of safety

2.2 1D infiltration-failure model

for the unit slice whose boundaries are perpendicular to the slope surface (Fig. 2.2c):

$$FS = \frac{(\gamma z' \cos \beta - p_w) \tan \phi' + c'}{\gamma z' \sin \beta} \quad (2.5)$$

The stability of infinite slopes is governed by the critical slip surface, whose factor of safety has minimum value among all potential slip surfaces. Thus, when performing slope stability analysis it is necessary to search for the location of the critical slip surface.

The slope is considered unstable if FS is smaller than unity. In principle, the limit equilibrium method regards the soil mass as a rigid body until it reaches the ultimate strength, at which point it is assumed to move very fast towards the downslope. The method does not provide any information about the soil deformation. Therefore, the slope stability analysis by means of the limit equilibrium method is suitable for cases where failure is caused by a “sudden” effect.

A “sudden” effect in cases of rainfall-induced landslides can occur due to the pore water pressure building up. The pore water pressure redistribution throughout the rainfall infiltration process causes the effective stress within the soil slope to vary with time, which is the reason for the time-dependent behavior of the slope stability during rainfall events. This has been addressed in recent studies (Zhang et al. 2005; Muntohar and Liao 2010).

2.2 1D infiltration-failure model

The Green and Ampt model (1911) and Richards equation (1931) are commonly applied to simulate water infiltration. In particular, the Green and Ampt model can be used for solving one-dimensional problems, whereas Richards equation can model infiltration in 1D, 2D or 3D (e.g. Iverson 2000; Fred 2011; Wu et al. 2012). The classical Green and Ampt model (1911) is only suitable for a homogenous soil stratum, yet Richards equation (1931) can be applied to either homogenous or heterogeneous soils. Considering the infinite slope model described in Section 2.1.2, the rainwater flow is subjected to the side

boundaries of the unit slice, forming the downslope seepage. The inflow and outflow through one unit slice due to the downslope seepage is nearly the same and can be neglected. That is, it is reasonable to assume the rainwater merely forms one dimension flow within infinite soil slopes unless the topography is too steep. Thus, this section will focus on the application of the Green and Ampt model and Richards equation for the one dimensional flow, particularly for the multi-layer case.

2.2.1 Extended Green and Ampt model

The Green and Ampt (1911) assumptions are utilized to simulate the rainwater infiltration process. They state that the vertical infiltration of rainwater causes a well-defined wetting front (see Fig. 2.3). Above the wetting front, the soil is assumed to be fully saturated while below the wetting front it continues to have its initial moisture content θ_0 . Note that these assumptions are mostly applicable to highly permeable soils such as gravel or sandy soils, subjected to intense rainfall events (Chu and Marino 2005). In this section, we first look into the classical Green and Ampt model, which is only valid for homogeneous soils. Subsequently, the extended model will be presented based on the fundamental assumptions of the classical Green and Ampt model.

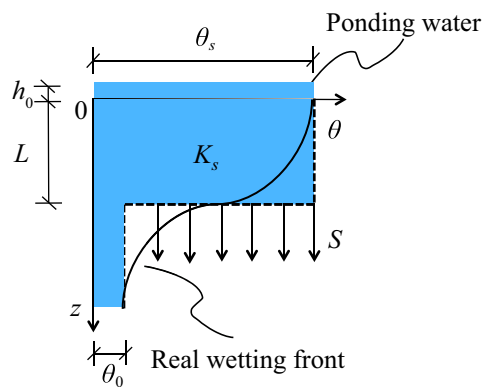


Figure 2.3 Classical Green and Ampt model, in which h_0 is the depth of the ponding water; L is the depth of the wetting front; S is the suction head; θ_0 is the initial water content; θ_s is the saturated water content.

The basic assumption of the Green and Ampt model implies a piston flow within the soil column instead of the real wetting front (see Fig. 2.3). The water deficit $\Delta\theta$ is defined as an increase from the initial water content θ_0 to a saturated water content θ_s , i.e.

2.2 1D infiltration-failure model

$$\Delta\theta = \theta_s - \theta_0 \quad (2.6)$$

Typically, the water flow is perpendicular to the ground surface. Let F be the cumulative infiltrated volume. Intense and uninterrupted rainfall events provide sufficient infiltration volume and hence for the piston flow one could obtain

$$F = L \cdot \Delta\theta \quad (2.7)$$

in which L is the depth of the wetting front. Considering the ponding water above the ground surface, the hydraulic head at the wetting front can be expressed as:

$$h = h_0 + L + S \quad (2.8)$$

in which h_0 is the depth of ponding water, S is the suction head at the wetting front. Ignoring the depth of ponding water, i.e. setting $h_0 = 0$, the vertical hydraulic gradient at the wetting front can be written as

$$i = \frac{dh}{dz} = -\frac{L+S}{L} \quad (2.9)$$

The infiltration rate of rainwater is defined as the time derivative of the cumulative infiltrated volume. Requiring that the one dimension flow obeys Darcy's law, the governing equation reads:

$$\frac{dF}{dt} = f = -K_s i \quad (2.10)$$

in which K_s is the saturated hydraulic conductivity.

Substituting Eq. (2.9) into Eq. (2.10), and knowing from Eq. (2.7) that $L = F/\Delta\theta$, the governing equation for one dimension flow yields,

$$f(t) = \frac{dF}{dt} = K_s \left[1 + \frac{S\Delta\theta}{F(t)} \right] \quad (2.11)$$

in which $f(t)$ is the infiltration rate at time t . Taking the integral on both sides, one can obtain the cumulative infiltration volume F as an implicit function of time,

$$F(t) = K_s t + S\Delta\theta \ln\left[1 + \frac{F(t)}{S\Delta\theta}\right] \quad (2.12)$$

Therefore, both the infiltration rate f and the cumulative infiltration volume F can be computed interactively by a numerical procedure in a step-wise manner, for example (e.g. Muntohar and Liao 2010),

$$F(t + \Delta t) - F(t) = K_s \Delta t + S\Delta\theta \ln\left[1 + \frac{F(t + \Delta t) - F(t)}{S\Delta\theta + F(t)}\right] \quad (2.13)$$

in which Δt is the computational time step. This implicit function is solved iteratively through forward difference scheme and it will be applied to the programming.

The classical Green and Ampt model has the following three limitations, which limit its application to practical situations: (1) Vertical flow is applied to the case with the horizontal distributed soil layer (see Fig. 2.3), but it is unclear how to define the flow path in an inclined slope. (2) The upper boundary of the infinite slope is subjected to a non-stop intense rainfall event. (3) This model is suitable for the homogeneous case, an extension is needed for applying it to multi-layered soils. Particularly, addressing the last limitation is vital to develop the model in this study. Further assumptions of the Green and Ampt model will be presented and discussed in the following section.

The first issue was addressed by (Muntohar and Liao 2010) who proposed the following modified Green and Ampt equation, applicable to inclined ground surfaces:

$$F(t) = K_s t + \frac{S\Delta\theta}{\cos\beta} \ln\left[1 + \frac{F(t)\cos\beta}{S\Delta\theta}\right] \quad (2.14)$$

Consider using the first way to attain the unit slice of infinite slope [cf. Fig. 2.2(b)], that is, vertical infiltration is assumed, since the rainwater is predominantly driven by gravity. The difference between the vertical flow and the water flow normal to the ground surface is rather small when topography is not too steep [compare Eq. (2.12) and (2.14)]. Therefore, if the inclination angle β is small, i.e. $\cos\beta \approx 1$, Eq. (2.14) is approximately the same as Eq. (2.12).

2.2 1D infiltration-failure model

The second limitation described above is not critical here, as the developed extended Green and Ampt model mainly focuses on non-stop intense rainfall events and effective drainage (no ponding above slope surface), during which it is assumed that the rainfall intensity is larger than the infiltration capacity and the pore water pressure at the slope surface is equal to zero (see Fig. 2.4). It should be pointed out that, this model can also be extended to address cases with unsteady (variable) rainfall intensity (Chu and Marino 2005; Liu et al. 2008).

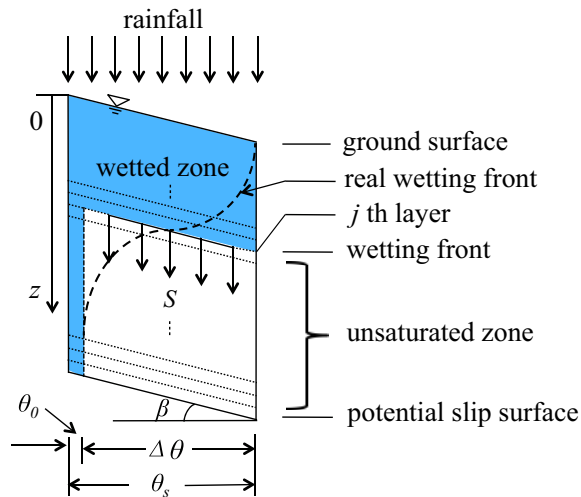


Figure 2.4 Infiltration process on the unit slice based on Green and Ampt assumptions, in which β is the slope angle; S is the suction head; θ_0 is the initial water content; $\Delta\theta$ is the deficit between saturated and the initial water content; θ_s is the saturated water content.

Consider the case where a single soil column is discretized to a multi-layered soil (see Fig. 2.4). The soil column is divided into a number of equal-thickness layers with varying saturated hydraulic conductivities and suction heads. This method will be further discussed in Chapter 3. The classical Green and Ampt model cannot handle such a multi-layer soil. To address this limitation, we assume that the wetting front development takes place in a step-wise manner for approaching the multi-layered case, whereby the wetting front advances by one layer in each computational time step; i.e. in step j the wetting front is exactly located at the bottom of the j th layer (Fig. 2.4). For simplicity, the initial moisture content θ_0 and soil porosity θ_s are considered to be constants within the unit slice (see Fig. 2.3 and 2.4).

According to the Green and Ampt assumptions, the wetting front is pulled down by the suction head S (see Fig. 2.4). Based on Eq. (2.9), the hydraulic gradient i from the ground surface to the wetting front at layer j in the vertical direction is:

$$i_j = \nabla h_j = -\frac{h_j}{z_j} = -\frac{z_j + S_j}{z_j} \quad (2.15)$$

where z_j is the depth of the wetting front at the bottom of the layer j ; S_j is the suction head at the wetting front. One can then evaluate the infiltration rate f_j via Darcy's law as:

$$f_j = -K_{eff,j} \cdot i_j \quad (2.16)$$

where $K_{eff,j}$ is the effective vertical saturated hydraulic conductivity, which for a heterogeneous field is averaged with the harmonic mean of the vertical saturated hydraulic conductivities at the soil layers within the wetted zone (Freeze and Cherry 1979):

$$K_{eff,j} = \frac{j}{\sum_{l=1}^j \frac{1}{K_l}} \quad (2.17)$$

in which K_l is the saturated hydraulic conductivity of the wetted discretization layer l . This equation results in an approximation of the infiltration process in cases where the permeability increases with depth. The approximation error when modeling multi-layered soils with variable permeability is expected to be small if deep soil layers with low permeability have similar values of saturated hydraulic conductivity to the effective hydraulic conductivity K_{eff} of the wetted zone. The cumulative infiltration will be governed by the infiltration capacity and can be obtained as:

$$t_j = \int_0^{t_j} dt = \int_0^{z_j} \frac{\Delta\theta}{f_j} dz \quad (2.18)$$

Eq. (2.18) can be evaluated numerically by substituting the integral with a summation over the wetted discretization layers as:

$$t_j = \Delta z \cdot \Delta\theta \cdot \sum_{l=1}^j \frac{1}{f_l} \quad (2.19)$$

2.2 1D infiltration-failure model

where Δz is the thickness of each layer and f_l is the flow rate at the l th wetted discretization layer. Through Eq. (2.19) one has a direct relationship between time and the wetting front development.

The pore water pressure enters the definition of the factor of safety [see Eqs. (2.4) and (2.5)] and therefore the slope stability exhibits time-dependent behavior due to a change in pore water pressure during the infiltration process. The following introduces the computation strategy for calculating the pore water pressure redistribution.

The pore water pressure buildup within the wetted zone varies with time and space, depending on the spatial variability of the saturated hydraulic conductivity and initial suction head. In this section, an extension of the Green and Ampt model is derived that allows for estimation of the pore water pressure distribution in multi-layered soil profiles. The model is based on the following assumption, which was also used in (Chu and Marino 2005, Liu et. al. 2008, Ma et al. 2010). Due to flow continuity, the effective flow rate of the wetted zone f computed by Eq. (6) is assumed to be equal to the flow rate at each wetted layer, i.e.

$$f_1 = f_2 = \dots = f_l = \dots = f_j \quad (2.20)$$

where f_l is the flow rate at wetted layer l , computed by

$$f_l = -K_l \cdot i_l = K_l \cdot \frac{\Delta h_l}{\Delta z} \quad (2.21)$$

Here, i_l is the hydraulic gradient of layer l and Δh_l represents the change of hydraulic head within the l th layer. Rearranging Eq. (2.21), one obtains:

$$\Delta h_l = \frac{f_l}{K_l} \cdot \Delta z \quad (2.22)$$

At the bottom of the l th wetted layer, the hydraulic head h_l is calculated by summing the incremental heads Δh_l over all wetted layers $k \leq l$:

$$h_l = h_0 - \sum_{k=1}^l \Delta h_k \quad (2.23)$$

in which h_0 is the boundary hydraulic head at the top of the wetted zone, which is $h_0 = 0$ as the ponding is neglected (see Fig. 2.4). Since the hydraulic head h_l consists of the pressure head ψ_l and the elevation z_l , the pressure head at the bottom of l th layer is evaluated as:

$$\psi_l = h_l - z_l \quad (2.24)$$

The pressure head at the wetting front is equal to the suction head, i.e. it holds $\psi_j = S_j$. The pore water pressure at the depth z_l can be computed as $p_w(z_l) = \gamma_w \cdot \psi_l$, where γ_w is the unit weight of water. Based on these parameter values, the pore water pressure distribution within the wetted zone can be computed.

One of most important advantages of the extended Green and Ampt model is its computational efficiency compared to the numerical solution of the Richards equation, presented in Section 2.2.2. Moreover, the time-dependent behaviour of soil slopes can be described in function of the wetting front development, which bridges time and the slope stability. Generally, the wetting front development reflects the influenced region with respect to time. Hence, based on the computation results one could visually understand the change of the slope stability due to the extension of wetted zone during the infiltration process. Nevertheless, the shortcoming of this model is the accuracy for evaluation of the pore water pressure redistribution in multilayer slopes, since the assumption of a clear wetting front is only valid for coarse soils (see Annex B).

2.2.2 Richards equation

The Richards equation (Richards 1931) describes the unsaturated flow through pore medium, such as soil layers. The infiltration flux of rainwater through a homogenous soil layer obeys Darcy's law,

$$\mathbf{q} = -K \cdot \nabla \mathbf{h} \quad (2.25)$$

in which \mathbf{h} is the vector of hydraulic head; ∇ is the gradient operator and in the case of one dimensional flow $\nabla \mathbf{h} = \frac{\partial h}{\partial z}$ [we use second strategy to abstract the unit slice, see Fig.

2.2 1D infiltration-failure model

2.2(a) and (c)]; K is the hydraulic conductivity of a given soil type. To simulate the unsaturated flow, K is regarded as a variable during the wetting and drying process even within the homogeneous soil column.

The infiltration rate f is equivalent to the change of moisture content θ in time scale [compare with Eq. (2.10)], that is,

$$\mathbf{f} = \frac{\partial \theta}{\partial t} = -\nabla \mathbf{q} \quad (2.26)$$

Combining Eqs. (2.25) and (2.26) and considering the spatial variability of the hydraulic conductivity K , the classical three dimensional Richards equation can be written as:

$$\frac{\partial \theta}{\partial t} = \nabla \cdot (\mathbf{K} \cdot \nabla \mathbf{h}) \quad (2.27)$$

in which \mathbf{K} is a vector of hydraulic conductivity, namely $\mathbf{K} = K_{z'}$. This conservation formula indicates that the moisture content θ , hydraulic conductivity \mathbf{K} , and hydraulic head \mathbf{h} have the certain functional relationship with respect to the time and space (e.g. Van Genuchten 1980).

The pore water pressure redistribution within the soil slope is mainly influenced by vertical infiltration rather than by horizontal flow (Santoso et al. 2011a). Vertical infiltration (direction z') is modelled in HYDRUS-1D (Šimůnek et al. 2009), which applies a one-dimensional flow model. Note that the hydraulic head h can be expressed as the sum of the pressure head ψ and elevation. In particular, on an inclination plane it is $h = \psi + z' \cos \beta$, in which β is the inclination angle of the slope [see Fig. 2.2(a)]. The governing equation of one-dimension water flow then can be described as a modified version of Richards equation (Šimůnek et al. 2009):

$$\frac{\partial \theta}{\partial t} = \frac{\partial}{\partial z'} [K (\frac{\partial \psi}{\partial z'} + \cos \beta)] \quad (2.28)$$

in which $\theta \in [\theta_0, \theta_s]$ is the water content of the soil layer; θ_0 and θ_s are the water content of the soil layer in the very dry and saturated condition, respectively. The input to the computation consists of the saturated hydraulic conductivities for each discrete soil layer and the rainfall pattern. Consider the entire soil column as unsaturated. The solution of HYDRUS-1D provides the pressure head $\psi(z', t)$ at each time step t and at each depth z' . Then, the pore water pressure $p_w(z', t)$ is obtained as $p_w(z', t) = \gamma_w \psi(z', t)$, in which γ_w represents the unit weight of water.

During the rainwater infiltration process, the pore water pressure p_w varies with time t and depth z' within the soil. Because $p_w = \gamma_w \psi$, it follows that ψ also varies with z' and t as $\psi(z', t) = \frac{p_w(z', t)}{\gamma_w}$.

Since Richards equation is a non-linear partial differential equation, it is often difficult to solve it directly, either using analytical or numerical method (e.g. Zhan and Ng 2004; Fred 2011). The general idea for solving the Richards equation is to find an appropriate model to describe the relationship among the aforementioned three parameters. In the following, we discuss how to approach the hydraulic conductivity K by means of Gardner (1958) and Van Genuchten (1980) formulations.

The hydraulic conductivity at certain depth z' is given by:

$$K(\psi, z') = K_r(\psi)K_s(z') \quad (2.29)$$

in which $K_s(z')$ is the saturated hydraulic conductivity and $K_r \in [0,1]$ is the relative hydraulic conductivity. Notice that, the relative hydraulic conductivity also depends on the depth of the soil, yet here we assume the relative hydraulic conductivity merely depends on the hydraulic head, denoted by $K_r(\psi)$. According to the simplified exponential model proposed in (Gardner 1958), $K_r(\psi)$ can be expressed as:

$$K_r(\psi) = e^{-\alpha\psi} \quad (2.30)$$

in which α is empirical parameter based on a given soil type. Another more sophisticated model was developed in (Van Genuchten 1980) based on the assumption of Brooks and

2.2 1D infiltration-failure model

Corey (1964). The so-called Van Genuchten model expresses the relative hydraulic conductivity as follows:

$$K_r(\psi) = \begin{cases} \frac{\{1 - (\alpha|\psi|)^{n-1} [1 + (\alpha|\psi|)^n]^{-m}\}^2}{[1 + (\alpha|\psi|)^n]^{m/2}}, & \psi \leq \psi_s \\ 1, & \psi > \psi_s \end{cases} \quad (2.31)$$

in which α , n , m are empirical parameters that depend on the soil type (Rawl et. al. 1982), with $m = 1 - 1/n$; ψ_s is the air-entry value. Figure 2.5 illustrates the relationship between the relative hydraulic conductivity and the pressure head for different values of the parameters α and n . It is assumed that there is no hysteresis during the wetting and drying process of the water flow. The sandy soil is represented by values $\alpha = 0.145\text{cm}^{-1}$ and $n = 2.68$, and the silty soil by values $\alpha = 0.00423\text{cm}^{-1}$ and $n = 2.06$. Moreover, the air-entry value is assumed zero in this study, i.e. $\psi_s = 0$. Figure 2.5 represents the transition between saturated and unsaturated flow throughout the infiltration process. The pressure head is nearly the same for both soils when the saturated flow occurs, i.e. when $K_r = 1$. When the relative hydraulic conductivity K_r is close to zero, the pressure head reaches a minimum value, which corresponds to the dry condition of the soil.

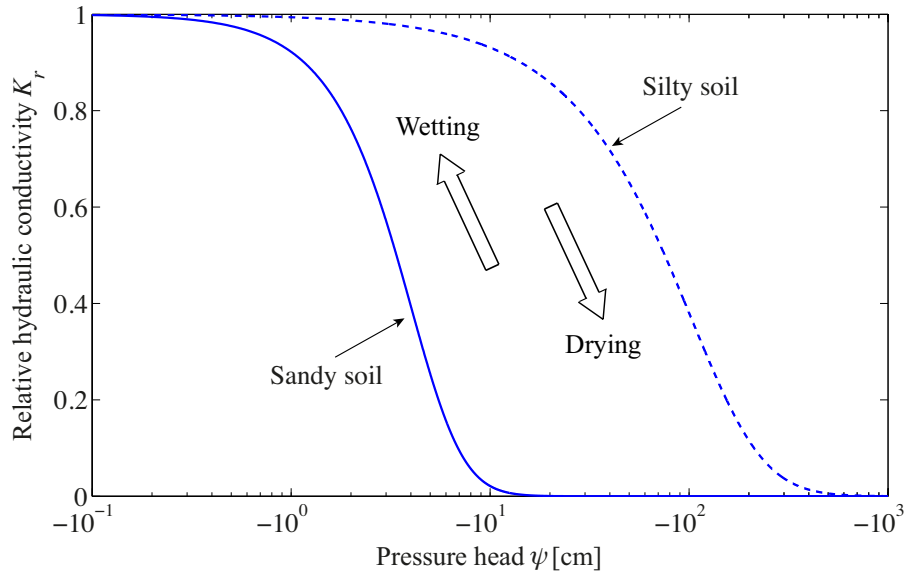


Figure 2.5 Relative hydraulic conductivities in terms of pressure head for silty and sandy soils, the parameters are given by $\alpha = 0.00423\text{cm}^{-1}, n = 2.06$ and $\alpha = 0.145\text{cm}^{-1}, n = 2.68$, respectively (Šimůnek 2009).

Richards equation can be solved analytically (Iverson 2000; Fred 2011) or numerically (Zabra et al. 1990; Šimůnek 2009). An analytical solution of Richards Equation can only be obtained under certain conditions. To avoid making unrealistic assumptions, the numerical solution is more often applied (see Annex A). It should be also mentioned that a non-uniform precipitation could be applied as upper boundary in the Richard's equation. The Green and Ampt model can also be applied in case of a non-uniform rainfall, but one should further modify it and the infiltration rate needs to be obtained through application of an iterative procedure, which would increase the computational cost.

Chapter 3 Modeling uncertainties

Uncertainties are present in most if not all natural processes. For instance, the soil permeability and other soil properties are highly uncertain due to the inherent variability of soil (Nilsson et al. 2011; Santoso et al. 2011a) and rainfall events naturally vary randomly in time (Menabde et al. 1997). Due to the fact that these uncertainties greatly influence the pore water pressure redistribution and hence the slope stability (Yuan et al. 2015a), it is necessary to account for them in the design and assessment of slopes. Uncertainties are typically modeled with the help of probability theory. In particular, quantities that vary randomly in space (time) are modeled with random fields (processes). This chapter presents the basic theory of random fields and discusses the numerical treatment that was adopted in this thesis within the context of slope stability. This chapter draws largely upon lecture notes on stochastic finite element method (Papaioannou 2014).

3.1 Random variables and random vectors

3.1.1 Random variables

As a basic element of the random field theory, a random variable X is defined as a set function, i.e. $X: \mathcal{X} \rightarrow \mathbb{R}$, where \mathcal{X} and \mathbb{R} are the sample and real-valued space, respectively. Random variables are often applied to represent uncertain parameters subjected to given variations. The space \mathcal{X} and the random variable X can either be discrete or continuous. Discrete random variables can take outcomes from any of a specified countable list of values, whereas continuous random variables take outcomes from any numerical value in collection of intervals. Define an event $E = \{X \leq x\}$, in which x is the outcome of the experiment. The cumulative distribution function (CDF) $F_X(x)$ of the random variable X is defined as the probability of occurrence of the event E . The universal expression for both discrete and continuous random variables is:

3.1 Random variables and random vectors

$$F_X(x) = \Pr[E] = \Pr[X \leq x] \quad (3.1)$$

Eq. (3.1) indicates how the probability of the real event connects to the function space. In this thesis we will focus on continuous random variables, because the relevant uncertain quantities have continuous sample spaces. The CDF is a non-decreasing function and it satisfies that $\lim_{x \rightarrow -\infty} F_X(x) = 0$ and $\lim_{x \rightarrow +\infty} F_X(x) = 1$. In a continuous sample space, probabilities of the type $\Pr[X = x]$ are zero. Thus, according to Eq. (3.1), the probability density function (PDF) of a continuous random variable can be defined as:

$$f_X(x) = \lim_{dx \rightarrow 0} \frac{\Pr[x < X \leq x + dx]}{dx} = \frac{dF_X(x)}{dx} \quad (3.2)$$

Conversely, the CDF can be obtained as:

$$F_X(x) = \int_{-\infty}^x f_X(z) dz \quad (3.3)$$

Since $\lim_{x \rightarrow +\infty} F_X(x) = 1$, the normalization rule reads:

$$\int_{-\infty}^{\infty} f_X(x) dx = 1 \quad (3.4)$$

Let $g(X)$ be any continuous function of the random variable X . The mathematical expectation $E[g(X)]$ is given for a continuous random variable as:

$$E[g(X)] = \int_{-\infty}^{\infty} g(x) f_X(x) dx \quad (3.5)$$

The mean (expected) value of a random variable can then be defined as:

$$\mu_X = E[X] = \int_{-\infty}^{\infty} x f_X(x) dx \quad (3.6)$$

The n -th moment μ_n and n -th central moment μ'_n of X are then defined as $\mu_n = E[X^n]$ and $\mu'_n = E[(X - \mu_X)^n]$, respectively. The variance or second order central moment, denoted by $\text{Var}[X]$, and the standard deviation σ_X of X are defined as:

$$\text{Var}[X] = E[(X - \mu_X)^2] \quad (3.7)$$

$$\sigma_X = \sqrt{\text{Var}[X]} \quad (3.8)$$

The variance is a measure of the dispersion of a PDF. For random variables with non-zero mean value ($\mu_X \neq 0$), we can define the dimensionless coefficient of variation CV_X as:

$$\text{CV}_X = \frac{\sigma_X}{|\mu_X|} \quad (3.9)$$

3.1.2 Random vectors

A random vector \mathbf{X} is a mapping of the form $\mathbf{X}: \mathcal{X} \rightarrow \mathbb{R}^n$, where n is the dimension of the vector. The components of the random vector are random variables, i.e. $\mathbf{X} = [X_1, X_2, \dots, X_n]^T$, where $[\cdot]^T$ denotes the transpose operator. The joint CDF of vector \mathbf{X} is given by:

$$F_{\mathbf{X}}(\mathbf{x}) = F_{X_1, X_2, \dots, X_n}(x_1, x_2, \dots, x_n) = P(X_1 \leq x_1 \cap X_2 \leq x_2 \dots \cap X_n \leq x_n) \quad (3.10)$$

In a similar manner as Eq. (3.3), the corresponding joint PDF can be obtained by differentiation of the joint CDF as follows:

$$f_{\mathbf{X}}(\mathbf{x}) = f_{X_1, X_2, \dots, X_n}(x_1, x_2, \dots, x_n) = \frac{\partial^n F_{X_1, X_2, \dots, X_n}(x_1, x_2, \dots, x_n)}{\partial x_1 \partial x_2 \dots \partial x_n} \quad (3.11)$$

One of the important normalization properties of the joint PDF and CDF is:

$$\int_{D_{\mathbf{X}}} f_{\mathbf{X}}(\mathbf{x}) d\mathbf{x} = \int_{-\infty}^{\infty} \dots \int_{-\infty}^{\infty} f_{X_1, X_2, \dots, X_n}(x_1, x_2, \dots, x_n) dx_1 dx_2 \dots dx_n = 1 \quad (3.12)$$

in which $D_{\mathbf{X}} = \mathbb{R}^n$ and $d\mathbf{x} = dx_1 dx_2 \dots dx_n$. The marginal distribution of any random variable X_i ($1 \leq i \leq n$) is obtained by integrating the joint PDF over all remaining components:

$$f_X(\mathbf{x}) = \int_{D_{\mathbf{x}^{-1}}} f_{\mathbf{X}}(\mathbf{x}) d\mathbf{x}^{-1} \quad (3.13)$$

in which $D_{\mathbf{x}^{-1}} = \mathbb{R}^{n-1}$ and $d\mathbf{x}^{-1} = dx_1 dx_2 \dots dx_{i-1} dx_{i+1} \dots dx_n$.

3.1 Random variables and random vectors

The conditional distribution of any random variable X_i given X_j ($1 \leq i, j \leq n$) can be written as:

$$f_{X_i|X_j}(x_i|x_j) = \frac{f_{X_i, X_j}(x_i, x_j)}{f_{X_j}(x_j)} \quad (3.14)$$

We can then express the joint PDF $f_{\mathbf{X}}(\mathbf{x})$ by applying a generalized multiplication chain rule, if all conditional PDFs are known:

$$\begin{aligned} f_{\mathbf{X}}(\mathbf{x}) &= f_{X_1, X_2, \dots, X_n}(x_1, x_2, \dots, x_n) \\ &= f_{X_n|X_1, X_2, \dots, X_{n-1}}(x_n|x_1, x_2, \dots, x_{n-1}) \dots f_{X_2|X_1}(x_2|x_1) f_{X_1}(x_1) \end{aligned} \quad (3.15)$$

Two random variables X_i and X_j are said to be statistically independent if and only if $[f_{X_j}(x_j) \neq 0]$:

$$f_{X_i|X_j}(x_i|x_j) = f_{X_i}(x_i) \quad (3.16)$$

Eq. (3.16) implies that if X_i and X_j are statistically independent, then $f_{X_i, X_j}(x_i, x_j) = f_{X_i}(x_i) f_{X_j}(x_j)$ [see also Eq. (3.14)]. We can then obtain the joint PDF of a vector \mathbf{X} of jointly statistically independent random variables as follows:

$$f_{\mathbf{X}}(\mathbf{x}) = f_{X_1}(x_1) f_{X_2}(x_2) \dots f_{X_n}(x_n) = \prod_{i=1}^n f_{X_i}(x_i) \quad (3.17)$$

Consider a function $g(\mathbf{X})$ of the random vector \mathbf{X} . The mathematical expectation $E[g(\mathbf{X})]$ is defined in analogy with the definition given in Eq. (3.5) as follows:

$$E[g(\mathbf{X})] = \int_{D_{\mathbf{X}}} g_{\mathbf{X}}(\mathbf{x}) f_{\mathbf{X}}(\mathbf{x}) d\mathbf{x} \quad (3.18)$$

The covariance $\text{Cov}[X_i, X_j]$ of the random variables X_i and X_j is defined as follows:

$$\text{Cov}[X_i, X_j] = E[(X_i - \mu_{X_i})(X_j - \mu_{X_j})] \quad (3.19)$$

The dimensionless correlation coefficient of X_i and X_j is defined by normalizing

the covariance by the standard deviations of the two random variables:

$$\rho_{X_i, X_j} = \frac{\text{Cov}[X_i, X_j]}{\sigma_{X_i} \sigma_{X_j}} \in [-1, 1] \quad (3.20)$$

The covariance and correlation coefficient are measures of the linear dependence of two random variables. Two random variables X_i and X_j are said to be uncorrelated if:

$$\text{Cov}[X_i, X_j] = 0 \text{ or } \rho_{X_i, X_j} = 0 \quad (3.21)$$

It can be easily shown that if two random variables are statistically independent, then they are also uncorrelated. Notice that the reverse does not necessarily hold. The mean value vector $\mu_{\mathbf{X}}$ of a random vector \mathbf{X} is defined as the vector containing the mean value of each component random variable, namely $\mu_{\mathbf{X}} = [\mu_{X_1}, \mu_{X_2}, \dots, \mu_{X_n}]^T$.

The covariance matrix $\Sigma_{\mathbf{X}\mathbf{X}}$ and the correlation coefficient matrix $\mathbf{R}_{\mathbf{X}\mathbf{X}}$ are square symmetric and positive semi-definite matrices, defined as:

$$\Sigma_{\mathbf{X}\mathbf{X}} = \{\text{Cov}[X_i, X_j]\}_{n \times n} \quad (3.22)$$

$$\mathbf{R}_{\mathbf{X}\mathbf{X}} = [\rho_{X_i, X_j}]_{n \times n} \quad (3.23)$$

We also define the diagonal matrix $\mathbf{D}_{\mathbf{X}}$ containing the standard deviation of each component random variable, i.e. $\mathbf{D}_{\mathbf{X}} = \text{diag}[\sigma_{X_i}]_{n \times n}$. Therefore, the covariance and correlation coefficient matrices satisfy the following relation:

$$\Sigma_{\mathbf{X}\mathbf{X}} = \mathbf{D}_{\mathbf{X}} \mathbf{R}_{\mathbf{X}\mathbf{X}} \mathbf{D}_{\mathbf{X}} \quad (3.24)$$

3.2 Random fields and random processes

Engineers often use random variables to represent uncertain parameters. Nevertheless, random variables are sometimes insufficient to accurately model the stochastic behavior of physical parameters. For instance, the spatial variability of permeability within soil slopes has significant influence on the rainwater infiltration process with respect to the wetting front development. The probabilistic description of such quantities requires the

3.2 Random fields and random processes

consideration of random fields or random processes (Vanmarcke 1983; Grigoriu 2013). In this section, we discuss basic definitions of random processes and random fields and introduce strategies for their numerical treatment. It is noted that the fundamental definitions for random processes are in analogy to the ones for random fields. They can be also in space, e.g. deformation along a cross section. The only difference is that random processes represent one-dimensional problems and their time domain of definition is $[0, \infty)$ (Swain 1984).

3.2.1 Definitions

A random field $X(\mathbf{z})$ is applied to modeling spatially variable properties. A random field, $X(\mathbf{z})$ is defined as collection of random variables indexed by a spatial coordinate $\mathbf{z} \in \Omega \subset \mathbb{R}^d$ ($d = 1, 2$ or 3), in which Ω is the sample domain. For each $\mathbf{z}_i \in \Omega$, $X(\mathbf{z}_i)$ is a random variable. And for each selection of elements $\{\mathbf{z}_i, i = 1, 2, \dots, n\} \in \Omega$, the vector $[X(\mathbf{z}_1), X(\mathbf{z}_2), \dots, X(\mathbf{z}_n)]^T$ is a random vector.

Random processes are often applied to capturing the evolution of a collection of time-dependent random variables, e.g. temperature, precipitation, moisture, etc. They can be understood as a one-dimensional case of random fields, i.e. $d = 1$. Thus, in analogy to the definition of random fields, the random process $X(t)$ refers to time varying properties, in which $t \in T$ and T represents a continue set (e.g. Papaioannou 2014).

The following interpretation focuses on the definition of random field, whereas the definition of random processes can be obtained by replacing the random vector \mathbf{z} by the scalar t . Notice that, t can only take non-negative values, namely lower boundary starts from zero. Similarly to the definition of random variables, the mean function $\mu_X(\mathbf{z})$ of a random field $X(\mathbf{z})$ yields:

$$\mu_X(\mathbf{z}) = E[X(\mathbf{z})] = \int_{-\infty}^{\infty} x f_{X(\mathbf{z})}(x, \mathbf{z}) dx \quad (3.25)$$

in which $f_{X(\mathbf{z})}(x, \mathbf{z})$ is the marginal PDF of $X(\mathbf{z})$. The mean-square and variance functions of a random field $X(\mathbf{z})$ are given by:

$$E[X^2(\mathbf{z})] = \int_{-\infty}^{\infty} x^2 f_{X(\mathbf{z})}(x, \mathbf{z}) dx \quad (3.26)$$

and

$$\text{Var}[X(\mathbf{z})] = \sigma_X^2(\mathbf{z}) = E[X^2(\mathbf{z})] - (E[X(\mathbf{z})])^2 \quad (3.27)$$

in which $\sigma_X(\mathbf{z})$ is the standard deviation of $X(\mathbf{z})$. Subsequently, the concept of the second moment function or auto-correlation function $R_{XX}(\mathbf{z}_1, \mathbf{z}_2)$ is defined as the mean of the product of two random variables $X(\mathbf{z}_1)$ and $X(\mathbf{z}_2)$ for arbitrary \mathbf{z}_1 and $\mathbf{z}_2 \in \Omega$:

$$R_{XX}(\mathbf{z}_1, \mathbf{z}_2) = E[X(\mathbf{z}_1)X(\mathbf{z}_2)] \quad (3.28)$$

The auto-covariance function $\Gamma_{XX}(\mathbf{z}_1, \mathbf{z}_2)$ is expressed as:

$$\Gamma_{XX}(\mathbf{z}_1, \mathbf{z}_2) = R_{XX}(\mathbf{z}_1, \mathbf{z}_2) - \mu_X(\mathbf{z}_1) \mu_X(\mathbf{z}_2) \quad (3.29)$$

The auto-correlation coefficient function of $X(\mathbf{z})$ is defined by normalizing the auto-covariance function $\Gamma_{XX}(\mathbf{z}_1, \mathbf{z}_2)$ with the standard deviation functions \mathbf{z}_1 and \mathbf{z}_2 , i.e.

$$\rho_{XX}(\mathbf{z}_1, \mathbf{z}_2) = \frac{\Gamma_{XX}(\mathbf{z}_1, \mathbf{z}_2)}{\sigma_X(\mathbf{z}_1)\sigma_X(\mathbf{z}_2)} \quad (3.30)$$

$\rho_{XX}(\mathbf{z}_1, \mathbf{z}_2)$ is a symmetric [i.e. $\rho_{XX}(\mathbf{z}_1, \mathbf{z}_2) = \rho_{XX}(\mathbf{z}_2, \mathbf{z}_1)$], bounded [see Eq. (3.20)] and positive semi-definite function, hence $-1 \leq \rho_{XX}(\mathbf{z}_1, \mathbf{z}_2) \leq 1$. A random field $X(\mathbf{z})$ is said to be strictly homogeneous if the random variables $[X(\mathbf{z}_1), X(\mathbf{z}_2), \dots, X(\mathbf{z}_n)]$ and $[X(\mathbf{z}_1 + \boldsymbol{\delta}), X(\mathbf{z}_2 + \boldsymbol{\delta}), \dots, X(\mathbf{z}_n + \boldsymbol{\delta})]$ have the same joint distribution for any $\{n, \mathbf{z}_1, \mathbf{z}_2, \dots, \mathbf{z}_n\}$:

$$f_{X(\mathbf{z}_1), X(\mathbf{z}_2), \dots, X(\mathbf{z}_n)}(x_1, \mathbf{z}_1; x_2, \mathbf{z}_2; \dots; x_n, \mathbf{z}_n) = f_{X(\mathbf{z}_1 + \boldsymbol{\delta}), X(\mathbf{z}_2 + \boldsymbol{\delta}), \dots, X(\mathbf{z}_n + \boldsymbol{\delta})}(x_1, \mathbf{z}_1 + \boldsymbol{\delta}; x_2, \mathbf{z}_2 + \boldsymbol{\delta}; \dots; x_n, \mathbf{z}_n + \boldsymbol{\delta}) \quad (3.31)$$

in which $\boldsymbol{\delta} \in \Omega$ is an arbitrary quantity. For random processes, this term is only valid for the stationary random process. By means of this definition, one could obtain following properties of homogeneous random fields or stationary random processes:

3.2 Random fields and random processes

(1) The mean function $\mu_X(\mathbf{z})$ and standard deviation function $\sigma_X(\mathbf{z})$ are constants;

(2) The auto-correlation $R_{XX}(\mathbf{z}_1, \mathbf{z}_2)$, the auto-covariance $\Gamma_{XX}(\mathbf{z}_1, \mathbf{z}_2)$ and the auto-correlation coefficient $\rho_{XX}(\mathbf{z}_1, \mathbf{z}_2)$ are functions of δ , namely $R_{XX}(\mathbf{z}_1, \mathbf{z}_2) \rightarrow R_{XX}(\boldsymbol{\delta})$, $\Gamma_{XX}(\mathbf{z}_1, \mathbf{z}_2) \rightarrow \Gamma_{XX}(\boldsymbol{\delta})$, $\rho_{XX}(\mathbf{z}_1, \mathbf{z}_2) \rightarrow \rho_{XX}(\boldsymbol{\delta})$;

(3) The second moment functions $R_{XX}(\boldsymbol{\delta})$ are symmetric with respect to the origin, i.e. $R_{XX}(\boldsymbol{\delta}) = R_{XX}(-\boldsymbol{\delta})$.

It should be pointed out that a weakly homogeneous field (weakly stationary process) also satisfies the aforementioned conditions, yet the definition of Eq. (3.31) holds only for $n \leq 2$.

3.2.2 One-dimensional correlation model

Several models have been proposed for the auto-correlation coefficient function of one-dimensional random fields. These models can be extended to application in higher dimensions by adopting the concept of separability (e.g. Papaioannou 2014). One of the most commonly used models is the following exponential or Markovian model:

$$\rho(\tau) = e^{-\frac{|\zeta|}{\lambda}} \quad (3.32)$$

in which λ is the correlation length; ζ is the difference between locations, i.e. $\zeta = \mathbf{z}_i - \mathbf{z}_j$ where \mathbf{z}_i and \mathbf{z}_j are arbitrary locations within the domain of definition of the random field. The properties of the auto-correlation coefficient function can be found in the previous Section 3.2.1. A small correlation length indicates fast reduction of the correlation coefficient as ζ increases and it leads to high variability in the sample realizations. In contrast, a large correlation length refers to a strongly correlated field with slowly varying sample realizations. A measure of the variability of a random field that is independent of the adopted correlation model is the scale of fluctuation r defined by the integral of the autocorrelation coefficient:

$$r = \int_{\Omega} \rho_{XX}(\zeta) d\zeta \quad (3.33)$$

For the exponential model of Eq. (3.32), the scale of fluctuation can be expressed in terms of the correlation length as $r = 2\lambda$.

3.2.3 Gaussian random fields

A random field $X(\mathbf{z})$ is Gaussian if for any $\{n, \mathbf{z}_1, \mathbf{z}_2, \dots, \mathbf{z}_n\}$ the random variables $[X(\mathbf{z}_1), X(\mathbf{z}_2), \dots, X(\mathbf{z}_n)]$ are jointly Gaussian. A Gaussian random field can be completely defined by its mean function $\mu_X(\mathbf{z})$ and its auto-covariance function Σ_{XX} , i.e. $\Sigma_{XX} = [\Gamma_{XX}(\mathbf{z}_i, \mathbf{z}_j)]_{n \times n}$. The marginal PDF of a Gaussian random field is given by:

$$f_X(x, \mathbf{z}) = \frac{1}{\sigma_X(\mathbf{z})} \cdot \varphi\left(\frac{x - \mu_X(\mathbf{z})}{\sigma_X(\mathbf{z})}\right) = \frac{1}{\sigma_X(\mathbf{z})\sqrt{2\pi}} \cdot \exp\left[-\frac{(x - \mu_X(\mathbf{z}))^2}{2\sigma_X^2(\mathbf{z})}\right] \quad (3.34)$$

in which $\varphi(\cdot)$ is the marginal PDF of the standardized Gaussian random field $U(\mathbf{z})$, defined as:

$$U(\mathbf{z}) = \frac{X(\mathbf{z}) - \mu_X(\mathbf{z})}{\sigma_X(\mathbf{z})} \quad (3.35)$$

The random field $U(\mathbf{z})$ has zero mean and unit standard deviation. The joint PDF of the random variables $X(\mathbf{z}_1), X(\mathbf{z}_2), \dots, X(\mathbf{z}_n)$ corresponding to any selection of n spatial points is the multinormal PDF given by:

$$f_X(\mathbf{x}) = \frac{1}{(2\pi)^{n/2}(\det \Sigma_{XX})^{1/2}} \cdot \exp\left[-\frac{1}{2}(\mathbf{x} - \boldsymbol{\mu}_X)^T \Sigma_{XX}^{-1}(\mathbf{x} - \boldsymbol{\mu}_X)\right] \quad (3.36)$$

in which $\det(\cdot)$ is the determinant operator; $\boldsymbol{\mu}_X$ is the mean vector of the random variables, evaluated as $\boldsymbol{\mu}_X = [\mu_X(\mathbf{z}_1), \mu_X(\mathbf{z}_2), \dots, \mu_X(\mathbf{z}_n)]^T$ and Σ_{XX} is their covariance matrix computed according to Eq. (3.30):

$$\Sigma_{XX} = [\Gamma_{XX}(\mathbf{z}_i, \mathbf{z}_j)]_{n \times n} = [\rho_{XX}(\mathbf{z}_i, \mathbf{z}_j)\sigma_X(\mathbf{z}_i)\sigma_X(\mathbf{z}_j)]_{n \times n} \quad (3.37)$$

3.2.4 Non-Gaussian random fields and transformation

Consider a non-Gaussian random field $X(\mathbf{z})$. The joint distribution of any random vector $[X(\mathbf{z}_1), X(\mathbf{z}_2), \dots, X(\mathbf{z}_n)]^T$ can then be defined by the n -th order CDF of $X(\mathbf{z})$. Usually

3.2 Random fields and random processes

an incomplete definition is given by the marginal distribution $F_{X(\mathbf{z})}(x, \mathbf{z}_i)$, $i = 1, 2, \dots, n$ and the covariance matrix $\mathbf{\Sigma}_{XX} = [\Gamma_{XX}(\mathbf{z}_i, \mathbf{z}_j)]_{n \times n}$. In this case, the joint distribution of the random variables can be modeled by the Nataf transformation (Nataf 1962; Liu and Der Kiureghian 1986). If the Nataf model is adopted, $X(\mathbf{z})$ can be defined by the following transformation:

$$X(\mathbf{z}) = F_{X(\mathbf{z})}^{-1}[\Phi(U(\mathbf{z})), \mathbf{z}] \quad (3.38)$$

where $U(\mathbf{z})$ is a Gaussian random field with zero mean and unit variance and auto-correlation coefficient function $\rho_{UU}(\mathbf{z}_1, \mathbf{z}_2)$. The function $\rho_{UU}(\mathbf{z}_1, \mathbf{z}_2)$ is determined in terms of the auto-correlation coefficient function of $X(\mathbf{z})$ $\rho_{XX}(\mathbf{z}_1, \mathbf{z}_2)$ by solving the following integral equation iteratively:

$$\rho_{XX}(\mathbf{z}_1, \mathbf{z}_2) = \int_{-\infty}^{\infty} \int_{-\infty}^{\infty} \left(\frac{x(\mathbf{z}_1) - \mu_X(\mathbf{z}_1)}{\sigma_X(\mathbf{z}_1)} \right) \left(\frac{x(\mathbf{z}_2) - \mu_X(\mathbf{z}_2)}{\sigma_X(\mathbf{z}_2)} \right) \varphi_2[u_1, u_2, \rho_{UU}(\mathbf{z}_1, \mathbf{z}_2)] du_1 du_2 \quad (3.39)$$

3.2.5 Discretization of random fields

The discretization of the random field $X(\mathbf{z})$ consists in its approximation by $\hat{X}(\mathbf{z})$, where $\hat{X}(\mathbf{z})$ is defined by means of a finite set of random variables $[X_1, X_2, \dots, X_n]$. The field $\hat{X}(\mathbf{z})$ is expressed as a finite sum of products of the random variables $[X_1, X_2, \dots, X_n]$ with deterministic functions, i.e.

$$\hat{X}(\mathbf{z}) = \sum_{i=1}^n \varphi_i(\mathbf{z}) \cdot X_i \quad (3.40)$$

in which $\varphi_i(\mathbf{z})$ are the deterministic functions. The choice of $\varphi_i(\mathbf{z})$ depends on the applied discretization methods. So far, common methods for discretization mainly involve three categories: point discretization, average discretization and series expansion methods. For instance, midpoint method and Karhunen-Loève expansion belong to point discretization and series expansion method, respectively.

In point discretization methods, the random field $X(\mathbf{z})$ can be approximated by using the random variables $[X_1, X_2, \dots, X_n]$ that correspond to the values

$[X(\mathbf{z}_1), X(\mathbf{z}_2), \dots, X(\mathbf{z}_n)]$ of $X(\mathbf{z})$ at discrete points of the entire domain Ω . These points are based on the selection of a mesh Ω_d , consisting of a finite number of elements Ω_e . Subsequently, the relative point-wise variance discretization error is defined as:

$$err_{r-\text{Var}} = \frac{\text{Var}[X(\mathbf{z}) - \hat{X}(\mathbf{z})]}{\text{Var}[X(\mathbf{z})]} \quad (3.41)$$

in which the point-wise variance is given by:

$$\begin{aligned} err_{\text{Var}}(\mathbf{z}) &= \text{Var}[X(\mathbf{z}) - \hat{X}(\mathbf{z})] \\ &= \sigma_X^2(\mathbf{z}) + \text{Var}[\sum_{i=1}^n \varphi_i(\mathbf{z})X_i] - 2\text{Cov}[X(\mathbf{z}), \sum_{i=1}^n \varphi_i(\mathbf{z}) \cdot X_i] \end{aligned} \quad (3.42)$$

In the midpoint method, the locations $[\mathbf{z}_1, \mathbf{z}_2, \dots, \mathbf{z}_n]$ are chosen at the midpoints (centers of gravity) of the elements Ω_i (Der Kiureghian and Ke 1988). Figure 3.1 represents one example of a discretization in one dimension by the mid-point method. The random field $X(\mathbf{z})$ over each element Ω_i is approximated by its value $\hat{X}(\mathbf{z}) = X_i = X(\mathbf{z}_i)$ at the midpoints \mathbf{z}_i , i.e.

$$\varphi_i(\mathbf{z}) = \begin{cases} 1, & \text{if } \mathbf{z} \in \Omega_i \\ 0, & \text{else} \end{cases} \quad (3.43)$$

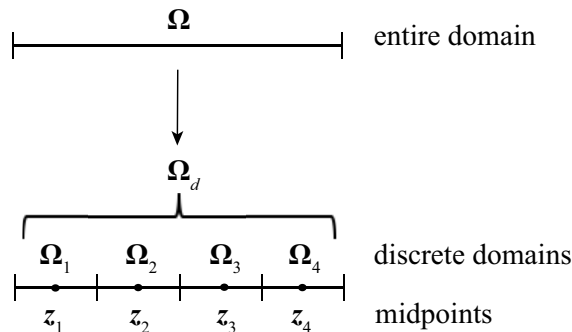


Figure 3.1 Midpoints of the element Ω_i .

Consider the case where the random field has been defined in terms of an underlying Gaussian random field, which has been discretized with the midpoint method. In this case, one can generate sample functions of the random field through generating

3.2 Random fields and random processes

samples of the correlated Gaussian random variables corresponding to the midpoints of the stochastic element mesh. Samples of the non-Gaussian field can then be obtained by transforming the samples of the Gaussian field through application of Eq. (3.38) (see Section 3.2.3). Generating samples of correlated Gaussian random variables $X \sim N(\boldsymbol{\mu}_X, \boldsymbol{\Sigma}_{XX})$ can be achieved by generating independent standard normal random variables $U \sim N(0,1)$ and transforming them to samples of X applying the Cholesky decomposition method. For a positive definite covariance matrix $\boldsymbol{\Sigma}_{XX}$, one can perform its Cholesky decomposition:

$$\boldsymbol{\Sigma}_{XX} = \mathbf{L}\mathbf{L}^T \quad (3.44)$$

in which \mathbf{L} is a lower triangular matrix with strictly positive diagonal entries. One can show that the following transformation applies:

$$\mathbf{X} = \boldsymbol{\mu}_X + \mathbf{L}\mathbf{U} \quad (3.45)$$

Another strategy of generating correlated Gaussian random variables is to apply the spectral decomposition method. This approach can also be employed for decreasing the number of random variables of the problem, which is beneficial for several methods for probabilistic and reliability assessment (see Chapter 5). The essential idea of applying this method is based on the spectral decomposition of the covariance matrix of the random variables, which reads

$$\boldsymbol{\Sigma}_{XX} = \sum_{i=1}^n \sqrt{\lambda_i} \mathbf{v}_i \mathbf{v}_i^T \quad (3.46)$$

in which λ_i is the i th non-negative eigenvalue of the covariance matrix; \mathbf{v}_i is the normalized eigenvector corresponding to the eigenvalue λ_i . For an arbitrary $n \times 1$ vector \mathbf{e}_k and diagonal matrix $\boldsymbol{\Lambda} = \text{diag}[\lambda_1, \lambda_2, \dots, \lambda_n]$, it holds that:

$$\boldsymbol{\Sigma}_{XX} \mathbf{e}_k = \boldsymbol{\Lambda} \mathbf{e}_k \quad (3.47)$$

Then, the random vector can be exactly expressed in terms of n independent standard normal random variables as follows

$$\mathbf{X} = \boldsymbol{\mu}_X + \sum_{i=1}^n \sqrt{\lambda_i} \mathbf{v}_i X_i \quad (3.48)$$

The above expression can be used to decrease the number of random variables in the problem by arranging the eigenvalues and eigenvectors in decreasing order of magnitude of the eigenvalues and truncating the expression after the $M < n$ largest eigenterms. In this way, fewer terms can be used in the representation of the random field and hence the modeling dimensions can be reduced considerably. Truncation of Eq. (3.48) leads to an approximation of the vector $X(\mathbf{z})$, denoted by $\hat{X}(\mathbf{z})$. This introduces an additional error in the random field approximation, which can be quantified by the relative variance error given by (e.g. Betz et al. 2014).

$$err_{r-var} = \frac{\text{Var}[X(\mathbf{z}) - \hat{X}(\mathbf{z})]}{\text{Var}[X(\mathbf{z})]} = \frac{\sum_{i=M+1}^n \lambda_i \mathbf{v}_i^2}{\sum_{i=1}^n \lambda_i \mathbf{v}_i^2} \quad (3.49)$$

Commonly, the choice of M is accepted when the error is less than 0.05.

3.3 Modeling permeability of soil layers as random fields

In this thesis, the focus is on the pore water pressure, which varies with time and space due to rainwater infiltration. Within this study, we assume the infiltration process, which affects the pore water pressure p_w during the wetting front development, is governed by the vertical saturated hydraulic conductivity K_s and the suction head S of the soil. In this thesis, we account for the vertical variability of these two parameters in the extended Green and Ampt model. When using Richards equation, we only consider the saturated hydraulic conductivity K_s as a random field.

Most soil properties, and in particular soil permeability, are highly heterogeneous (Vogel et al. 2000). The saturated hydraulic conductivity within soil layers is often assumed to follow a lognormal distribution (Gelhar 1986; Skaggs and Barry 1997). Here, we model the saturated hydraulic conductivities of the soil column $K_s(z)$ in the direction perpendicular to the ground surface as a one-dimensional homogeneous lognormal random field. Hence, the decimal logarithms of the parameters $\log_{10}K$ and $\log_{10}S$ are modeled as homogeneous Gaussian random fields, with the assumption that the

3.3 Modeling permeability of soil layers as random fields

autocorrelation coefficient function of the logarithms of both fields is given by the following exponential model (Vanmarcke 1983):

$$\rho(\tau) = e^{-\frac{2|\zeta|}{r}} \quad (3.50)$$

where ζ is the absolute distance between two locations in the vertical direction. Notice that the parameters in this equation are the same as in Eqs. (3.32) and $r = 2\lambda$. The scale of fluctuation is a measure of the spatial variability of the random field. A scale of fluctuation that is much larger than the depth of the soil slice implies a uniform soil profile; in such a case, the saturated hydraulic conductivity and suction head can be modeled each by a single random variable instead of random field. In the extreme case where the scale of fluctuation is close to zero, the values of each random property become independent of each other at all locations. Figure 3.2 shows one possible realizations of a Gaussian random field representing the decimal logarithm of the saturated hydraulic conductivity of a soil column for scales of fluctuation of 0.5m and of 5m, respectively. One can observe that the spatial variability is higher as the scale of fluctuation becomes smaller. The lower bound of scale of fluctuation depends on the random field discretization, namely the size of random cells, which is the fundamental element of random fields and defined having equal length in this study.

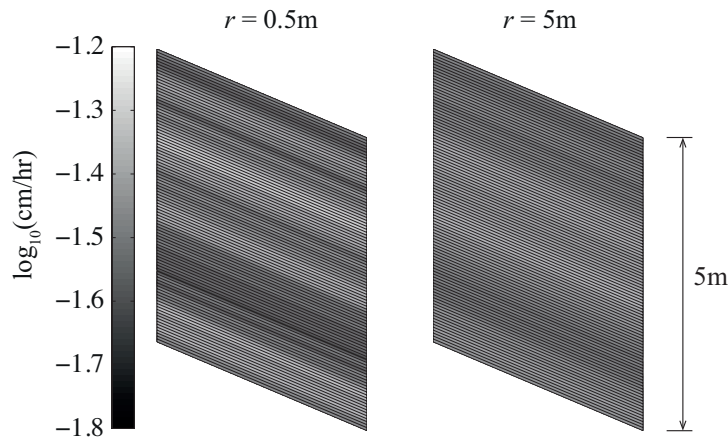


Figure 3.2 Realizations of $\log_{10}K_s$ for different scales of fluctuation.

The cross-correlation coefficient function, describing the cross-correlation of the logarithms of the two random fields at locations separated by ζ is given by:

$$\rho_{cross}(\zeta) = \rho_c \cdot \rho(\zeta) \quad (3.51)$$

where ρ_c is the point-wise cross-correlation coefficient between the two fields. The saturated hydraulic conductivity and suction head are negatively correlated because the suction tends to increase as the soil becomes less permeable, hence typically $-1 < \rho_c < 0$.

The continuous random fields are discretized by the midpoint method. The unit slice is divided into a number n layers of equal-thickness. Each randomized property is assumed to be constant within each layer, represented by the random variable corresponding to the value of the random field at the midpoint of the layer. Hence the two random fields are represented by a total of $2n$ random variables, gathered in a random vector X . Assuming statistically homogenous fields, the means $\mu_{\log_{10}K_s}$, $\mu_{\log_{10}S}$ and standard deviations $\sigma_{\log_{10}K_s}$, $\sigma_{\log_{10}S}$ of the random variables are constant over the entire random field. The entries of the $[2n \times 2n]$ correlation matrix \mathbf{R} of the logarithms of the soil properties at each layer are evaluated as follows:

$$\mathbf{R} = [R_{pq}]_{2n \times 2n} = \begin{bmatrix} [\rho(\zeta_{pq})]_{n \times n} & [\rho_{cross}(\zeta_{pq})]_{n \times n} \\ [\rho_{cross}(\zeta_{pq})]_{n \times n} & [\rho(\zeta_{pq})]_{n \times n} \end{bmatrix}_{2n \times 2n} \quad (3.52)$$

where τ_{pq} is the distance between the midpoints of two layers p and q . Simulation from the joint Gaussian distribution of random variables corresponding to the discrete layers with correlation matrix \mathbf{R} is performed by the Cholesky decomposition method (Horn and Johnson 1985). In order to obtain samples from the soil parameters, we take the 10-power of the samples from the joint Gaussian distribution. The number of layers n should be chosen such that the variability of the random field, described by the auto- and cross-correlation functions, is adequately represented. Common measures for the representation of random fields are the mean-square or variance errors. For the midpoint method and the applied exponential correlation model, the relative variance error becomes smaller than

3.4 Modeling rainfall events as random processes

10% for an element size smaller than one tenth of the scale of fluctuation (Li and Der Kiureghian 1993).

3.4 Modeling rainfall events as random processes

Commonly, uniformly distributed rainfall events are used in precipitation simulations for slope stability analysis (Zhang et al. 2005; Huang et al. 2013; Ali et al. 2014). These are parameterized by their intensity and duration. To simplify the computation, it is often assumed that the precipitation rate is larger than the water capacity of the slope, such that infiltration is controlled by the water capacity (Iverson 2000; Chen and Young 2006). In contrast, realistic rainfall patterns are usually characterized by high intermittency combined with long-range correlation (Menabde et al. 1997). These phenomena can be captured accurately through application of self-similar random process theory.

The basic idea of self-similarity is that the distribution of a quantity averaged over a given time period can be obtained by scaling down the distribution of the same quantity averaged over a longer time period. Self-similar random rainfall events can be simulated by application of the break down coefficients (BDC) concept (Menabde and Murugesu 2000). The time period of interest is divided into a number of basic cells. The simulation begins first with a uniformly distributed rainfall, whose pattern is described in terms of an average intensity and duration. At each simulation step, the rainfall event is scaled down into cells with shorter duration. The intensity of rainfall in each cell is then obtained as the average rainfall intensity multiplied by the corresponding break down coefficient (see Fig. 3.3).

Dry periods within a single rainfall event are ignored in this study, and therefore the random rainfall event is constructed by a series of discretized rainfall cells without interruption. It is noted that dry periods can be accounted for through a discrete random process model (Menabde and Murugesu 2000). The duration of each basic cell is set to $s_0 = 0.1\text{hr}$. According to the self-similar stochastic behavior of the rainfall event, the break down coefficient is defined as:

$$U(s, t) = \frac{R_s(t_1)}{R_t(t_2)}, \quad s < t \quad (3.53)$$

in which $R_s(t_1)$ and $R_t(t_2)$ are the accumulated precipitations over the rainfall durations s and t and centered at t_1 and t_2 , respectively. The coefficient $U(s, t)$ is a random variable, whose distribution depends on the ratio s/t . Here, U is modeled by a Beta distribution, whose two parameters have the same value a , i.e. $U \sim B(a, a)$.

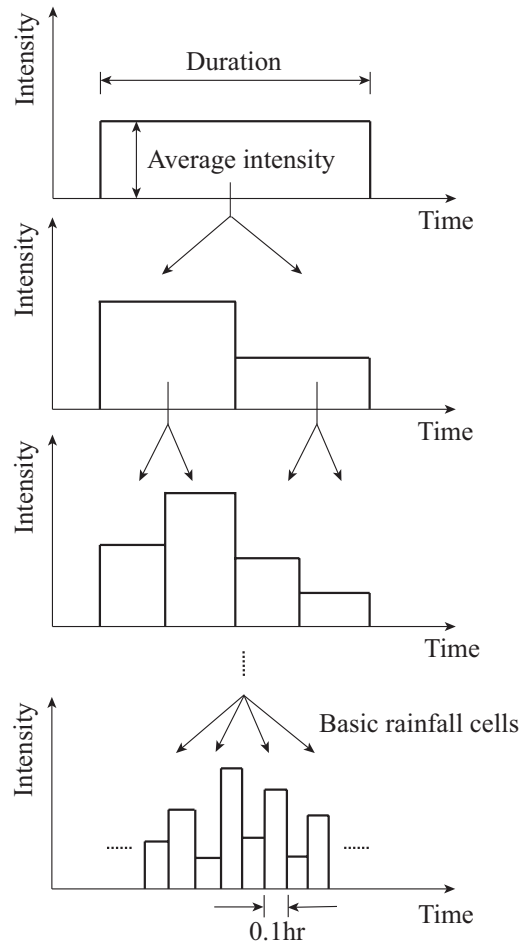


Figure 3.3 Random rainfall generation process by means of the break down coefficient concept. At the first step, the total rainfall volume is (randomly) distributed into two cells according to Eq. (3.53). The volume in each cell is further subdivided into two cells, again following Eq. (3.53). This process is repeated until the duration of the cells reaches 0.1hr.

The parameter a changes with the timescale parameter s (Menabde and Murugesu 2000):

3.4 Modeling rainfall events as random processes

$$a(s) = a_0 s^{-H} \quad (3.54)$$

in which a_0 is a dimensionless constant and $H \in (0,1)$ is the so-called Hurst parameter. These parameters can be estimated by data regression analysis for a certain region (Menabde and Murugesu 2000).

At each step of the simulation procedure, the rainfall event is divided into two cells of equal duration. The break down coefficient of each cell with duration s is obtained by simulating two random variables Y_1 and Y_2 , which follow the Beta distribution with parameter $a(s)$ and satisfy $Y_1 + Y_2 = 1$. The latter condition ensures that the accumulative precipitation of the random rainfall event is unchanged. The process is repeated N times, until the duration of each cell reaches the duration of the basic cell s_0 . The rainfall intensity in each basic cell is obtained as

$$R_i = R U_i \quad i = 1, 2, \dots, 2^N \quad (3.54)$$

in which R is the average precipitation intensity over the given duration; the subscript i indicates the basic rainfall cell; N is the number of downscaling steps. Following this procedure, the break down coefficient is:

$$U_i = \prod_{j=1}^N Y_{j,i} \quad (3.55)$$

in which $Y_{j,i}$ is the Beta random variable associated with the downscaling of the breakdown coefficient at the j th scaling down step and corresponding to the i th rainfall cell. Notice that a total of $2 + 4 + \dots + 2^N = 2^{N+1} - 2$ random variables $Y_{j,i}$ are required for generating one rainfall event. Figure 3.4 shows a random realization of a rainfall event with $N = 5$ and duration $2^N s_0 = 3.2$ hr. The average rainfall intensity is 3cm/hr.

Eq. (3.53) governs the variability of the precipitation intensity during a rainfall event. The parameter a controls the variance of the Beta distribution that models the breakdown coefficient. The variance decreases with increasing a . The parameter a_0 controls the magnitude of a , while H controls its slope in the log-scale.

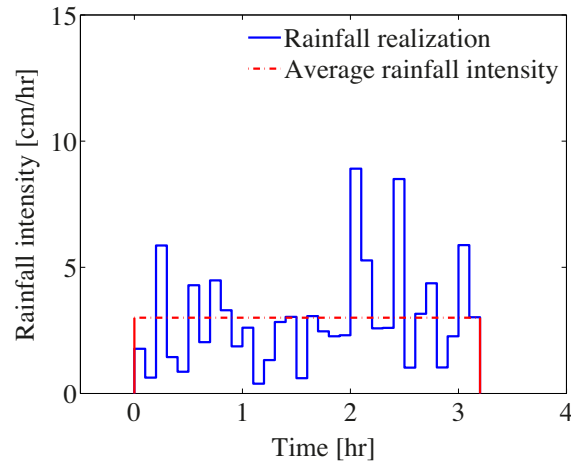


Figure 3.4 One realization of a random rainfall event with $N = 5$ downscaling steps and total duration $2^N s_0 = 3.2$ hr, in which $a_0 = 12.27$, $H = 0.47$ (Menabde and Murugesu 2000).

To demonstrate the influence of the parameters a_0 and H on the variability of the rainfall patterns, we look at a random realization of a rainfall event for a fixed duration with $N = 6$ downscaling steps, duration $2^N s_0 = 6.4$ hr, and varying values of a_0 and H . In Figure 3.5 (a)-(d), realizations obtained for a fixed $H = 0.1$ and different values of a_0 are shown, while Figure 3.4 (e)-(h) illustrates the realizations obtained with a fixed $a_0 = 10$ and different values of H . It is observed from Figure 3.4 (a)-(d) that, the variability of the intensity of rainfall cells is reduced as a_0 increases. In the limit as $a_0 \rightarrow \infty$, the variance of the breakdown coefficient tends to zero and hence the corresponding realization tends to a uniformly distributed rainfall event. If $H \rightarrow 0$, the time variability of the intensity of rainfall cells will reduce and $a \approx a_0$ [see Fig. 3.4 (b), (e)].

3.4 Modeling rainfall events as random processes

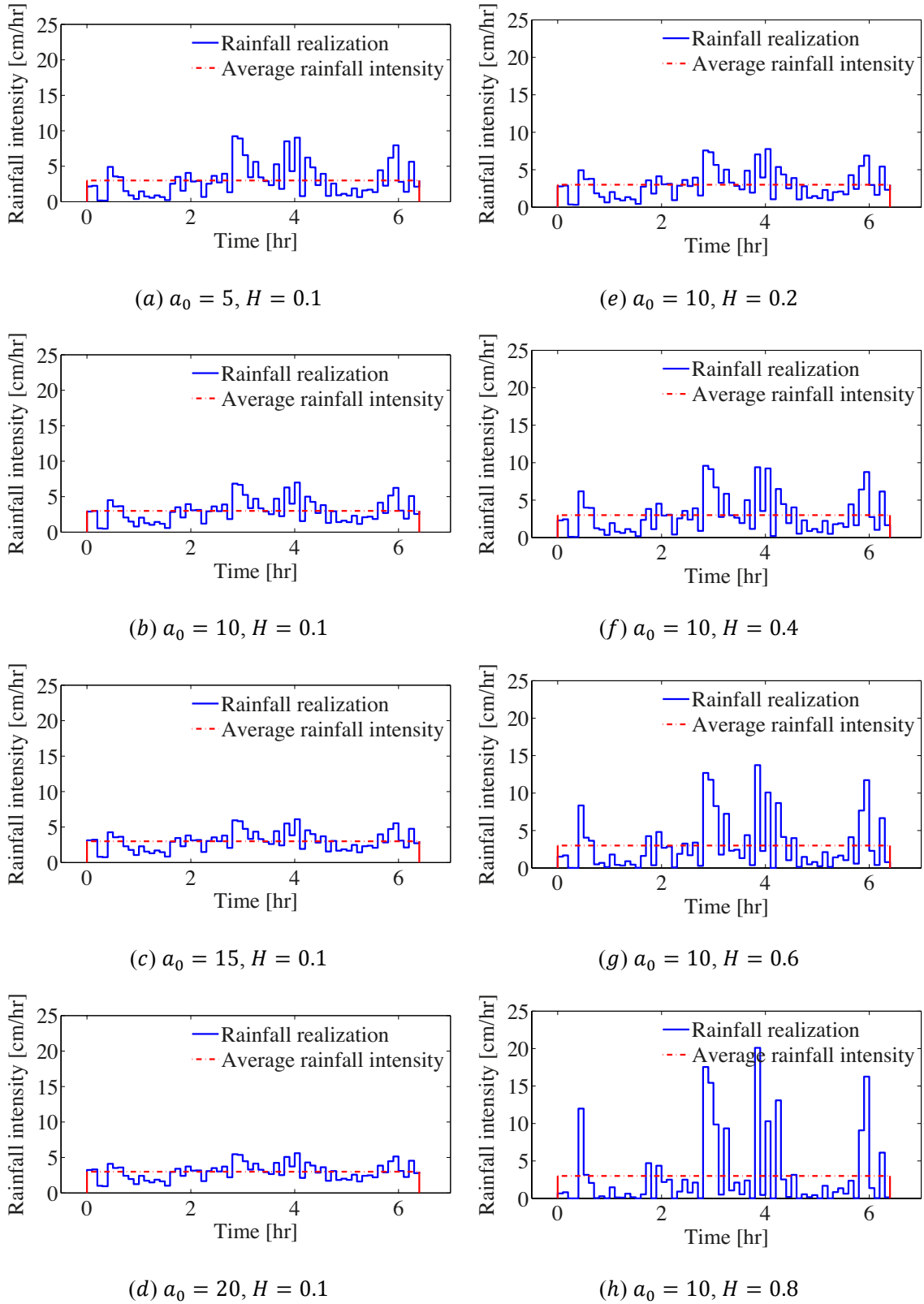


Figure 3.5 Random rainfall realizations with different a_0 and H .

Chapter 4 Reliability analysis

Reliability analysis provides a consistent means to assess the safety of slopes (Ang and Tang 1984; Christian et al. 1994). Therein, uncertainties are explicitly accounted for and modelled with probability distributions. The probability of failure of the slope is evaluated through repeated calculations of the deterministic model for possible outcomes of the uncertain variables. A proper reliability assessment can enhance engineering design and management, particularly in cases where uncertainties dominate the slope stability.

As presented in Chapter 3, random field and random process models can be applied to capture the stochastic nature of hydrogeological and geotechnical properties. The probabilistic assessment of a slope is commonly performed with Monte Carlo Simulation (Griffiths and Fenton 2004; Leynaud and Sultan 2010; Griffiths et al. 2011). In the past, application of the Monte Carlo method was restricted due to limited computation capability of the computer. For instance, the engineer might wait a few weeks for outcomes with relatively small probability when using Monte Carlo Simulation, i.e. when directly embedding the stochastic realizations into numerical models. Alternative methods based on either approximations of the geotechnical model or sampling at important regions of the probability space have been developed to enhance computational efficiency (Ching et al. 2009; Au and Wang 2014; Straub et al. 2016).

Nowadays, with fast development of computer technology and novel optimal methodologies, efficient computation is viable. One of the most effective sampling methods is Subset Simulation (Au and Beck 2001), which is an adaptive Monte Carlo method that samples adaptively the failure domain in the probability space through Markov chain Monte Carlo sampling (Papaioannou et al. 2015). This chapter discusses the basic definition of the reliability problem and its solution with the Subset Simulation method for the slope-infiltration models presented in Chapter 2.

4.1 Basic definition

4.1 Basic definition

This section presents the basic concept of the reliability analysis and its applications on slopes. The state of slopes can be evaluated by limit state functions g , such that positive values of the limit state function $g > 0$ correspond to satisfactory performance, whereas negative values correspond to failure, i.e. $g < 0$. Commonly, the limit state function can be defined in terms of the driving forces D and the resistance forces R (see Chapter 2). Failure occurs when D exceeds R , i.e. $F = \{D > R\} = \{R - D < 0\}$. It follows that the limit state function reads:

$$g(D, R) = R - D \quad (4.1)$$

The failure event is defined as $g < 0$, thereby the probability of the failure is the integral of the joint PDF of D and R over the failure domain (see Fig. 4.1):

$$P_f = \Pr[g(D, R) < 0] = \iint_{r-d < 0} f_{R,D}(r, d) dr dd \quad (4.2)$$

If the two variables are statistically independent, then the joint PDF is expressed as:

$$f_{R,D}(r, d) = f_R(r) f_D(d) \quad (4.3)$$

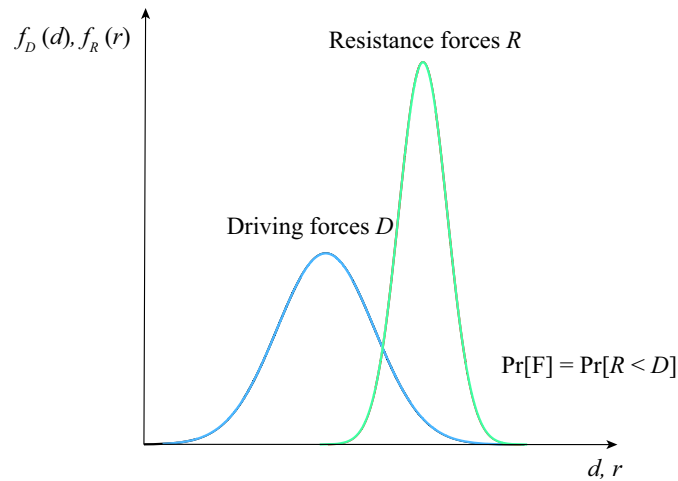


Figure 4.1 The basic slope reliability problem.

In this case, Eq. (4.2) becomes:

$$P_f = \int_{-\infty}^{\infty} \left[\int_{-\infty}^{r < d} f_R(r) dr \right] f_D(d) dd \quad (4.4)$$

An alternative equivalent definition of the limit state function g can be obtained by dividing Eq. (4.1) with the driving force D , leading to

$$g(D, R) = \frac{R}{D} - 1 = FS - 1 \quad (4.5)$$

where FS is the factor of safety of the slope, defined in Chapter 2. In general, the factor of safety will depend on multiple input parameters, e.g. strength, hydrogeological and loading parameters. The uncertain parameters can be gathered in a vector of random variables \mathbf{X} with joint PDF $f_{\mathbf{X}}(\mathbf{x})$. The limit state function is then expressed as a function of \mathbf{X} :

$$g(\mathbf{X}) = FS(\mathbf{X}) - 1 \quad (4.6)$$

The probability of failure can be evaluated by integrating $f_{\mathbf{X}}(\mathbf{x})$ at the failure domain:

$$P_f = \int_{g(\mathbf{x}) \leq 0} f_{\mathbf{X}}(\mathbf{x}) d\mathbf{x} \quad (4.7)$$

Eq. (4.2) can be efficiently solved by the First or Second Order Reliability Methods (FORM or SORM) (Hohenbichler and Rackwitz 1983; Hohenbichler and Rackwitz 1988; Breitung 2015). The accuracy of these methods can be limited in nonlinear problem, but they can be combined with sampling based methods to improve performance in these cases (Rackwitz 2001). Alternatively, direct simulation approaches based on the Monte Carlo method can be applied. One advantage of the basic Monte Carlo method is that its performance is the same also in higher dimensions. However, the efficiency of Monte Carlo Simulation becomes low if the event of interest has a small probability of occurrence. A number of advanced simulation methods have been developed to overcome this problem (e.g. Au and Beck 2001; Ching et al. 2009; Papaioannou et al. 2016; Straub et al. 2016). In particular, the Subset Simulation method

4.2 Probabilistic transformation

is an adaptive Monte Carlo method that performs efficiently for estimating rare events in high dimensional problems (Au and Beck 2001).

4.2 Probabilistic transformation

For most reliability methods, it is convenient to transform from the original probability space of the input random variables \mathbf{X} to an equivalent space of independent standard normal random variables \mathbf{U} . In this section, the transformation rule used to map from the original space \mathbf{X} to \mathbf{U} -space is discussed.

Consider the case of a single random variable. Let random samples U follow the standard normal distribution [i.e. $U \sim N(0,1)$]. We seek a one-to-one function $X = T(U)$ such that the random variables X and U have the same CDF values for every possible outcome. Assume that X has a strictly increasing CDF $F_X(x)$. It must hold:

$$F_X(T(u)) = F_U(u) = \Phi(u) \quad (4.8)$$

The sought transformation is:

$$T(u) = F_X^{-1}(F_U(u)) = F_X^{-1}(\Phi(u)) \quad (4.9)$$

in which $F_X^{-1}(\cdot)$ is the inverse operator of the CDF of X . Therefore, the sampling proceeds by generating a sample u_i of U and then computing the corresponding sample x_i of X by $x_i = T(u_i) = F_X^{-1}(\Phi(u_i))$. For example, Figure 4.2 illustrates the transformation from the standard normal space to a uniform distribution $U(0,1)$.

For the case with multiple random variables, consider sampling from a vector of jointly normal distributed random variables $\mathbf{X} = [X_1, X_2, \dots, X_n]^T$, with mean vector \mathbf{M}_X and covariance matrix Σ_{XX} . Notice that, the covariance matrix Σ_{XX} is expressed as:

$$\Sigma_{XX} = \begin{bmatrix} \sigma_{X_1}^2 & \rho_{X_1 X_2} \sigma_{X_1} \sigma_{X_2} & \cdots & \rho_{X_1 X_n} \sigma_{X_1} \sigma_{X_n} \\ \rho_{X_2 X_1} \sigma_{X_1} \sigma_{X_2} & \sigma_{X_2}^2 & \cdots & \rho_{X_2 X_n} \sigma_{X_2} \sigma_{X_n} \\ \vdots & \vdots & \ddots & \vdots \\ \rho_{X_n X_1} \sigma_{X_1} \sigma_{X_n} & \rho_{X_n X_2} \sigma_{X_2} \sigma_{X_n} & \cdots & \sigma_{X_n}^2 \end{bmatrix} \quad (4.10)$$

in which $\rho_{X_i X_j}$ ($i, j = 1, 2, \dots, n$) is the correlation coefficient, e.g. estimated by Eq. (3.32), and $\rho_{X_i X_j} = \rho_{X_j X_i}$; σ_{X_i} is the standard deviation of X_i .

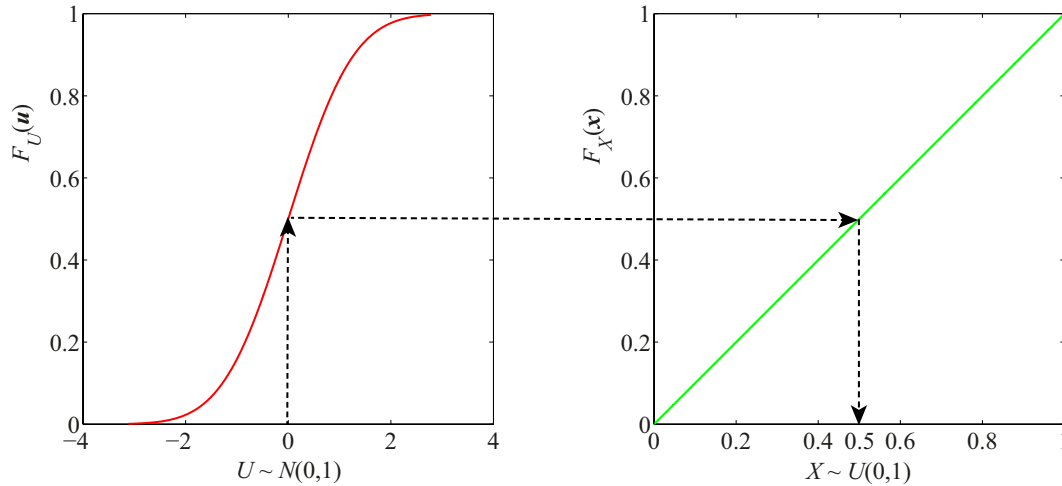


Figure 4.2 Transformation from a standard normal space $N(0,1)$ to a uniform distribution $U(0,1)$.

The vector \mathbf{X} can be transformed to a vector of independent standard normal random variables $U = [U_1, U_2, \dots, U_n]^T$ by the Cholesky decomposition method. The covariance matrix $\Sigma_{\mathbf{X}\mathbf{X}}$ can be split up into a diagonal matrix of standard deviations \mathbf{D}_X , i.e. $\mathbf{D}_X = \text{diag}(\sigma_{X_1}, \sigma_{X_2}, \dots, \sigma_{X_n})$, and a matrix of correlation coefficients $\mathbf{R}_{\mathbf{X}\mathbf{X}}$, so that $\Sigma_{\mathbf{X}\mathbf{X}} = \mathbf{D}_X \mathbf{R}_{\mathbf{X}\mathbf{X}} \mathbf{D}_X$. One then computes the lower triangle matrix \mathbf{L} by a Choleski decomposition of the matrix $\mathbf{R}_{\mathbf{X}\mathbf{X}}$, so that $\mathbf{L}\mathbf{L}^T = \mathbf{R}_{\mathbf{X}\mathbf{X}}$. Notice that the decomposition is possible when the matrix $\mathbf{R}_{\mathbf{X}\mathbf{X}}$ is positive-definite. Thus,

$$\mathbf{X} = \mathbf{M}_X + \mathbf{D}_X(\mathbf{L}\mathbf{U}) \quad (4.11)$$

Alternatively, the discrete Karhunen-Loève (KL) expansion can be applied, based on the spectral decomposition of $\Sigma_{\mathbf{X}\mathbf{X}} = \mathbf{D}_X \mathbf{R}_{\mathbf{X}\mathbf{X}} \mathbf{D}_X$. The more detailed description can be found in Chapter 2.

For a general case where the probabilistic description of the random vector \mathbf{X} is given in terms of marginal distribution and correlations, the transformation to an underlying independent standard normal vector can be achieved through application of the Nataf model. This transformation involves applying Eq. (4.9) for every component of

4.3 Monte Carlo Simulation

X. The resulting vector is assumed to follow the multivariate normal distribution with zero mean vector, unit variances and correlation matrix evaluated through the solution of an integral equation [see Eq. (3.39)]. This vector is further transformed to a standard normal vector with independent components through application of the Cholesky or spectral decomposition methods.

4.3 Monte Carlo Simulation

Monte Carlo Simulation is one of classical approaches for handling probabilistic assessment problems. The kernel of this method is to generate random samples according to the distribution of the input random vector **X**. For each sample, the deterministic model (e.g. factor of safety) is evaluated and statistical analysis using the obtained samples is performed. It is often convenient to generate samples from an equivalent independent standard normal space and subsequently map them to samples from the prescribed distribution. To this end, the transformation rule presented in Section 4.2 is used.

The fundamental steps for the MCS-based reliability analysis are summarized as follows: 1) Generate n_s random vectors **U** from the jointly standard normal distribution $\varphi_n(\mathbf{u})$; 2) Transform vectors **U** to the desired distribution of variables **X** according to the procedure described above; 3) Evaluate the function $g(\mathbf{x}_i), i = 1, 2, \dots, n_s$; 4) Count the number of failed vectors n_F , namely the vectors for which $g(\mathbf{x}_i) < 0$; 5) Compute the probability of failure by dividing the failed vectors with the total number of vectors.

Formally, we can write the MCS approximation to the probability of failure as:

$$P_f \approx p_{MC} = \frac{1}{n_s} \sum_{i=1}^{n_s} I[g(\mathbf{x}_i) < 0] = \frac{n_F}{n_s} \quad (4.12)$$

where \mathbf{x}_i are samples drawn from the joint distribution of **X** and $I[\cdot]$ is the indicator function:

$$I[g(\mathbf{x}_i) < 0] = \begin{cases} 1, & g(\mathbf{x}_i) < 0 \\ 0, & \text{else} \end{cases} \quad (4.13)$$

The coefficient of variation of the Monte Carlo estimate is as follows:

$$CV_{p_{MC}} = \sqrt{\frac{1-P_f}{n_s P_f}} \quad (4.14)$$

Notice that $CV_{p_{MC}}$ does not depend on the dimension of the random variable space. However, $CV_{p_{MC}}$ becomes large for small values of P_f . Therefore, the Monte Carlo method is inefficient for estimating small failure probabilities.

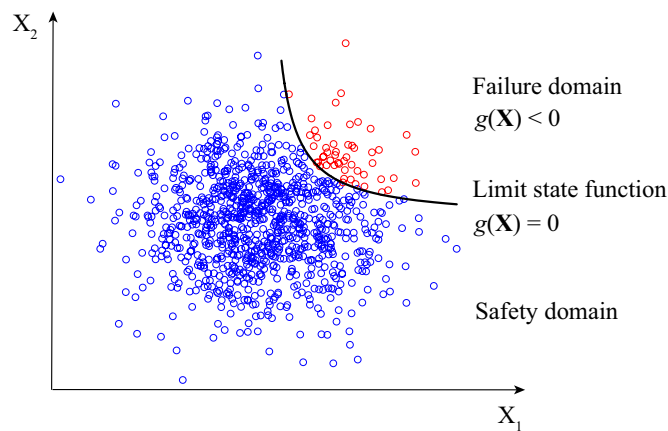


Figure 4.3 Monte Carlo Simulation for estimating the probability of failure.

4.4 Subset Simulation

The continuous random fields modeling the spatial variability of the permeability parameters of the soil are represented by random variables corresponding to the midpoints of the discrete soil layers (see Chapter 2). If the random fields have a relatively small scale of fluctuation, a large number of random variables will be required in order to capture their point-to-point variability (see Li and Der Kiureghian 1993). Efficient estimation of the failure probability in high dimensional problems can be achieved by application of Subset Simulation (Au and Beck 2001).

Subset Simulation is an adaptive Monte Carlo method that estimates probabilities of rare events efficiently independent of the number of random variables. To utilize fewer samples in computations, it is reasonable to express rare events in terms of a series of

4.4 Subset Simulation

more frequent events and this is the essence of Subset Simulation. In this regard, a series of strictly nested domains can be constructed for connecting a series of intermediate events with relatively high frequency of occurrence to the rare event. The probability of the rare event is expressed as a product of the conditional probabilities of each of the intermediate events conditional on the occurrence of the previous event in the sequence. Estimation of the conditional probabilities can be achieved by means of Markov chain Monte Carlo (MCMC) sampling (Papaioannou et al. 2015).

Suppose F is a rare event. The key idea behind Subset Simulation is to express the event F as the intersection of M intermediate events:

$$F = \bigcap_{j=1}^M F_j \quad (4.15)$$

Notice that, the intermediate events are strictly nested, i.e. $F_1 \supset F_2 \supset \dots \supset F_M$ and $F_M = F$. The probability of rare event F is estimated as a product of conditional probabilities:

$$P_f = \Pr[F] = \Pr[\bigcap_{j=1}^M F_j] = \prod_{j=1}^M \Pr[F_j|F_{j-1}] \quad (4.16)$$

where F_0 is the certain event. As with the Monte Carlo method, estimation can be performed in standard normal space \mathbf{U} with joint PDF $\varphi_n(\mathbf{u})$. The intermediate events are selected such that the conditional probabilities $\Pr[F_j|F_{j-1}]$ are large. This is achieved by sampling each domain F_{j-1} and selecting the domain $F_j = [g(\mathbf{x}) < b_j]$ such that $\Pr[F_j|F_{j-1}]$ equals a target value p_0 , where $b_1 > b_2 > \dots > b_M = 0$. Typically p_0 is chosen as $p_0 = 0.1$. The probability $\Pr[F_1|F_0]$ is computed by application of crude Monte Carlo through simulating independent and identically distribution (i.i.d) samples from $\varphi_n(\mathbf{u})$. For estimating the probabilities $\{\Pr[F_j|F_{j-1}]: j = 2, \dots, M\}$, one needs to generate samples from the conditional PDFs $\{\varphi_n(\mathbf{u}|F_{j-1}): j = 2, \dots, M\}$, where:

$$\varphi_n(\mathbf{u}|F_{j-1}) = \frac{\varphi_n(\mathbf{u})I_{F_{j-1}}(\mathbf{u})}{\Pr[F_{j-1}]} \quad (4.17)$$

wherein $I_{F_{j-1}}(\mathbf{u})$ is the indicator function of F_{j-1} . This is achieved by application of

MCMC sampling. The basic idea of MCMC sampling is to construct a Markov chain with stationary distribution equal to the target distribution. Starting from a sample \mathbf{u}_0 that lies in F_{j-1} , a sample that follows $\varphi_n(\mathbf{u}|F_{j-1})$ can be obtained by the following algorithm (Papaioannou et al. 2015):

1. Generate candidate sample $\mathbf{v} = (v_1, \dots, v_n)$ from $\varphi_n(\cdot)$.

For each $i = 1, \dots, n$, generate v_i from the normal distribution with mean

$$\rho_i u_{0i} \text{ and standard deviation } \sqrt{1 - \rho_i^2}$$

2. Accept or reject \mathbf{v}

$$\mathbf{u}_1 = \begin{cases} \mathbf{v}, & \mathbf{v} \in F_j \\ \mathbf{u}_0, & \mathbf{v} \notin F_j \end{cases}$$

The above algorithm is termed conditional sampling Metropolis-Hastings algorithm. The parameters $\rho_i, i = 1, 2, \dots, n$, model the correlation of each component of \mathbf{U} between two subsequent states of the Markov chain. For probabilities in the order $10^{-2} \sim 10^{-6}$, the choice of $\rho_i = 0.8$ is reasonable (Papaioannou et al. 2015). Alternatively, this parameter can be chose adaptively following (Papaioannou et al. 2015).

4.5 Time-dependent reliability analysis of infiltration-failure model

In this Section, the reliability analysis of the time-dependent infiltration-failure models developed in Chapter 2 is presented. As discussed in Chapter 2, the rainwater infiltration influences the surficial pore water pressure redistribution. At a given point in time, the critical slope failure plane is likely to be located at shallow depths and, hence, can be assumed parallel to the ground surface. The shallow slope failure mechanism is thus often sufficiently described by the infinite slope model (Enrico and Antonello 2012).

4.5.1 Extended Green and Ampt model

For the extended Green and Ampt model, the factor of safety (FS), associated with the

4.5 Time-dependent reliability analysis of infiltration-failure model

wetting front having reached layer j , is the minimum value among all the layers in the wetted zone (see also Fig. 2.4):

$$FS(\mathbf{X}; z_j) = \min\{FS_l(\mathbf{X}; z_j), l = 1, \dots, j\} \quad (4.18)$$

where $FS_l(\mathbf{X}; z_j)$ is the critical factor of safety for a slip surface at the bottom of layer l with the wetting front at layer j , i.e. located at depth z_j . Substituting $FS_l(\mathbf{X}; z_j)$ with Eq. (2.4), the complete expression is:

$$FS(\mathbf{X}; z_j) = \min\left\{\frac{[\gamma z_l \cos^2 \beta - p_w(z_l, z_j)] \tan \varphi' + c'}{\gamma z_l \sin \beta \cos \beta}, l = 1, \dots, j\right\} \quad (4.19)$$

in which z_l is the depth of soil layers. Eq. (4.19) computes the critical factor of safety associated with a wetting front located at layer j , neglecting failures in slip surfaces below the wetting front. These failures are included by computing the factor of safety associated with a “dry” soil ($j = 0$), which is:

$$FS(\mathbf{X}; 0) = \min\{FS_l(\mathbf{X}; 0)\} = \min\left\{\frac{\tan \varphi'}{\tan \beta} + \frac{c'}{\gamma z_l \sin \beta \cos \beta}, l = 1, 2, \dots, N_s\right\} \quad (4.20)$$

in which N_s is the total number of soil layers.

It is noted that the initial factor of safety FS_0 in this study is deterministic as the focus here is to study the uncertainty in the infiltration process and not the uncertainty of the soil strength parameters. The probability distribution of the factor of safety at each time step can be evaluated by Monte Carlo simulation, by sampling a large number of discrete sets of the random vector \mathbf{X} describing the random fields. For each realization of the random fields, the evolution of the factor of safety with time is computed by the combination of Eqs. (4.19), (4.20) and (2.18).

As discussed in Section 4.1, for the infinite slope model failure occurs when the factor of safety (FS) is less than unity. Hence, the condition $FS(\mathbf{X}; z_j) < 1$ represents instantaneous failure for a wetting front located at layer j . Usually, one is interested in knowing the probability that failure has occurred at any wetting front location smaller or

equal to j , that is, the probability that failure has occurred at any time prior to the time needed for the water to reach layer j . This probability of failure at any wetting front $k \leq j$ is termed cumulative failure probability and can be expressed as follows:

$$P_{f_j} = \Pr[F_j] = \Pr [\exists k \in \{0, \dots, j\}: FS(\mathbf{X}; z_k) < 1] \quad (4.21)$$

The failure condition of the above cumulative failure probability can be expressed by the following limit-state function:

$$g_j(\mathbf{X}) = \min\{FS(\mathbf{X}; z_k), k = 0, \dots, j\} - 1 \quad (4.22)$$

Here, $FS(\mathbf{X}; z_k)$ is the factor of safety associated with wetting front k , which is evaluated by application of Eqs. (4.20) and (4.21). Slope failure at any layer smaller or equal to j occurs for any realization \mathbf{x} of \mathbf{X} for which $g_j(\mathbf{x}) < 0$. Hence, the cumulative probability of failure P_{f_j} is given by:

$$P_{f_j} = \Pr [g_j(\mathbf{X}) < 0] \quad (4.23)$$

Following Eq. (4.21), F_j is the failure event corresponding to factor of safety FS_j being smaller than unity [see Eq. (4.19)] at any wetting front $k \leq j$. It is easy to see that F_{j-1} implies F_j , i.e. the former is a subset of the latter: $F_{j-1} \subset F_j$. Hence, for the sequence of failure events $F_0, F_1, F_2, \dots, F_n$, where n is the number of layers, it holds $F_0 \subset F_1 \subset F_2 \subset \dots \subset F_n$, see also Figure 4.3. In the following we assume that for the initial state of the infinite slope, the probability of failure is zero, $\Pr[F_0] = 0$; we can therefore omit the event F_0 in the following. Subset Simulation is applied to estimate the probability $\Pr[F_n]$. To this end, the event F_n is further decomposed into a sequence of M nested intermediate failure events $F_{n1}, F_{n2}, \dots, F_{nM}$, with $F_{n1} \supset F_{n2} \supset \dots \supset F_{nM}$. The probability $\Pr[F_n]$ is expressed as a product of the conditional probabilities:

$$P_{f_n} = \Pr[F_n] = \Pr[\bigcap_{i=1}^M F_{ni}] = \Pr[F_{n1}] \prod_{i=2}^M \Pr[F_{ni}|F_{n(i-1)}] \quad (4.24)$$

The intermediate events are defined as $F_{ni} = [g_n(\mathbf{x}) < b_{ni}]$, where $b_{n1} > b_{n2} > \dots > b_{nM} = 0$. The values of b_{ni} are chosen adaptively such that the estimates of the

4.5 Time-dependent reliability analysis of infiltration-failure model

conditional probabilities correspond to a chosen value p_0 , i.e. $p_0 = 0.1$. This is achieved by simulating samples of \mathbf{X} conditional on each intermediate failure event $F_{n(i-1)}$. For each sample, the limit-state function $g_n(\mathbf{x})$ is evaluated and the samples are ordered in increasing order of magnitude of the limit-state function values. The threshold b_{ni} is set to the p_0 -percentile of the ordered samples. The procedure is repeated until the maximum level M is reached, for which $b_{nM} = 0$. To estimate b_{n1} , unconditional samples of \mathbf{X} are obtained by crude Monte Carlo simulation. Samples of \mathbf{X} conditional on the events $F_{ni}, i = 1, \dots, M - 1$, are computed by MCMC sampling using as seeds the samples conditional on $F_{n(i-1)}$ for which $g_n(\mathbf{x}) < b_{ni}$. The probability $\Pr[F_n]$ is then obtained as:

$$\Pr[F_n] = p_0^{M-1} \hat{P}_{nM} \quad (4.25)$$

where \hat{P}_{nM} is the estimate of $\Pr[F_{nM}|F_{n(M-1)}]$ and is given by the ratio of the number of samples for which $g_n(\mathbf{x}) < 0$ over the total number of samples simulated conditional on $F_{n(M-1)}$.

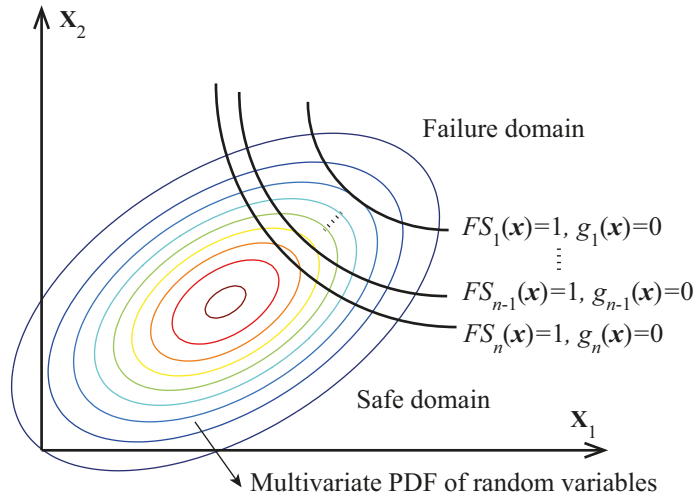


Figure 4.4 Propagation of failure domain with progression of the wetting front from step 1 to n .

At the final level of Subset Simulation for estimating F_n , the available samples conditional on $F_{nM} = F_n$ are used to start a new Subset Simulation run for estimating the conditional probability $\Pr[F_{n-1}|F_n]$. For these samples conditional on the failure domain $F_{n-1} \subset F_n$ are obtained by sampling \mathbf{X} conditional on a sequence of intermediate failure

domains through MCMC and the probability $\Pr[F_{n-1}|F_n]$ is estimated in a manner analogous to Eq. (4.16). The probability $\Pr[F_{n-1}]$ is then obtained as:

$$\Pr[F_{n-1}] = \Pr[F_n] \Pr[F_{n-1}|F_n] \quad (4.26)$$

This procedure is repeated for estimation of the remaining probabilities $\Pr[F_j], j = 1, \dots, n - 2$. An efficient algorithm for estimating the conditional probabilities $\Pr[F_{n-1}|F_n]$ is provided in (Papaioannou et al. 2015).

4.5.2 Richards equation

The factor of safety of the infinite slope along the potential slip plane at depth z'_l (see Fig. 2.2) and the certain time step t_j can be written as:

$$FS_l(\mathbf{X}; t_j) = \frac{[\gamma z'_l \cos \beta - p_w(z'_l, t_j)] \tan \varphi' + c'}{\gamma z'_l \sin \beta} \quad (4.27)$$

Note that the depth z' is measured perpendicular to the sliding surface, as opposed to the wetting front in Section 4.5.1, which is measured in vertical direction. It is assumed that the change of unit weight of soil mass during the rainwater infiltration is negligible.

Through the numerical solution of Eq. (2.28), one obtains the pressure distribution at the soil layers at a number of discrete time steps. At each time t_j , the point-in-time factor of safety is evaluated as the minimum factor of safety from all potential slip surfaces, located at the bottom of each discrete layer. The complete expression is:

$$FS(\mathbf{X}; t_j) = \min_{l=1, \dots, N_s} FS_l(\mathbf{X}, t_j) = \min \left\{ \frac{[\gamma z'_l \cos \beta - p_w(z'_l, t_j)] \tan \varphi' + c'}{\gamma z'_l \sin \beta}, l = 1, \dots, N_s \right\} \quad (4.28)$$

where z'_l is the bottom depth of soil layer l and N_s is the total number of soil layers. Here, we introduce \mathbf{X} to represent the vector of all random variables in the problem, which includes the break down coefficients for generating the random rainfall events and the saturated hydraulic conductivities at the discrete soil layers.

4.5 Time-dependent reliability analysis of infiltration-failure model

In reliability analysis, failure F is defined through limit state functions g , so that a negative value of g indicates failure, and a positive value of g represents the safe state. The limit state function defining slope failure is:

$$g_j(\mathbf{X}) = \min\{FS(\mathbf{X}; t_k), k = 1, \dots, j\} - 1 \quad (4.29)$$

in which $\min\{FS(\mathbf{X}; t_j), k = 1, \dots, j\}$ represents the minimum value of the factor of safety among all potential slip planes during the time period $t \in (0, S]$, where S is the duration of the rainfall event. The probability of failure of the infinite slope during S reads:

$$P_{f_j} = \Pr [g_j(\mathbf{X}) < 0] \quad (4.30)$$

In analogy to the previous case, in this case subsets are defined on a series of nested failure events at different time points. Having estimated the probability of failure $\Pr[F_{S_1}]$ for a rainfall scenario with duration S_1 , we can estimate the failure probability $\Pr[F_{S_2}]$ for a rainfall with the same average intensity but shorter duration $S_2 < S_1$, through starting a new subset simulation run. Because it holds that $F_{S_2} \subset F_{S_1}$, the probability of the event with shorter duration can be expressed as:

$$\Pr[F_{S_2}] = \Pr[F_{S_2}|F_{S_1}] \Pr[F_{S_1}] \quad (4.31)$$

The conditional probability $\Pr[F_{S_2}|F_{S_1}]$ can be estimated with subset simulation starting from the available samples conditional on F_{S_1} and defining a set of intermediate nested failure events, which are estimated with MCMC sampling.

Chapter 5 Bayesian updating

As presented in Chapter 2, the prediction of the factor of safety FS of the slope can be made by means of the infiltration-failure model (see also Fig. 1.2), based on the stochastic input. Often the stochastic description of uncertain input (e.g. the hydraulic conductivity K_s) for initial predictions is based on information from literature, expert knowledge and measurements at similar sites. This information is often vague and, hence, may lead to flat probability distributions, i.e. distribution with large variance. This can lead to unrealistic and often over-conservative probabilistic predictions.

To refine the probabilistic input, in-situ investigations are usually performed. Moreover, in many practical situations, additional measurements or other data may become available during an ongoing project. Data can be used to update the distribution of uncertain parameters, such as hydrogeological properties, through application of Bayesian analysis (e.g. Beck and Katafygiotis 1998). Therein the prior distribution of uncertain parameters is updated with data to the posterior distribution. The slope stability is then estimated by using the posterior distribution.

This Section presents the basic theory of Bayesian updating for learning probability distributions with measurement data. The solution of the Bayesian updating problem with a method termed BUS (Bayesian Updating with Structural reliability methods) is then discussed (Straub and Papaioannou 2014). In particular, the BUS approach is combined with Subset Simulation, which was discussed in Chapter 4. The presented approach will be applied in Chapter 6 to learn the distribution of the hydraulic conductivity with measurements of pore water pressure.

5.1 Bayesian analysis

5.1.1 Bayes' theorem

Consider a failure event F (or any other event of interest) with probability $\Pr [F]$.

5.1 Bayesian analysis

Assume that an event Z has occurred. Event Z is termed the observation event. If F represents the failure of a slope, Z could for example represent the event that the slope has survived a particular loading condition or measurements of a quantity of interest, e.g. the pore water pressure or the slope deformations. The conditional probability of the failure event F given that the observation event Z has occurred is obtained according to Bayes' theorem, as follows:

$$\Pr[F|Z] = \frac{\Pr[Z|F]\Pr[F]}{\Pr[Z]} \quad (5.1)$$

in which $\Pr[F]$ is termed the prior probability; $\Pr[F|Z]$ is the posterior probability conditional on the information; $\Pr[Z|F]$ is the likelihood describing the probability of the observation given failure; $\Pr[Z]$ is the probability of the observation.

Notice that, Bayes' theorem describes how the information Z changes the probability of the event F from $\Pr[F]$ to $\Pr[F|Z]$. Through application of Eq. (5.2) the uncertainty within the event F reduces in light of the information Z . It should be also pointed out that, the updating process can be repeated when additional information becomes available, through application of Eq. (5.2).

In many instances, instead of only describing a single event F , it is of interest to assess the distribution of a vector of continuous uncertain parameters \mathbf{X} conditional on information. Eq. (5.2) then can be expressed for continuous random variables \mathbf{X} in the following form:

$$f_{\mathbf{X}}''(\mathbf{x}) = c_E^{-1}L(\mathbf{x})f_{\mathbf{X}}'(\mathbf{x}) \quad (5.2)$$

in which $f_{\mathbf{X}}'(\mathbf{x})$ is the prior probability density function (PDF) before site specific measurements become available; $f_{\mathbf{X}}''(\mathbf{x})$ is the posterior PDF, that is, $f_{\mathbf{X}}'' = f_{\mathbf{X}|Z}$ is the conditional PDF of \mathbf{X} given the observation Z ; $L(\mathbf{x})$ is the likelihood function describing the information Z ; c_E is referred as the evidence and regarded as a normalising scalar in Eq. (5.2):

$$c_E = \int_{\mathbf{X}} L(\mathbf{x})f_{\mathbf{X}}'(\mathbf{x})d\mathbf{x} \quad (5.3)$$

Here, we use the convention $\int_{\mathbf{x}} d\mathbf{x} = \int_{-\infty}^{\infty} \cdots \int_{-\infty}^{\infty} dx_1 dx_2 \cdots dx_n$. That is, the constant c_E ensures that $f_{\mathbf{x}}''$ integrates to one and therefore is a valid PDF.

In Bayesian analysis, the major task is to estimate the posterior distribution through solving Eq. (5.2) and to update model predictions using the obtained estimate. Eq. (5.2) can be solved by a variety of existing approaches. The most common approaches are asymptotic approximation methods and sampling approaches, e.g. Markov chain Monte Carlo (MCMC) sampling or sequential Monte Carlo methods (Papaioannou et al. 2016). Here, a method termed BUS is employed to solve Eq. (5.2). In the following, the description of measurements in terms of the likelihood function is discussed. Afterwards, estimation of the posterior distribution using the BUS approach is presented.

5.1.2 Likelihood function

The likelihood function is defined as being proportional to the probability of the observation Z given a parameter state \mathbf{x} , i.e.

$$L(\mathbf{x}) \propto \Pr[Z|\mathbf{X} = \mathbf{x}] \quad (5.4)$$

For example, the likelihood of the information that the slope has survived a loading condition (e.g. an intense rainfall event) can be expressed as the indicator function of an observation domain, i.e.

$$L(\mathbf{x}) = I(h(\mathbf{x}) \leq 0) \quad (5.5)$$

where the domain $\{h(\mathbf{x}) \leq 0\}$ contains all outcomes for which the slope survives the particular loading.

Assume now that the measurement y_i is of a continuous quantity, which is related to the uncertain input parameters through a model $\eta_i(\mathbf{x})$. Typically, the measurement is associated with an error term ϵ_i , which is attributed to measurement and/or model errors. If the error is additive, the event describing this measurement is given by

5.2 BUS approach

$$Z = \{y_i = \eta_i(\mathbf{x}) + \epsilon_i\} \quad (5.6)$$

In this case, the likelihood function of this observation $L_i(\mathbf{x})$ is given as follows:

$$L_i(\mathbf{x}) = f_{\epsilon_i}(y_i - \eta_i(\mathbf{x})) \quad (5.7)$$

in which $f_{\epsilon_i}(y_i - \eta_i(\mathbf{x}))$ is the PDF of the error ϵ_i . If a total of m independent measurements are available, then the joint likelihood function $L(\mathbf{x})$ describing all measurement is evaluated as follows:

$$L(\mathbf{x}) = \prod_{i=1}^m L_i(\mathbf{x}) \quad (5.8)$$

Assume the likelihood function for each measurement follows the normal distribution with a zero mean (e.g. Betz et al. 2014), i.e. $L_i(\mathbf{x}) \sim N(0, \sigma_{\epsilon_i}^2)$, in which σ_{ϵ_i} is the standard deviation of the error. In this case, the likelihood function of Eq. (5.8) takes the following form

$$L(\mathbf{x}) = \exp\left\{-\sum_{i=1}^m \frac{[y_i - \eta_i(\mathbf{x})]^2}{2\sigma_{\epsilon_i}^2}\right\} \quad (5.9)$$

wherein the proportionality constant is omitted. For computational purposes, it is often convenient to evaluate the logarithm of the likelihood function. It reads:

$$\ln L(\mathbf{x}) = -\sum_{i=1}^m \frac{[y_i - \eta_i(\mathbf{x})]^2}{2\sigma_{\epsilon_i}^2} \quad (5.10)$$

5.2 BUS approach

5.2.1 Basic idea

The basic idea of the BUS (Bayesian Updating with Structural reliability methods) approach is to define an equivalent reliability problem and solve the Bayesian updating problem by applying structural reliability methods. To this end, the observation domain Ω_Z is established as:

$$\Omega_Z = \{\pi \leq c \cdot L(\mathbf{x})\} \quad (5.11)$$

in which π is a uniformly distributed random variable in $[0,1]$; c is a positive constant chosen such that $c \cdot L(\mathbf{x}) \leq 1$ is satisfied for all \mathbf{x} . It can be shown (e.g. Betz et al. 2016) that the posterior distribution can be obtained by censoring the prior distribution of the vector $[\mathbf{X}; \pi]$ at the observation domain and integrating over π , i.e.

$$f_{\mathbf{X}}''(\mathbf{x}) \propto \int_0^1 I_{\Omega_Z}(\mathbf{x}, \pi) f_{\mathbf{X}}'(\mathbf{x}) d\pi \quad (5.12)$$

in which $I_{\Omega_Z}(\mathbf{x})$ is the indicator function of the observation domain Ω_Z . Therefore, the solution of the updating problem becomes equivalent to solving a structural reliability problem in the extended random variable space $[\mathbf{X}; \pi]$. The observation domain is then described by an equivalent limit state function $h(\mathbf{x}; \pi)$ as:

$$h(\mathbf{x}; \pi) = \pi - cL(\mathbf{x}) \quad (5.13)$$

The observation domain is then defined as $\Omega_Z = \{h(\mathbf{x}, \pi) \leq 0\}$. The observation event is then $Z = \{\mathbf{x} \in \Omega_Z\}$.

To apply the likelihood function in natural logarithm scale, based on Eqs. (5.11) and (5.13) one could employ the following equivalent formulation of the limit state function:

$$\hat{h}(\mathbf{x}; \pi) = \ln(\pi) - \ln(c) - \ln[L(\mathbf{x})] \quad (5.14)$$

in which $\ln(\cdot)$ denotes the natural logarithm operator.

By applying transformation to an equivalent standard normal random variable space $\mathbf{U} = [u_0; u_1; \dots; u_n]$, Eq. (5.14) can be written as:

$$\hat{H}(\mathbf{u}) = \ln \Phi(u_0) - \ln c - \ln\{L[\Phi(u_1, u_2, \dots, u_n)]\} \quad (5.15)$$

in which $\mathbf{T}(\cdot)$ is a classical transformation operator used in structural reliability methods (see Section 4.2); $\Phi(\cdot)$ is the CDF of the standard normal distribution.

5.2 BUS approach

A crucial issue on the implementation of the BUS approach is the choice of the constant c . As noted earlier c needs to satisfy $cL(\mathbf{x}) \leq 1$. Therefore, c should be chosen smaller than the reciprocal of the maximum value of the likelihood function, denoted $\max[L(\mathbf{x})]$. If c is chosen too small then the probability of the observation event $\Pr(Z)$ will become too small and therefore the BUS approach will be inefficient. Therefore the optimal choice of c is:

$$c = \frac{1}{\max[L(\mathbf{x})]} \quad (5.16)$$

The simplest approach to solve the BUS problem is by application of the standard Monte Carlo method. In this case, the standard normal distribution is sampled and the samples that lie in the observation domain will be samples from the posterior distribution. These samples could be further used to obtain updated predictions. In many cases, the probability that a sample lies in the observation domain $\Pr(Z)$ will be small. In such cases, the Monte Carlo method will be inefficient. Therefore, the BUS approach is combined with the Subset Simulation, which is efficient in estimating probabilities of rare events in high dimensional input spaces.

5.2.2 Subset Simulation-based BUS approach

The probability $\Pr(Z)$ can be solved by application of the Subset Simulation algorithm. As discussed in Section 4.3, Subset Simulation is an adaptive Monte Carlo method and it can efficiently handle rare events in cases with high dimensions. Following the strategy discussed in Chapter 4, the observation event can be expressed as the intersection of M intermediate events Z_i , i.e. $Z_0 \subset Z_1 \subset \dots \subset Z_M = \Omega_Z$, in which Z_0 represents the certain event. The domains Z_i are defined as the sets $\{\widehat{H}(\mathbf{u}) \leq b_i\}$, where b_i are threshold levels, namely $b_0 = \infty > b_1 > \dots > b_M = 0$. According to Eq. (5.14), the intermediate domains can be expressed as:

$$F_i = \{\pi \leq c \cdot L(\mathbf{x}) \cdot \exp(b_i)\}, i = 1, 2, \dots, M \quad (5.17)$$

Hence, the probability of failure is equivalent to a series of product of conditional

probabilities, i.e.

$$p_{\Omega_Z} = \Pr[F_0] \prod_{i=1}^M \Pr[F_i|F_{i-1}] \quad (5.18)$$

For details on the implementation of the standard Subset Simulation algorithm the reader can refer to Chapter 4.

5.2.3 Adaptive Subset Simulation-based BUS approach

The efficiency of the Subset Simulation method depends linearly on $\ln[\Pr(Z)]$. As discussed in Section 5.2.2, the magnitude of the probability of the observation $\Pr(Z)$ depends on the choice of the constant c . In particular, the optimal value of c is given by the reciprocal of the maximum of the likelihood function, as in Eq. (5.16). Therefore, one can enhance the efficiency of the SuS-based BUS approach by choosing c adaptively, as the reciprocal of the maximum of the samples of the likelihood function evaluated at each subset level. This is underlying idea behind the adaptive BUS-SuS (BUS with Subset Simulation) approach.

The formulation of the limit state function of Eq. (5.16) facilitates the implementation of the adaptive BUS-SuS approach, because it can ensure the nestedness of the intermediate failure domains (Betz et al. 2016). Assume that at subset level i , samples $\{\mathbf{x}_k, k = 1, \dots, n_s\}$ samples are available. The constant c at subset level i is computed as

$$c_i = \frac{1}{\max[c_{i-1}^{-1}, \{L(\mathbf{x}_k), k=1, \dots, n_s\}]} \quad (5.19)$$

where c_{i-1} is the constant evaluated at subset level $i - 1$. In order to ensure that the intermediate failure events defined by Eq. (5.17) are nested, the threshold level of the subset level i should be adjusted through:

$$b_i = b_i + \ln\left(\frac{c_i^{-1}}{c_{i-1}^{-1}}\right) \quad (5.20)$$

Apart from these two steps, the subset simulation algorithm remains the same as

5.2 BUS approach

in Chapter 4.

5.2.4 Limitation of the Subset Simulation-based BUS approach

As an inverse analysis method, Subset Simulation-based BUS approach works well for many linear or nonlinear models (Straub and Papaioannou 2014). The Subset Simulation algorithm embedded in the BUS approach facilitates the process of searching for target samples, because of its efficiency for dealing with rare events in cases with high dimensions. Furthermore, choosing the constant c adaptively also reduces the runtime of program. Nevertheless, in some situations the MCMC algorithm for sampling the intermediate domains is not able to propagate throughout the probability space and gets trapped in some small areas or islands. Such cases typically occur when the model is not a one-to-one function, which renders the input not uniquely identifiable based on measurements of the output. In such cases, the likelihood function has multiple modes, which translate to multiple islands in the equivalent observation domain of the BUS approach. Therefore, when performing local moves in the MCMC algorithm, the probability of leaving an island in the vicinity of a local mode of the likelihood becomes extremely small. This leads to most of the resulting samples being concentrated in the vicinity of a local mode. Therefore, the resulting posterior estimate is not able to identify all the possible states of the posterior distribution and therefore underestimates its actual variability.

Figure 5.1 illustrates the results from a Bayesian analysis according to the two modeling functions $\eta_1(\mathbf{z}) = \sin[K_s(\mathbf{z})]$ and $\eta_2(\mathbf{z}) = \sin[10K_s(\mathbf{z})]$, respectively. Here, K_s is a lognormal random field. The median of K_s is 3.6cm/hr and the standard deviation in decimal logarithm scale is 0.2, i.e. $\sigma_{\log_{10}K_s} = 0.2$. The scale of fluctuation is chosen as 5m. The soil column with 5m depth is then discretized into 100 equal thickness layers and the resulting random vector is approximated with the discrete KL expansion with 10 largest terms. In this case, 10 observations are selected at uniformly distributed points along the depth of the soil column. The synthetic observations of the models are obtained through generating a random realization of the random field and adding a Gaussian noise with standard deviation 0.1 to the corresponding model outcome. The likelihood function

is then defined according to Eq. (5.9). The model η_1 has a large period and for the considered range of K_s the resulting mapping is one-to-one. The period of model η_2 is considerably smaller, which leads to a mapping that is not one-to-one.

Figure 5.1(a) shows the comparison between the posterior mean of $\log_{10}K_s$ and the true value of $\log_{10}K_s$ (i.e. the realization of $\log_{10}K_s$ used to generate the measurements), together with 95% credible interval for model η_1 . As seen from this figure, the true value is within the credible interval obtained with the posterior samples, which manifests to the efficiency of the BUS approach in identifying $\log_{10}K_s$. Figure 5.1(b) illustrates the posterior distribution and true value for model η_2 , i.e. the model with smaller period. In this case, the 95% credible bounds shrink, which indicates reduction of the variability of the posterior samples. Also, it can be seen that the true value is not correctly identified. This is because model η_2 will result in multiple modes of the likelihood function. Hence, the MCMC samples in the Subset Simulation-based BUS approach get trapped around a local maximum of the likelihood function.

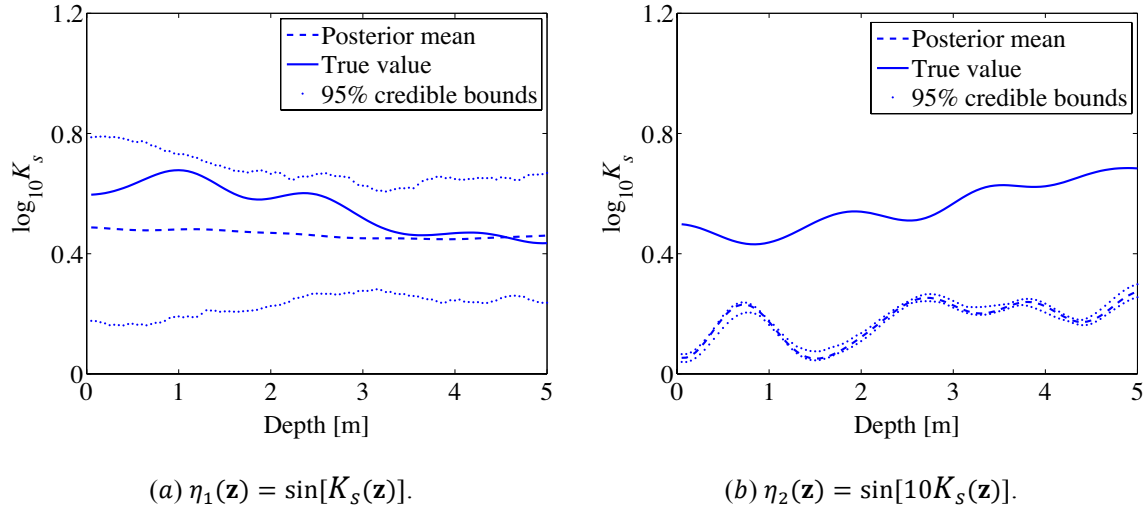


Figure 5.1 Two applications of the adaptive BUS-SuS approach.

To illustrate better this problem, we look at plots of the likelihood function. Figure 5.2 shows contour plots of the logarithm of the likelihood function in terms of the first two random variables in the KL representation of the random field for the two modeling functions, i.e. $\eta_1(\mathbf{z}) = \sin[K_s(\mathbf{z})]$ and $\eta_2(\mathbf{z}) = \sin[10K_s(\mathbf{z})]$. The remaining

5.2 BUS approach

random variables in the KL representation are fixed at their mean values. As shown in Figure 5.2(a), the likelihood varies smoothly around a single mode for model η_1 within the given range $[-2,2] \times [-2,2]$ in standard normal space. On the other hand Figure 5.2(b) shows that the likelihood of model η_2 has multiple maxima. Therefore, for this model MCMC samples are not able to reach the target domain by crossing between regions around the local maximum values.

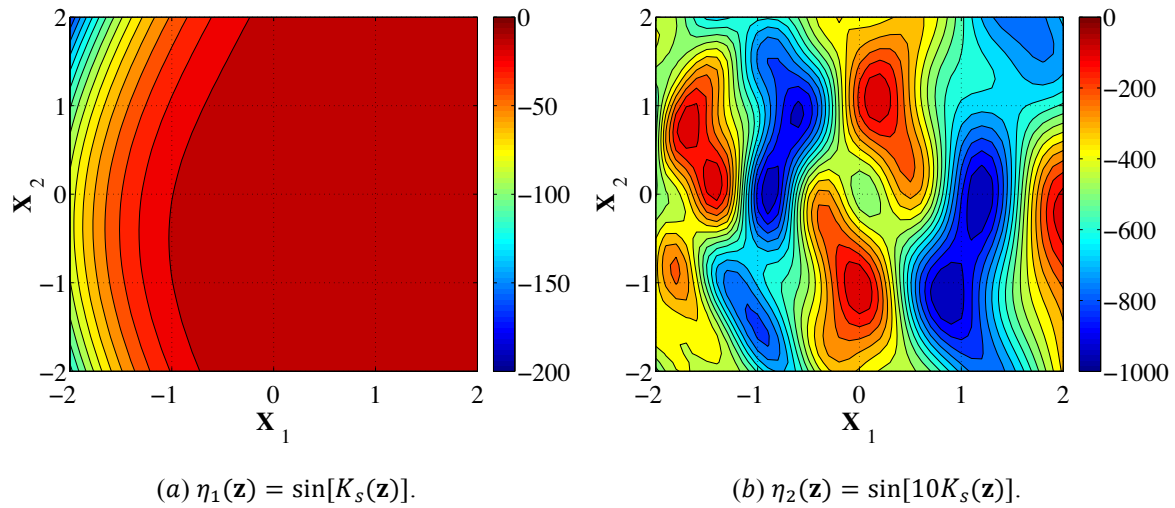


Figure 5.2 Contour plots of the logarithm of the likelihood function.

Chapter 6 Numerical investigations

6.1 Case description

We consider an infinite slope in a sandy subsoil subjected to rainfall events. The sandy layer has 5m depth above a highly permeable layer, represented by a free drainage boundary condition. In this study, we are only interested in potential slip surfaces above the lower boundary. The slope angle and effective friction angle are $\beta = 18^\circ$ and $\varphi' = 30^\circ$, respectively. The effective cohesion of the sand is assumed to be zero, i.e. $c' = 0\text{kPa}$ and the unit weight is 20kN/m^3 . The saturated unit weight is selected for the conservative estimation of the slope stability.

6.2 Application of extended Green and Ampt model to time-dependent reliability analysis

In this section, the reliability analysis of the infinite slope is performed based on the extended Green and Ampt model. The direct effects of matric suction on the effective stress, and as such the stability of the slope, are neglected. The layers of the infinite sandy slope are assumed to have the same water content $\theta_0 = 0.125$ prior to the rainwater infiltration. That is, the residual effect of antecedent rainfall events is neglected. The saturated vertical hydraulic conductivity K_s and suction head S are modeled as statistically homogeneous lognormal random fields with medians $M_{K_s} = 2.99\text{ cm/hr}$ and $M_{|S|} = 6.13\text{ cm}$, respectively. These values are for loamy sands (Rawls et al. 1983). We assume that the point-wise cross-correlation coefficient between K_s and $|S|$ is $\rho_c = -0.5$. In a parametric study, the standard deviation and the scale of fluctuation of the decimal logarithms of the two random fields are varied. The random fields are discretized with the midpoint method using 100 layers, i.e. thickness $\Delta z = 0.05\text{m}$ [see also Fig. 2.2 (a)]. The deterministic parameters of the Green and Ampt model for loamy sand are taken from Rawls et al. (1982) and Rawls et al. (1983) as given in Tab. 6.1.

6.2 Application of extended Green and Ampt model to time-dependent reliability analysis

Table 6.1 Parameters for Green and Ampt model.

Parameters	Unit	Definition	Value
K_s	cm/hr	Saturated hydraulic conductivity	$M_{K_s} = 2.99$
S	cm	Suction head	$M_{ S } = 6.13$
$\sigma_{\log_{10} K_s}$	$\log_{10}(\text{cm/hr})$	Standard deviation of K_s in decimal logarithm scale	[0.1, 0.2, 0.3, 0.4, 0.5]
$\sigma_{\log_{10} S }$	$\log_{10}(\text{cm})$	Standard deviation of S in decimal logarithm scale	[0.1, 0.2, 0.3, 0.4, 0.5]
θ_s	-	Saturated water content	0.437
θ_0	-	Initial water content	0.125

We use the symbol $\sigma_{\log_{10}(K_s,|S|)}$ to indicate that $\sigma_{\log_{10} K_s}$ and $\sigma_{\log_{10} |S|}$ take the same value.

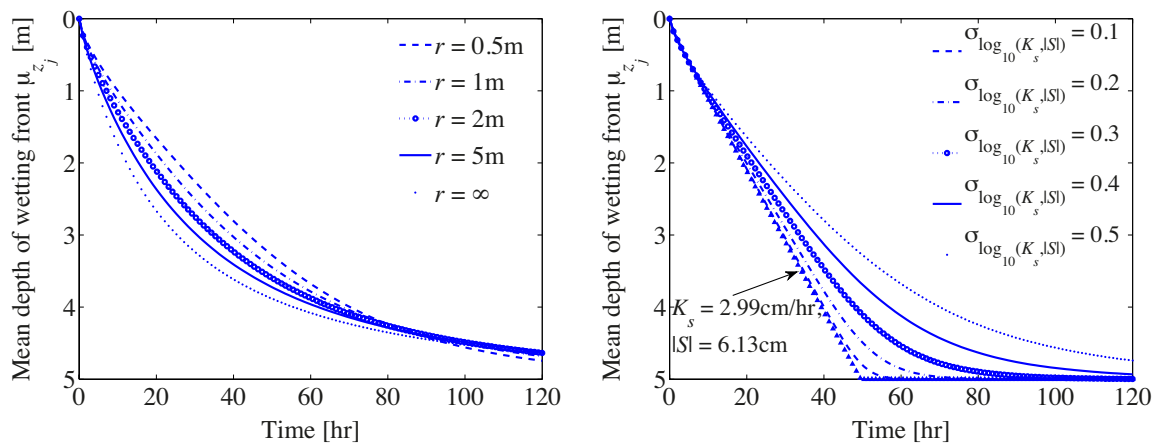
6.2.1 Wetting front development

First, the influence of the scale of fluctuation and standard deviation of the two random fields on the wetting front development is investigated. Figure 6.1 presents the development of the mean depth of the wetting front with time evaluated using 5000 samples (realizations) of the random fields. The time period of interest is 120 hours (5 days) after the start of the rainfall event.

Figure 6.1 (a) shows the wetting front development for different values of the scale of fluctuation of the two random fields. The standard deviation of the decimal logarithms for both fields $\sigma_{\log_{10}(K_s,|S|)}$ is here 0.5. It is shown that in the case of a smaller scale of fluctuation, the water infiltrates slower towards the bottom of the soil column. This can be explained by the fact that a small scale of fluctuation implies a larger variability within the wetted zone and hence more frequent occurrence of lower values of K_s . The flow within the wetted zone as the wetting front becomes deeper becomes dominated by the low values of K_s , as the evident from the use of the harmonic mean of the saturated hydraulic conductivity in Eq. (2.17). For a rainfall period of more than 80 hours, the infiltration rates of the larger scale of fluctuation cases ($r \geq 0.5\text{m}$) are nearly identical. It can be inferred that, as the wetting front advances, the difference of the effective hydraulic conductivity K_{eff} within wetted zone in those cases become smaller. In the limit case $r = \infty$, the hydraulic conductivity is constant in space and hence

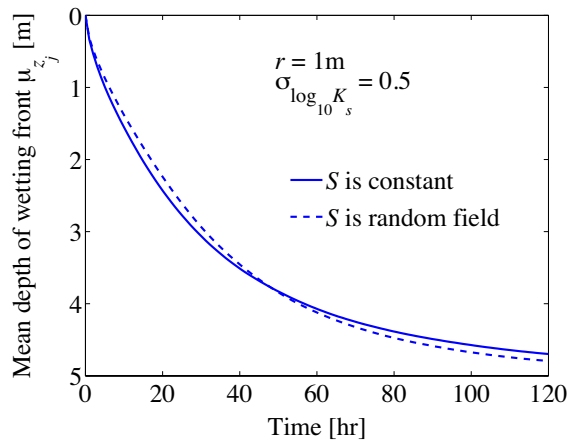
modeled by a single random variable.

Figure 6.1(b) shows the influence of a variation in the standard deviation $\sigma_{\log_{10}(K_s|S)}$ of the two random fields. Here, the scale of fluctuation is fixed at 0.5m. As $\sigma_{\log_{10}(K_s|S)}$ increases, the wetting front moves slower towards the bottom of the soil column. This is due to the fact that a large standard deviation increases the average occurrence of low values of the saturated hydraulic conductivity and hence decreases its harmonic mean within the wetted zone.



(a) Influence of the scale of fluctuation r for a constant $\sigma_{\log_{10}(K_s|S)} = 0.5$.

(b) Influence of the standard deviation $\sigma_{\log_{10}(K_s|S)}$ for a constant $r = 0.5\text{m}$.



(c) Influence of the suction head S for $r = 1\text{m}$ and $\sigma_{\log_{10}(K_s|S)} = 0.5$.

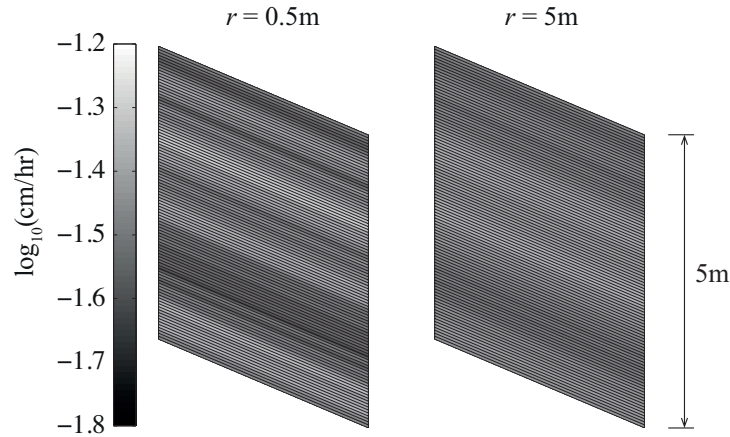
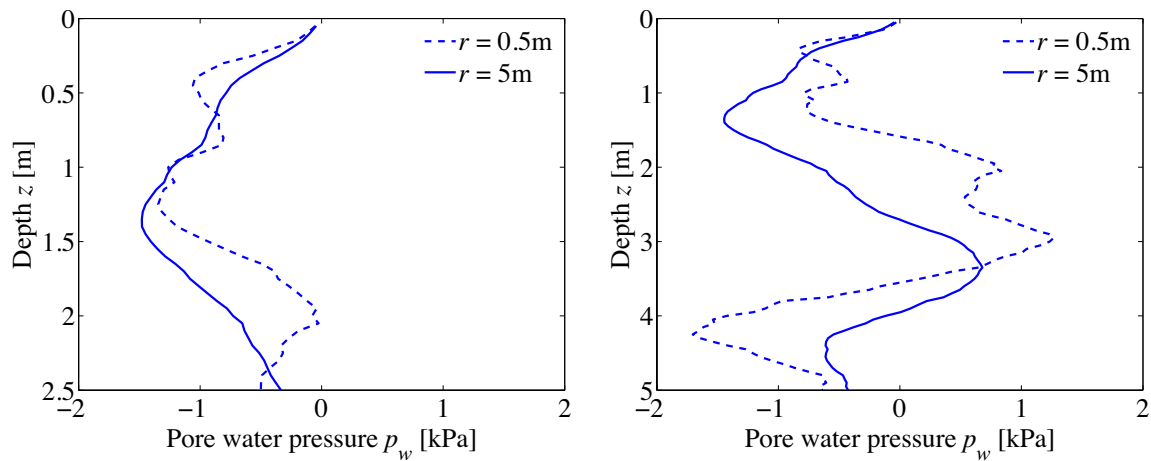
Figure 6.1 The mean wetting front development.

6.2 Application of extended Green and Ampt model to time-dependent reliability analysis

Figure 6.1(c) shows the influence of the suction head on the mean wetting front development. There is only small difference between the wetting front development for the case where the suction head is fixed at its median value and the case where it is modelled as a random field when $r = 1\text{m}$ and $\sigma_{\log_{10}K_s} = 0.5$. It is noted that for each realization at each time step, only the suction head at the wetting front is used to evaluate the hydraulic gradient [see Eq. (2.15)].

6.2.2 Pore water pressure buildup

Throughout the infiltration process, the variable permeability within the sandy soil will influence the pore water pressure buildup and further influence the factor of safety of the infinite slope. Figure 6.2 shows the pore water pressure distribution for the two realizations of the hydraulic conductivity, corresponding to scales of fluctuation of 0.5m and 5m, respectively, for two specific depths of the wetting front, i.e. 2.5m and 5m. The suction head is kept constant and equal to its median 6.13 cm, as the influence of its variability on the wetting front development was shown to be small [cf. Fig. 6.1(c)]. In the case with smaller scale of fluctuation ($r = 0.5\text{m}$), the spatial variability of the hydraulic conductivity within the wetted zone introduces fast local changes in hydraulic head [cf. Eq. (2.22)], which lead to fast changes in the pore water pressure. This can be clearly observed in Figure 6.2, where for a small scale of fluctuation ($r = 0.5\text{m}$) the pore water pressure presents larger spatial variation along the depth of the soil column, whereas for a larger scale of fluctuation ($r = 5\text{m}$), the distribution of pore water pressure represented by the dashed line is smoother. The pore water pressure build-up at the areas with steep gradient of the hydraulic conductivity is evident when comparing Figures 6.2(a), (b) and (c). Moreover, the large hydraulic gradients in the highly fluctuating case introduce positive pore water pressure at shallow depths of the wetting front [see Figure 6.2(c)]. Based on Eq. (2.4), the factor of safety decreases as the pore water pressure increases and as the depth of the potential slip surface decreases. Hence, positive pore water pressure at a shallow depth of the wetting front will undermine the stability of the slope and favor shallow slope failure.

(a) Realizations of $\log_{10}K_s$ for different scale of fluctuation.(b) Depth of wetting front $z_j = 2.5\text{m}$.(c) Depth of wetting front $z_j = 5\text{m}$.**Figure 6.2** Pore water pressure distributions for the realizations of the hydraulic conductivity.

6.2.3 Mean factor of safety

The mean factor of safety is obtained by generating 5000 Monte Carlo realizations of the random fields representing the hydraulic conductivity and suction head, taking the mean value of the factors of safety computed for individual realizations, according to Eq. (4.19). $\sigma_{\log_{10}(K_s|S)}$ and r are varied to assess their influences on the mean factor of safety.

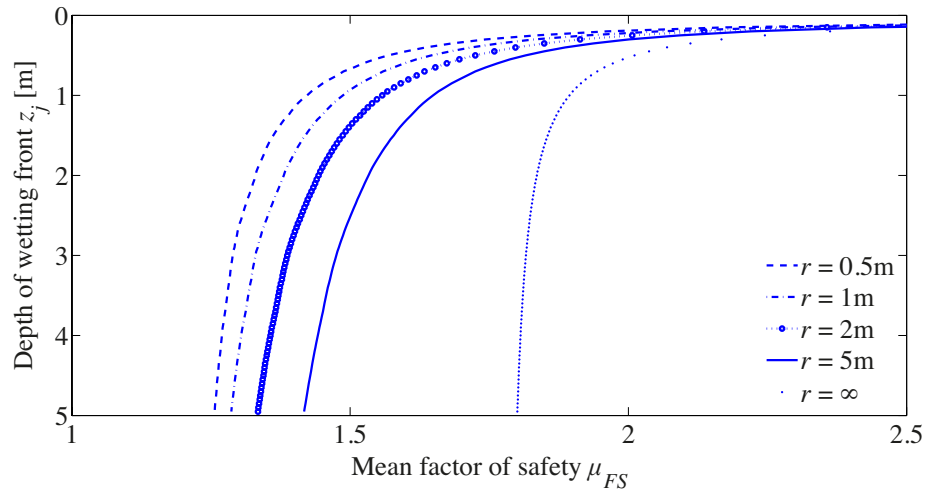
Figure 6.3(a) shows the influence of the scale of fluctuation on the mean factor of safety with respect to the wetting front development, for $\sigma_{\log_{10}(K_s|S)}$ fixed at 0.5.

6.2 Application of extended Green and Ampt model to time-dependent reliability analysis

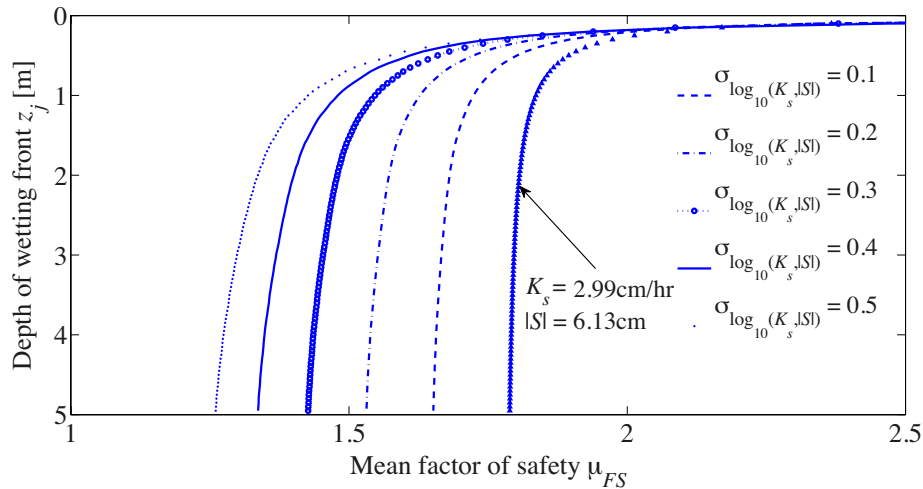
Since the pore water pressure tends to increase as the wetting front progresses, the mean factor of safety decreases during the infiltration procedure in all cases. The transient behavior of the mean factor of safety is characterized by a fast reduction right after the beginning of the rainfall event, followed by a slower decrease as the wetting front moves closer towards the bottom of the soil column [cf. Figure 6.1(a)]. The reduction is larger in the case where the scale of fluctuation is smaller and hence the spatial variability of the permeability parameters is higher. This is because high spatial variability of the hydraulic conductivity within the wetted zone introduces large hydraulic gradients, as also illustrated in Figure 6.2, and therefore increases the likelihood of high pore water pressure at shallow depths of the wetting front, which are critical for the stability of the slope. Hence the factor of safety reaches its minimum on average at a smaller depth of the wetting front in highly fluctuating soils as compared to more homogeneous soils. Moreover, due to the low pore water pressure gradients the minimum factor of safety in soils with larger scale of fluctuation is larger than the one in highly fluctuating soils.

Figure 6.3(b) depicts the influence of $\sigma_{\log_{10}(K_s,|S|)}$ on the mean factor of safety of the slope. The scale of fluctuation is fixed at $r = 0.5\text{m}$. The resulting mean factor of safety has a similar transient behavior in all cases, i.e. its value decreases in the first 1m and asymptotically approaches a minimum value. This minimum value decreases with increase of $\sigma_{\log_{10}(K_s,|S|)}$, which is due to the standard deviation increasing and the high positive pore water pressures at shallower depths become more likely.

Next we investigate the change of the location of the critical slip surface within the wetted zone with respect to the development of the wetting front. The factor of safety of each potential slip plane within the dry zone remains constant during the rainwater infiltration and equals $\tan\phi'/\tan\beta$, because positive pore water pressure only exists in the wetted zone and pore water pressure is negative in the dry zone due to suction, see Eq. (4.20). Here, the critical slip surface corresponds to the plane with minimum factor of safety in the wetted zone of the soil column.



(a) Influence of the scale of fluctuation r for a constant $\sigma_{\log_{10}(K_s, |S|)} = 0.5$.



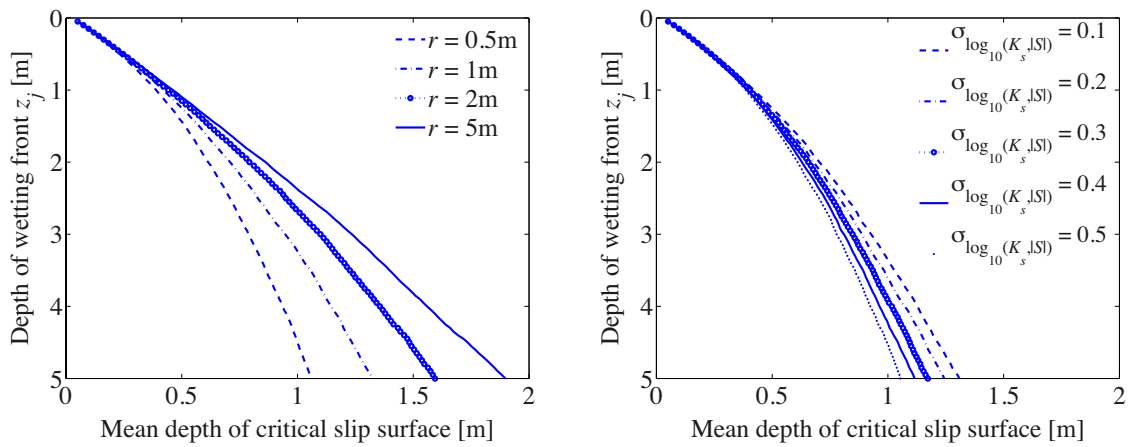
(b) Influence of the standard deviation $\sigma_{\log_{10}(K_s, |S|)}$ for a constant $r = 0.5\text{m}$.

Figure 6.3 Mean factor of safety in terms of wetting front development.

Figure 6.4(a) shows the influence of the scale of fluctuation on the mean depth of the critical slip surface within the wetted zone with wetting front development for $\sigma_{\log_{10}(K_s, |S|)} = 0.5$. It is shown that the mean depth of the critical slip surface approaches the ground surface as the scale of fluctuation decreases. Hence small scales of fluctuation r favor shallow slope failure. This agrees with Figure 6.4(a), where it was shown that for small r the factor of safety on average reduces faster to its minimum value with the wetting front development. Conversely, for larger scales of fluctuation the critical slip surface increases linearly with the wetting front development and therefore the mean

6.2 Application of extended Green and Ampt model to time-dependent reliability analysis

factor of safety decreases slower. In Figure 6.4(b), we fix the scale of fluctuation at $r = 0.5\text{m}$ and study the influence of the standard deviation $\sigma_{\log_{10}(K_s|S)}$ on the mean depth of critical slip surface. For higher values of $\sigma_{\log_{10}(K_s|S)}$, the critical slip surface moves closer to the ground surface. However, the influence of $\sigma_{\log_{10}(K_s|S)}$ is less pronounced than the influence of the scale of fluctuation. This agrees with the result of Figure 6.3(b), which shows that changes in $\sigma_{\log_{10}(K_s|S)}$ will not significantly influence the transient behavior of the mean factor of safety. It only affects the minimum value of the mean factor of safety.



(a) Influence of the scale of fluctuation r for a constant $\sigma_{\log_{10}(K_s|S)} = 0.5$.

(b) Influence of the standard deviation $\sigma_{\log_{10}(K_s|S)}$ for a constant $r = 0.5\text{m}$.

Figure 6.4 Critical slip surface distributions within wetted zone.

6.2.4 Probability of failure

In most cases, the probability of failure of the infinite slope due to infiltration is small. We therefore employ Subset Simulation for computing it (see Section 4.1.4). 1000 samples are used at each subset and the intermediate conditional probability is taken as $p_0 = 0.1$.

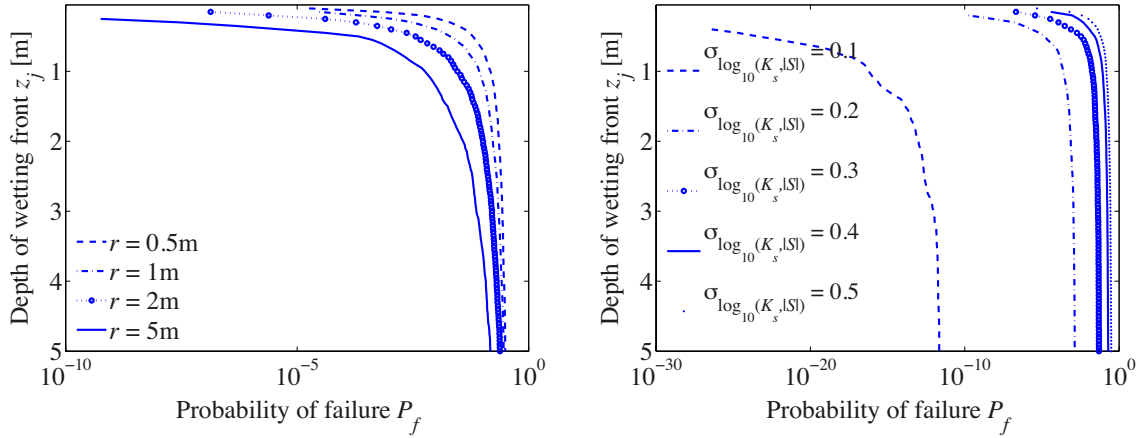
Figure 6.5(a) shows the influence of the scale of fluctuation on the probability of failure in function of the wetting front development, for a fixed $\sigma_{\log_{10}(K_s|S)} = 0.5$. As the wetting front depth increases, the probability of failure approaches the same value for all scales for fluctuation. However, this value is reached much faster for smaller scales of

fluctuation, i.e. for larger variability of the permeability within the soil layer. This agrees with Figure 6.3(a) where it is shown that in cases with smaller scales of fluctuation the mean factor of safety decreases faster at shallower depths of the wetting front. It can be concluded that in soils with high spatial variability the probability of failure of the infinite slope is higher at the start of the rainfall event compared to soils with low variability.

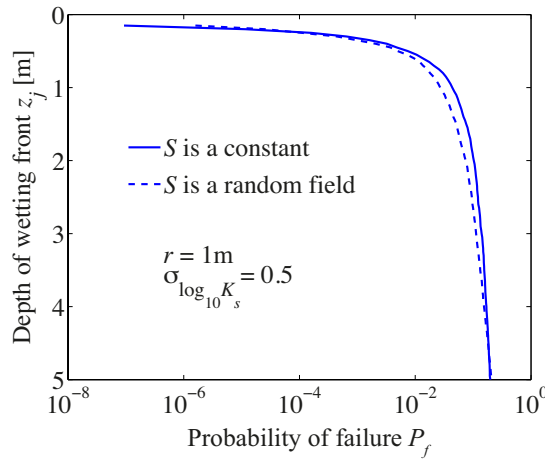
Figure 6.5(b) illustrates the influence of $\sigma_{\log_{10}(K_s,|S|)}$ on the probability of failure of the infinite slope for a fixed (small) scale of fluctuation $r = 0.05\text{m}$. We see that in all cases the probability of failure increases fast to a constant value within 0~1m wetted depth. This is because the scale of fluctuation is small and hence failure is more likely to occur at shallow depths. Also, as illustrated in Figure 6.4(b), the standard deviation in log scale does not have significant influence on the mean position of the critical slip surface within the wetted zone. The logarithm of the probability of failure in the case with different $\sigma_{\log_{10}(K_s,|S|)}$ converges to different values as the wetting front advances. These values increase exponentially with increase of $\sigma_{\log_{10}(K_s,|S|)}$, which indicates that $\sigma_{\log_{10}(K_s,|S|)}$ has significant influence on the reliability of the infinite slope. Moreover, it is shown that as the standard deviation increases the probability of failure increases faster with the wetting front development. This is because, although $\sigma_{\log_{10}(K_s,|S|)}$ does not influence the mean depth of the critical slip surface, it has an impact on the variance.

Figure 6.5(c) illustrates how the suction head affects the probability of failure when it is taken as constant or modelled as a random field. In this case, $r = 1\text{m}$ and $\sigma_{\log_{10}K_s} = 0.5$. The probabilities of failure for the two cases are close to each other both in the beginning and in the end of the infiltration process. A small difference between the two curves can be observed in the interval from $z = 1$ to 4m. However, comparing this difference with the one between the curves in Figures 6.5(a) and (b), we see that the influence of the variability of the suction head is small compared to the one of the saturated hydraulic conductivity.

6.3 Application of Richards equation to time-dependent reliability analysis



(a) Influence of the scale of fluctuation r for a constant $\sigma_{\log_{10}(K_s, |S|)} = 0.5$. (b) Influence of the standard deviation $\sigma_{\log_{10}(K_s, |S|)}$ for a constant $r = 0.5$ m.



(c) Influence of the suction head S for a constant $r = 1$ m and $\sigma_{\log_{10} K_s} = 0.5$.

Figure 6.5 Probability of failure in terms of wetting front development.

6.3 Application of Richards equation to time-dependent reliability analysis

In this section, we assess the reliability of the infinite slope in sandy soil subjected to random rainfall events with the infiltration model based on Richards equation. The layers of the infinite sandy slope are assumed to have the same water content $\theta_0 = 0.2$ before the rainwater infiltration. The median of the saturated hydraulic conductivity K_s is 3.6cm/hr. The standard deviation in log-scale, i.e. the standard deviation of $\log_{10} K_s$, is

0.3. The random field representing the hydraulic conductivity is discretized with the midpoint method using 100 equal thickness layers. The remaining permeability parameters of the sandy soil are modeled deterministically, and their values are summarized in Tab. 6.2.

Table 6.2 Permeability parameters.

Parameters	α	n	θ_s	θ_r
Values	0.145	2.68	0.437	0.02
Sources	Zlotnik et al. 2007		Rawls et al. 1982	

The random process modeling the stochastic behavior of the rainfall event and the continuous random field modeling the spatial variability of the hydraulic conductivity of the soil are represented by a set of correlated random variables, as discussed in Section 3.3. The number of random variables required for representing the rainfall event is $2^{N+1} - 2$, where N is the number of downscaling steps. The number of random variables for representing the hydraulic conductivity is the same as the number N_s of discrete soil layers. The total number of random variables for different duration of the rainfall event with a fixed $N_s = 100$ are listed in Tab. 6.3:

Table 6.3 Durations of rainfall events and random variables.

Parameters	Values				
Duration [hr]	3.2	6.4	12.8	25.6	51.2
N	5	6	7	8	9
Total random variables	162	226	354	610	1122

6.3.1 Pore water pressure redistribution

With the onset of a rainfall event, the pore water pressure within the soil slope changes with time and depth. Here, we look at the influence of the scale of fluctuation of the random field, which describes the saturated hydraulic conductivity of the soil, on the pore

6.3 Application of Richards equation to time-dependent reliability analysis

water pressure buildup. We consider two realizations of the hydraulic conductivity corresponding to two different scales of fluctuation, namely 0.5m and 4m. A random rainfall pattern is generated with parameters $a_0 = 12.27$ and $H = 0.47$, which are obtained by regression analysis based on rainfall data in the Melbourne area (Menabde and Murugesu 2000), and duration 25.6hr. The average rainfall intensity is 3cm/hr. Figure 6.6 shows the realization of the random rainfall event. Figure 6.7(a) – (d) illustrates the saturated hydraulic conductivity distribution in decimal logarithm scale on the left side and redistribution of the pore water pressure along the z direction on the right side for the different chosen parameter values. It is shown that the saturated hydraulic conductivity varies more frequently in the case of a smaller scale of fluctuation. The difference of the pore water pressure redistribution caused by $\sigma_{\log_{10} K_s}$ is significant [cf. Figure 6.7(a) and (c) or Figure 6.7 (b) and (d)].

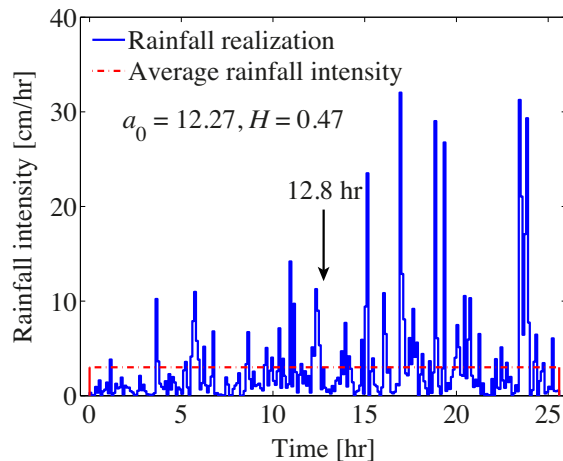


Figure 6.6 One realization of random event with duration 25.6hr.

In addition, the wetting front moves faster in the case with smaller $\sigma_{\log_{10} K_s}$. It can also be observed that occurrence of positive pore water pressure at shallow depths is favored in cases with smaller scale of fluctuation and larger $\sigma_{\log_{10} K_s}$. Looking at the figures for $\sigma_{\log_{10} K_s} = 0.5$ [cf. Figure 6.7 (c) and (d)], one can observe that a larger scale of fluctuation results in a clearer defined wetting front development from 12.8hr to 25.6hr, while for a smaller scale of fluctuation the wetting front is less clearly identified. Notice that, in all cases there is nearly no change in pore water pressure below the

wetting front between 12.8hr and 25.6hr.

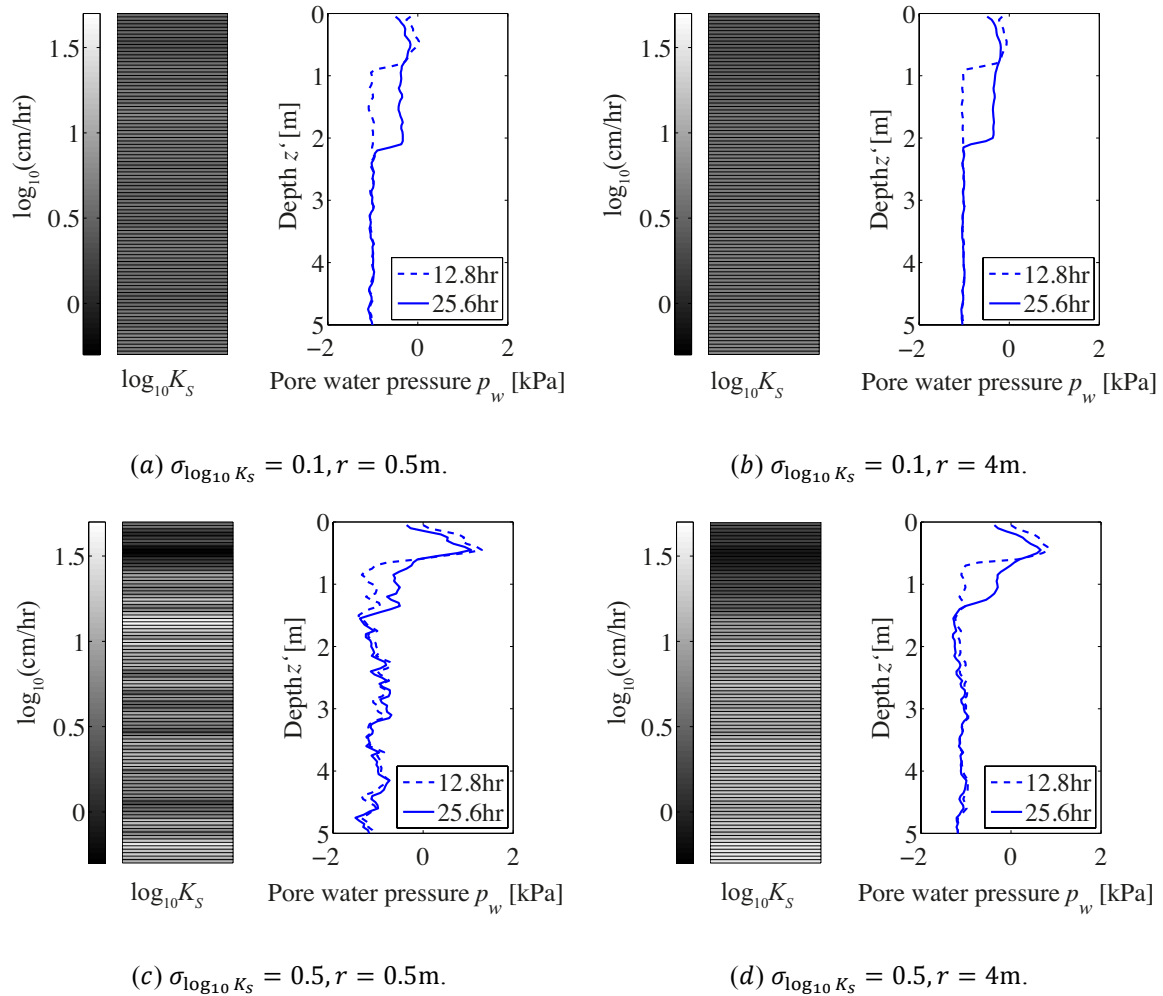


Figure 6.7 The pore water redistribution in the soil column with different values of the scale of fluctuation r and the standard deviation of saturated hydraulic conductivity in decimal logarithm scale $\sigma_{\log_{10} K_s}$.

Figure 6.8 shows the mean pore water redistribution with time at different depths for the considered scale of fluctuations and $\sigma_{\log_{10} K_s}$, $r = 0.5\text{m}$ and 4m , and $\sigma_{\log_{10} K_s} = 0.1$ and 0.5 , respectively. Figure 6.8(a) and (b) shows that in the case $\sigma_{\log_{10} K_s} = 0.1$, the mean pore water pressure at depth 1m is constant until influenced by rainwater infiltration when it gradually increases. The pore water pressures at depths 2m, 3m and 4m exhibit similar behavior. The influence of the scale of fluctuation in cases with $\sigma_{\log_{10} K_s} = 0.1$ is insignificant. In the case where $\sigma_{\log_{10} K_s}$ increases to $\sigma_{\log_{10} K_s} = 0.5$, the mean pore water pressure is influenced by rainwater infiltration earlier than for

6.3 Application of Richards equation to time-dependent reliability analysis

$\sigma_{\log_{10} K_s} = 0.1$ [cf. Figure 6.8 (a) and (c) or Figure 6.8 (b) and (d)], and it rises slower after the flow reaches the corresponding soil layers.

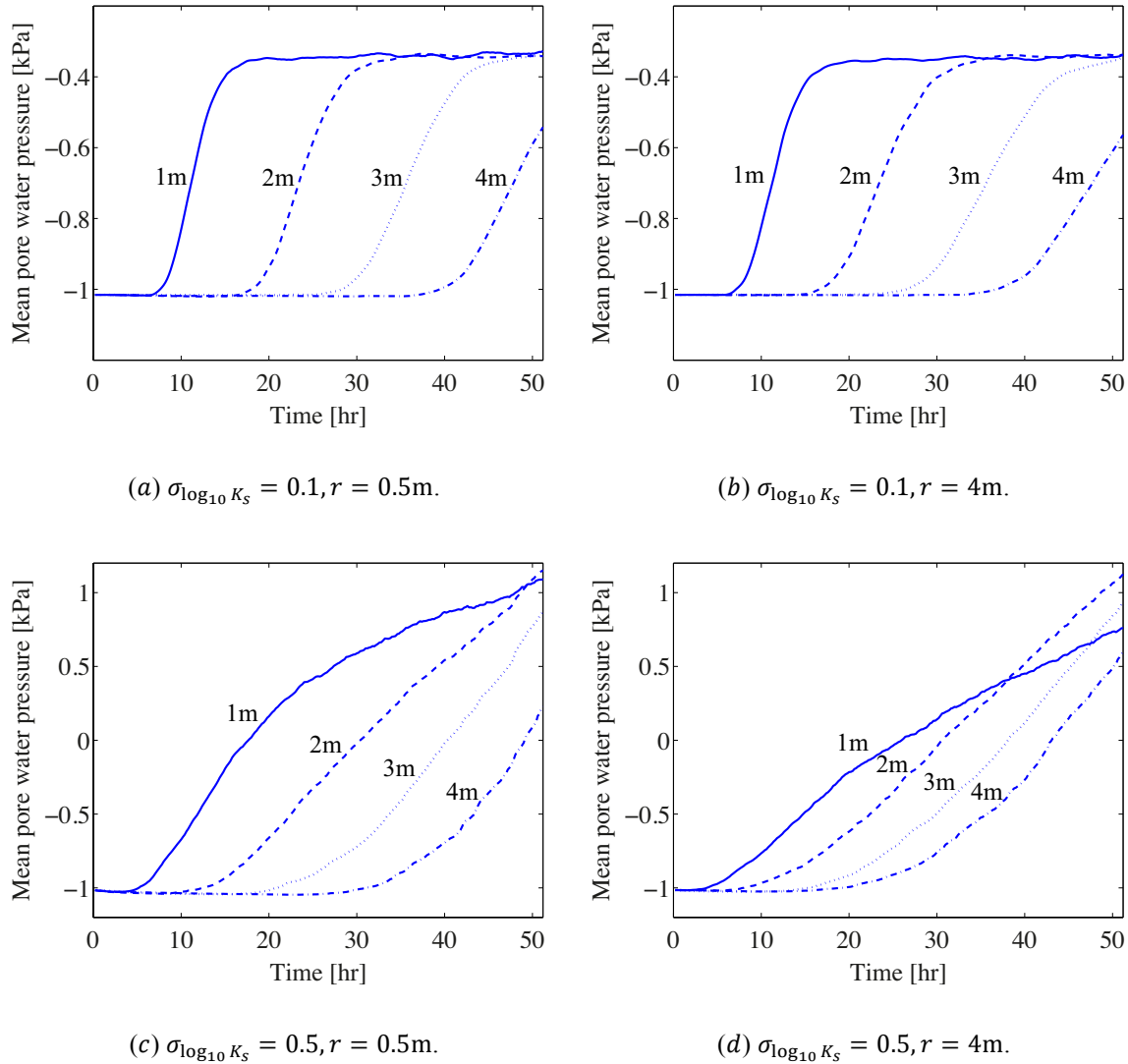


Figure 6.8 Pore water pressure at depths of 1m, 2m, 3m and 4m of the soil column, for different scales of fluctuation and $\sigma_{\log_{10} K_s}$, i.e. $r = 0.5\text{m}$, $r = 4\text{m}$, $\sigma_{\log_{10} K_s} = 0.1$ and $\sigma_{\log_{10} K_s} = 0.5$.

Figure 6.8 (c) illustrates that in the case $r = 0.5\text{m}$ and $\sigma_{\log_{10} K_s} = 0.5$, the mean pore water pressure at 1m depth increases gradually and continuously with the rainwater infiltration process. In Figure 6.8 (d), it is shown that for a larger scale of fluctuation $r = 4\text{m}$, the increase of the pore water pressure extends over a longer time period. These effects are due to the variability of the saturated hydraulic conductivity, which increases

with decrease of scale of fluctuation or increase of the standard deviation in decimal logarithm scale $\sigma_{\log_{10} K_s}$. A higher scale of fluctuation or a smaller $\sigma_{\log_{10} K_s}$ produces more homogeneous soil layers that absorb more rainwater through infiltration. Therefore, in the case of a smaller scale of fluctuation or a larger $\sigma_{\log_{10} K_s}$, a large amount of rainwater will form runoff at the ground surface due to the presence of lower permeable soil layers. In contrast, in the case with larger scale of fluctuation or a smaller $\sigma_{\log_{10} K_s}$, the shallow soil layers will be influenced by infiltration gradually and continuously. Hence it is expected that rainfall infiltration will affect higher soil layers in cases with smaller scale of fluctuation or larger $\sigma_{\log_{10} K_s}$ and deeper soil layers in cases with larger scale of fluctuation or smaller $\sigma_{\log_{10} K_s}$.

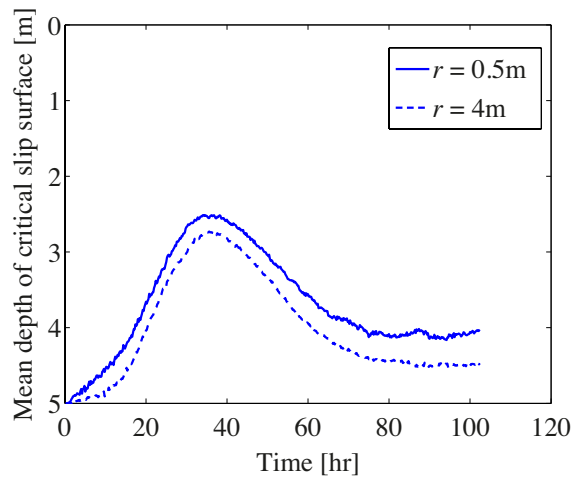
The point-in-time critical slip surface is the plane with the lowest factor of safety value FS among all potential slip surfaces, Eq. (4.28). Figure 6.9 shows the mean depth of the critical slip surface with respect to infiltration time for two slopes with different scales of fluctuation and $\sigma_{\log_{10} K_s}$ throughout a rainfall period of 102.4hr with an average rainfall intensity of 3cm/hr and parameters $a_0 = 12.27$ and $H = 0.47$.

In Figure 6.9(a), $\sigma_{\log_{10} K_s}$ is 0.1. At the beginning of the rainfall event, the mean critical slip surface is located at the bottom of the soil column, since within the unsaturated zone, the initial pore water pressure is negative and the factor of safety decreases with depth [see Eq. (4.27)]. The mean depth of the critical slip surface decreases at the onset of the rainfall event because of the pore water pressure redistribution. Between the two considered scales of fluctuation r , 0.5m and 4m, respectively, the case with smaller r leads to shallower mean critical slip surfaces. This is because in soils with smaller scale of fluctuation the pore water pressure is more likely to build up at shallow depths. With the wetting front development, the mean depth of critical slip surface then goes deeper in both cases.

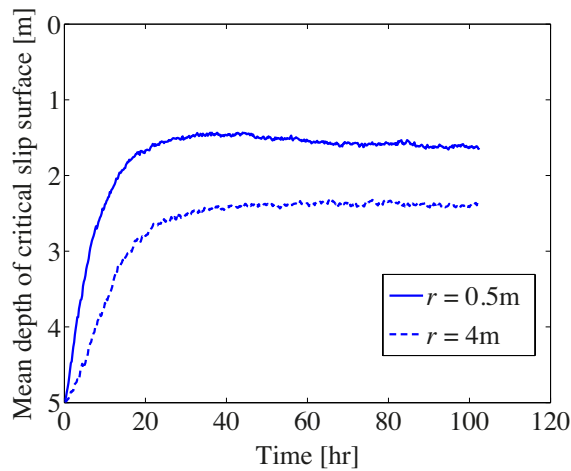
Figure 6.9(b) illustrates the relationship between the mean depth of the critical slip surface and rainfall time in the case with larger $\sigma_{\log_{10} K_s}$, i.e. $\sigma_{\log_{10} K_s} = 0.5$. The development of mean depth of the critical slip surface in the first 20hr exhibits a similar

6.3 Application of Richards equation to time-dependent reliability analysis

behavior as in Figure 6.8(a), although the depth rises much faster in this case. With further development of the wetting front, the mean depth of critical slip surface reaches a stable value for both considered scales of fluctuation and does not increase again as the rainfall progresses. This is because in the case with smaller $\sigma_{\log_{10} K_s}$ (i.e. lower variability) the rainwater infiltration is more likely to form nearly-saturated-flow within the soil column after a long period of the rainfall event, which can cause the depth of the critical slip surface to rise close to the bottom of the soil column.



(a) $\sigma_{\log_{10} K_s} = 0.1\text{m}$.



(b) $\sigma_{\log_{10} K_s} = 0.5\text{m}$.

Figure 6.9 Mean depth of critical slip surface in function of time, for different scales of fluctuation r and $\sigma_{\log_{10} K_s}$.

We investigate the influence of the variability in rainfall patterns on the pore water pressure redistribution. We consider an average rainfall intensity of 3cm/hr and duration of rainfall of 51.2hr. Figure 6.10 illustrates the redistribution of the pore water pressure for different random rainfall events using the same realization of saturated hydraulic conductivities within the soil slope for $r = 0.5\text{m}$. The random rainfall events are generated with $H = 0.47$, and $a_0 = 5$ and 20. The pore water pressure is plotted at the point in time when the rainfall stops. It is shown that the pore water pressure builds up faster for lower H , i.e. when the time variability of rainfall intensity is lower (cf. Fig. 3.5). This is because a low variability of the rainfall pattern will allow more rainwater to infiltrate into the soil slope, which will result in pore water pressure buildup. On the other hand, a rainfall pattern with high variability is more likely to produce runoff and hence will have a smaller effect on the pore water pressure redistribution.

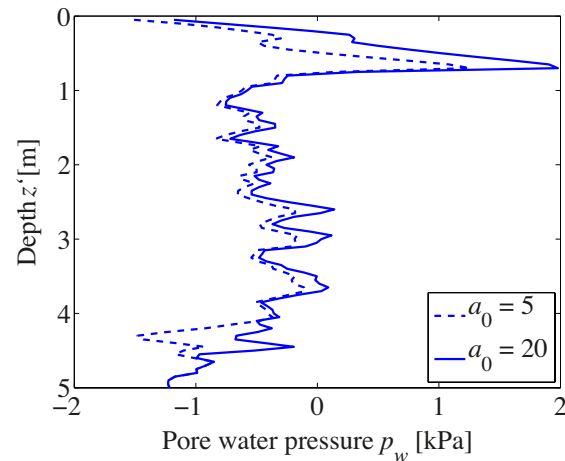


Figure 6.10 Realizations of pore water redistribution with different random rainfall events.

6.3.2 Probability of failure

We vary the number of steps N in the simulation of the rainfall event as $N = 5, 6, 7, 8, 9$ and evaluate the probability of failure for the corresponding time periods 3.2hr, 6.4hr, 12.8hr, 25.6hr, 51.2hr. The time step for the evaluation of the point-in-time factor of safety is chosen as 0.2hr. The average rainfall intensity is varied as 2cm/hr, 2.5cm/hr, 3cm/hr, 3.5cm/hr, 4cm/hr. The number of samples per Subset Simulation level is set to 10^3 , which was found to give acceptable coefficient of variations of the probability

6.3 Application of Richards equation to time-dependent reliability analysis

estimates for the cases considered. Figure 6.11 depicts the probability of slope failure in function of the average rainfall intensity and rainfall duration, for two considered scales of fluctuation $r = 0.5\text{m}$ and 4m .

As expected, the probability of failure increases with increasing rainfall duration and with increasing average rainfall intensity. The density of the contour lines represents the changing rate of the probability of failure. In the case with smaller scale of fluctuation ($r = 0.5\text{m}$), rapid changes of the probability occur when the average rainfall intensity increases from 2cm/hr to 3cm/hr . On the other hand, in the case with a larger scale of fluctuation ($r = 4\text{m}$), the probability of failure increases faster at higher rainfall intensities. This indicates that when the spatial variability of the soil is high, fast changes in p_w at shallow depths are likely to occur at shorter rainfall duration.

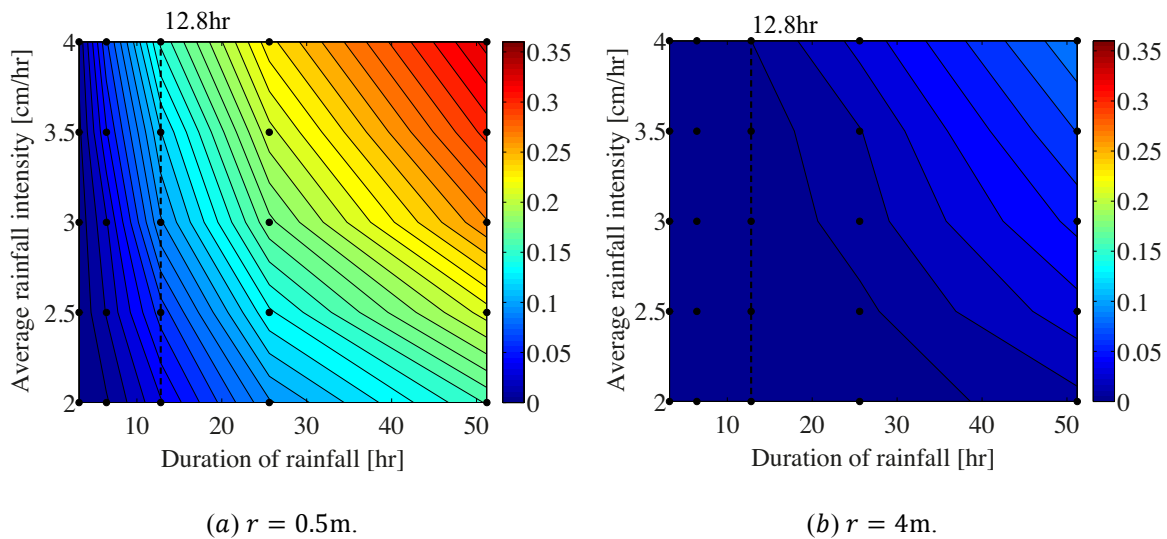


Figure 6.11 Comparison of probability of failure in cases with different r .

Figure 6.12 illustrates the influence of the scale of fluctuation on the probability of failure for a given time period of 12.8hr . For lower rainfall intensity, the probability of failure is larger in the case with smaller scale of fluctuation ($r = 0.5\text{m}$). This is because soils with high spatial variability will favor the occurrence of low after high permeability layers, and hence a larger p_w is more likely to build up at shallow depths. Therefore, in such cases, the critical slip plane is likely to be located near the ground surface. This

implies a simultaneous decrease of z' and increase of p_w in Eq. (4.11), which will result in a reduction of the critical factor of safety.

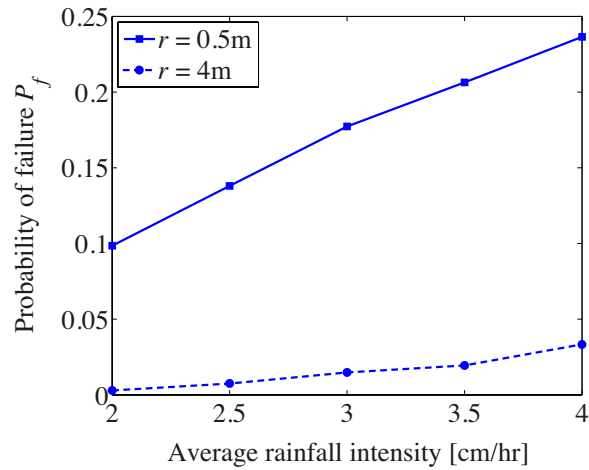


Figure 6.12 Comparison of probability of failure in cases with different r .

We investigate the effect of the rainfall characteristics. As discussed in Section 3.4, larger values of a_0 lead to a more uniform rainfall event (see Fig. 3.5). Figure 6.13 shows the influence of the self-similar random process parameter a_0 on the probability of failure. The value of the rainfall parameter H is 0.47 and the scale of fluctuation r is 0.5m. The probability of failure increases as a_0 increases, i.e. as the rainfall becomes more uniform. It indicates that smaller variability of the rainfall process leads to a larger probability of failure.

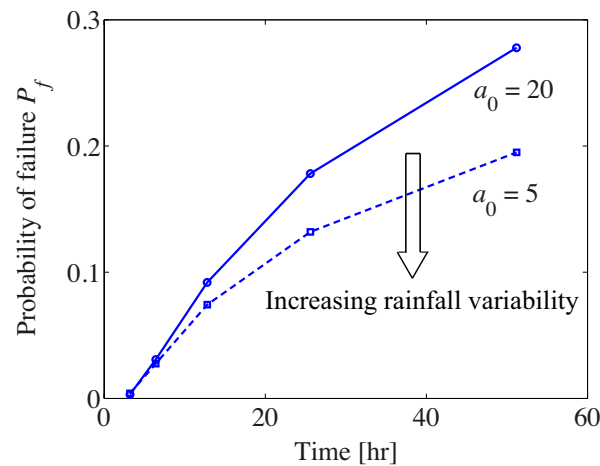


Figure 6.13 Comparison of probability of failure in cases with different a_0 , $H = 0.47$.

6.4 Bayesian updating

In these cases, more rainwater becomes infiltration and causes a larger hydraulic gradient within the soil slope. This in turn leads to a larger pore water pressure when the rainfall intensity is below the water capacity of the slope (see Fig. 6.11). Since the water capacity of the slope is larger at the beginning of the rainfall event and decreases with infiltration volume accumulation, the excess rainwater will form runoff at the ground surface and will not affect pore water pressure buildup and the slope stability.

6.4 Bayesian updating

In this section, we apply Bayesian analysis to update the distribution of the saturated hydraulic conductivity K_s with measurements of the pore water pressure along the depth of the soil profile. The lower boundary condition is set as a fixed volumetric water content, i.e. $\theta = \theta_s$. We consider the infinite slope in sandy soil presented in Section 6.1. In the context of Bayesian analysis, we need to define the prior distribution of the hydraulic conductivity. We model the prior distribution of K_s with a lognormal random field with median 3.6cm/hr. The standard deviation in log-scale, i.e. the standard deviation of $\log_{10} K_s$, is 0.5 and the scale of fluctuation is 5m. The random field is discretized applying a discrete KL expansion based on 100 equal thickness layers. Therefore, Bayesian updating is applied to learn the posterior distribution of the random variables in the KL expansion. In the KL representation the 10 random variables corresponding to the larger eigenvalues are retained, which decreases considerably the dimension of the updating problem. The layers of the infinite sandy slope are assumed to have the same water content $\theta_0 = 0.2$ before the rainwater infiltration. The remaining permeability parameters of the sandy soil are modeled deterministically, and their values are listed as Tab. 5.2.

The distribution of K_s is updated with synthetic measurements of the pore water pressure. We assume the rainfall event with duration of 51.2hr shown in Fig. 6.14 is measured in the field. This measurement is generated using the self-similar random process model discussed in Section 3.4 for an average intensity of 8cm/hr and parameters of the random process model $a_0 = 12.27$ and $H = 0.47$. In order to generate synthetic measurements of the pore water pressure, we draw a realization from the prior

distribution of K_s and evaluate the corresponding pore water pressure distribution by application of the infiltration model based on Richards equation. The permeability parameters used in this model are the ones shown in Tab. 6.2.

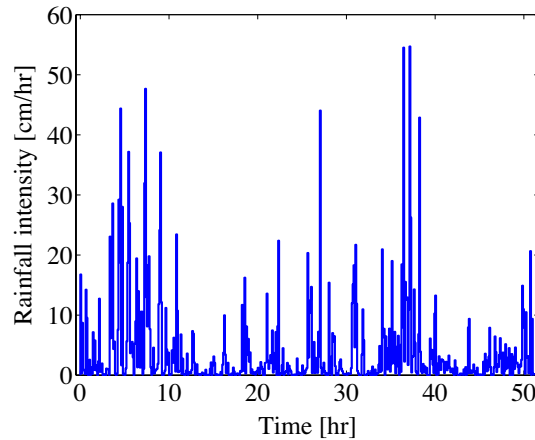


Figure 6.14 A rainfall event with duration of 51.2hr.

In order to make better use of the measurements, it is of interest to choose appropriate time steps and infiltration layers for the pore water pressure data that are used in the Bayesian analysis. This is because including a large number of data will render the problem overdetermined, which makes it difficult to obtain reliable solutions with the Bayesian updating algorithm. Figure 6.15 illustrates the relationship between the relative hydraulic conductivity K_r and pressure head h within the sandy soil (c.f. Fig. 2.5). In Figure 6.15, the pressure head ψ here is plotted in logarithm scale. This figure shows that when the pressure head varies from -0.1kPa to -1kPa the relative hydraulic conductivity K_r changes rapidly. This part can be named as “rapid-changing area” and is meaningful for setting observation points. Moreover, it is known that, the pore water pressure significantly increases with respect to the wetting front development. Nevertheless, the numerical solution of Richards equation is not stable around the wetting front (Phoon et al. 2007). It is not proper to arrange all observation points within the location where it has large changes. The rest part of the curve is relatively smooth, yet it does not provide adequate information for identifying the permeability of soil layers. Thus, the principle of selecting observation points is as follows: 1) Not too many points within the rapid-changing area; 2) Not too close to the wetting front.

6.4 Bayesian updating

Another issue that is of interest when performing the Bayesian updating with pore water pressure data is that for certain cases of spatial distribution of the hydraulic conductivity the infiltration model becomes not uniquely identifiable. This is illustrated in Figure 6.15. Note that the infiltration model assumes that the wetting and drying phases follow the same path (solid blue line). Points P_1 and P_2 represent two arbitrary states of the sandy soil (see Fig. 6.15). Because of the spatial variability of the hydraulic conductivity and the randomness in the rainfall patterns, one could find many trajectories from point P_1 to point P_2 . For instance, one can find at least two paths, i.e. one direct way is to follow the solid line and the other is shown as the dash line. The latter indicates one of many possible combinations of the wetting and drying process. Notice that, the initial and final states are the same for the two paths, yet their runtime is different. Recalling the Richards equation in Eq. (2.28), one could infer that, different paths lead to multiple solutions. In addition, the classical analytical solution of Richards equation (1931) comprises many periodic terms as it applies Fourier transformation (e.g. Fred 2011). As discussed in Section 5.3, periodic models with high frequencies lead to multimodal likelihood functions that affect the efficiency of sampling-based Bayesian methods. The frequencies of periodic terms in the numerical solution of Richards equation become lower in cases where the saturated hydraulic conductivity decreases gradually with depth. Such cases are often observed in the field due to the natural soil deposition processes. Therefore, in this study we add a bias term to the realization of the hydraulic conductivity used to generate the observations that increases linearly with depth.

The pore water pressure is observed with respect to the time and depth. The measurements are obtained as follows:

$$y_i = p_w(t_i, d_i) + \epsilon_i, i = 1, 2, \dots, m \quad (6.1)$$

in which t_i is the observation time; d_i is the observation depth; m is the number of observation points and ϵ_i is a Gaussian error term with standard deviation 0.1kPa. The likelihood function of the observations can be calculated following Eq. (5.10). Bayesian updating is performed with the adaptive version of BUS with Subset Simulation, described in Section 5.2.3. The number of samples per level is chosen as 1000 and the

intermediate conditional probability is $p_0 = 0.1$.

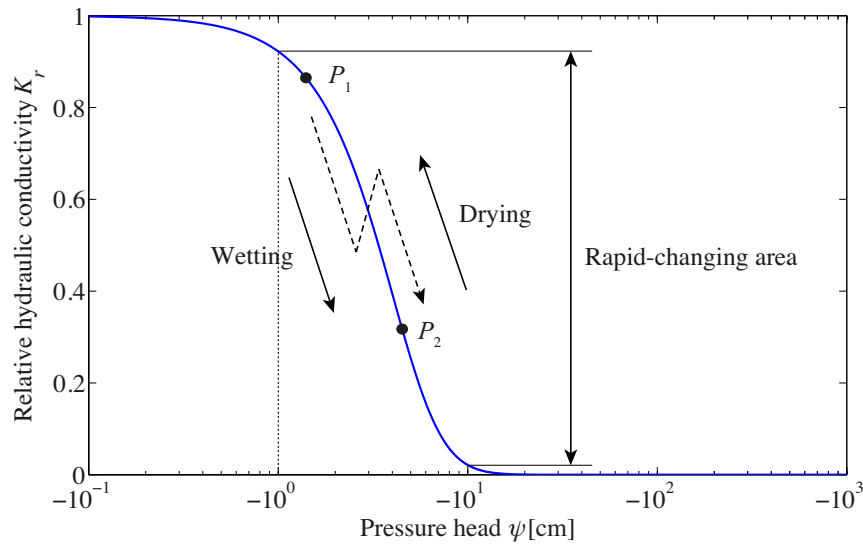


Figure 6.15 Relative hydraulic conductivities in terms of the pressure head for sandy soils, and the parameters are given by $\alpha = 0.145\text{cm}^{-1}$, $n = 2.68$ (Šimůnek 2009).

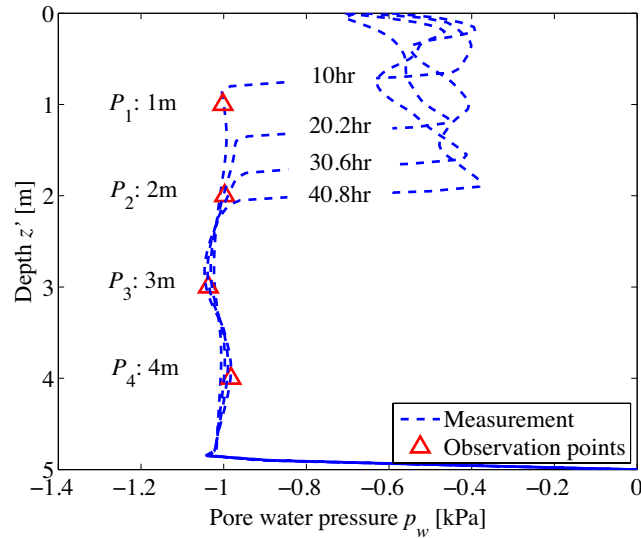
Two different data sets are chosen. Figure 6.16 illustrates the redistribution of the pore water pressure with respect to the time and depth during the rainwater infiltration for the realization of the hydraulic conductivity used to generate the data.

Figure 6.16(a) shows the pore water pressure redistribution at four time points, i.e. 10hr, 20.2hr, 30.6hr and 40.8hr. The depths of observation points of the first data set are located at 1m, 2m, 3m and 4m, respectively. According to Figure 6.16(a), at 10hr and 20.2hr the notable wetting front is located around the depth of 0.9m and 1.5m, respectively. At 30.6hr and 40.8hr, the wetting front development becomes slower. Intuitively, the pore water pressure will be built-up above the wetting front. In contrast, below the wetting front, the pore water pressure does not vary significantly during infiltration. For the same realization of the hydraulic conductivity, we choose measurements of the pore water pressure redistribution at six time points, i.e. 7hr, 14.4hr, 21.8hr, 29.2hr, 36.4hr and 43.8hr.

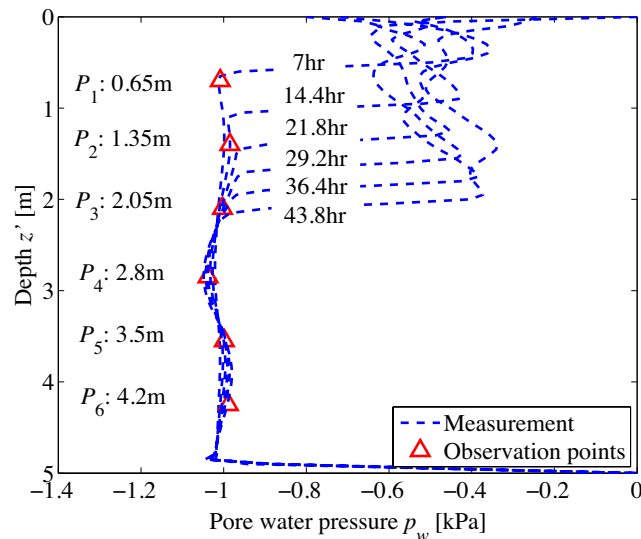
The measurements are plotted in Figure 6.16(b). The depths of corresponding observation points are located at 0.65m, 1.35m, 2.05m, 2.8m, 3.5m and 4.2m,

6.4 Bayesian updating

respectively. In analogy to the previous case, the wetting front advances faster at the beginning and it slows down after around 21.8hr. The observation points are chosen below the wetting front and this is based on the two discussed principles.



(a) Four observation points.



(b) Six observation points.

Figure 6.16 Pore water pressure redistribution with respect to wetting front development.

Figure 6.17(a) and (b) illustrate the comparison among the real distribution of the saturated hydraulic conductivity, the posterior mean and 95% credible intervals with four and six measurement points, respectively. It is shown that, in Figure 6.17(a) the posterior

mean of saturated hydraulic conductivities is close to the true values, whereas in Figure 6.17(b) the posterior mean and true values at some locations do not agree well. This is probably due to the fact that, the identification of $K_s(\mathbf{z}')$ greatly relies on locations of observation points. In the latter case, some points are near the wetting front, where the infiltration model is subjected to numerical noise. In the first case, the true value is within the credible interval, whereas in the second case the true value exceeds the upper credible bound in some regions.

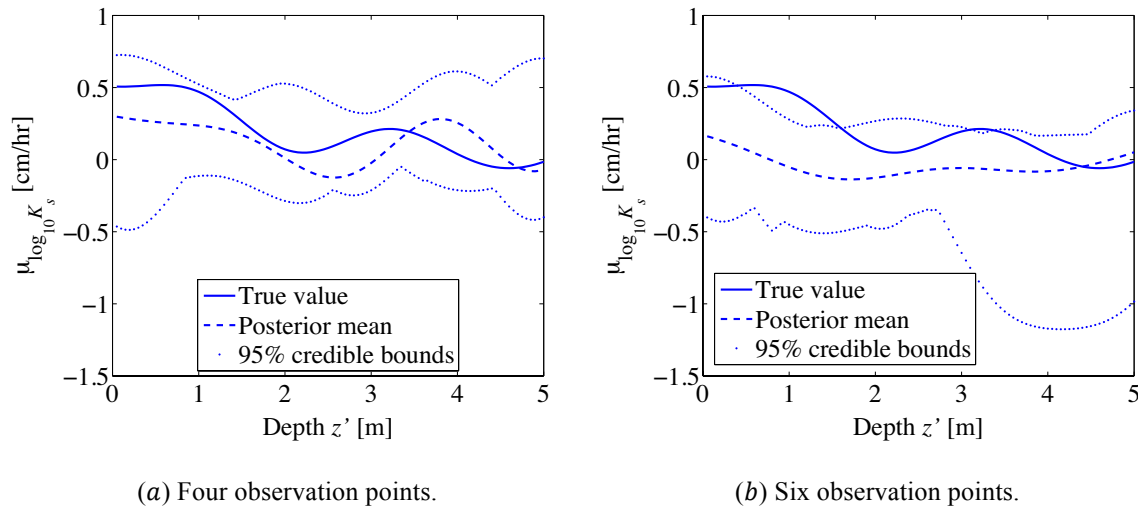


Figure 6.17 The posterior distributions of saturated hydraulic conductivities.

Figure 6.18 compares the mean of the pore water pressure obtained by the prior hypothesis and posterior distribution of saturated hydraulic conductivities with the measurements. In Figure 6.18(a) the posterior distribution moves toward the measurement at points located at 1m, 2m and 3m, yet the last point does not match well. This is probably because the pore water pressure at this point is not influenced by $K_s(\mathbf{z}')$ throughout the infiltration process. For the same reason, the posterior mean of the last three points in Figure 6.18(b) differs from the measurement. However, the differences in both cases are minor. This validates the ability of the adaptive BUS-SuS approach to identify the measurements.

6.4 Bayesian updating

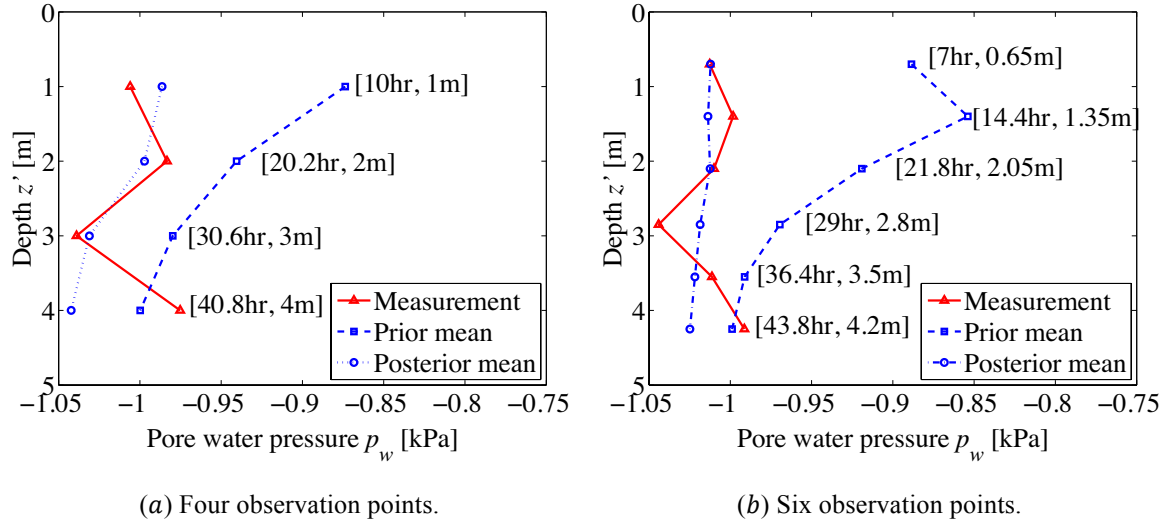


Figure 6.18 Pore water pressure obtained by the prior, posterior and measurement.

Figure 6.19 depicts the comparison between the prior and posterior mean factor of safety with four and six measurement points. The posterior mean is evaluated considering a random rainfall event with duration 51.2hr, average intensity 2cm/hr and parameters of the self-similar random process model $a_0 = 12.27$ and $H = 0.47$. The posterior mean factor of safety nearly overlaps with the prior mean curve at the first few hours. The posterior mean becomes smaller than the prior after the first 20hrs. In other words, according to the prior knowledge, we will underestimate the average influence of the rainfall infiltration on the slope stability. Because of the wetting front development (see Fig. 6.16), below about 3m depth for both cases a Bayesian analysis can learn less information from the measurements, since $K_s(\mathbf{z})$ has little influence on the pore water pressure redistribution. The wetting front has not reached 3m for both cases until the rainfall stops (see Fig. 6.16), i.e. 51.2hr. Since the most critical slip surface is above the wetting front, the rest of soil layers will not affect the stability of soil slope. The computation results are reliable within the time domain $[0, 51.2\text{hr}]$ in consideration of the wetting front development.

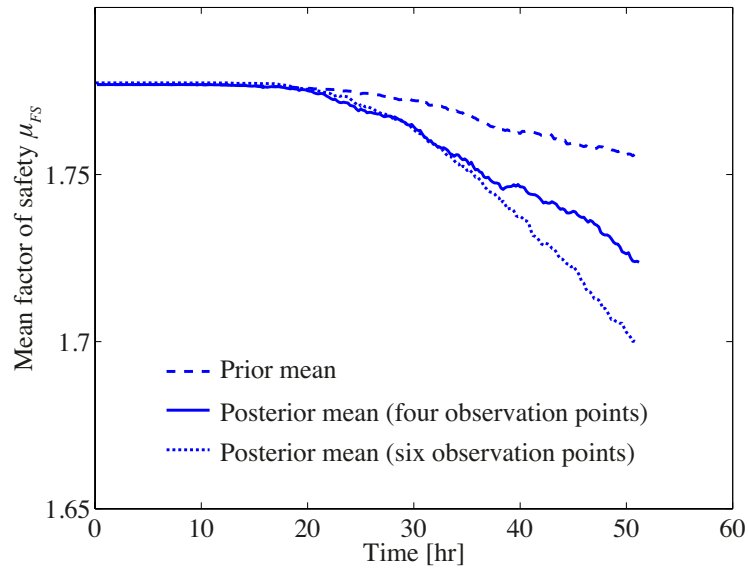


Figure 6.19 Mean factor of safety.

Chapter 7 Conclusions

7.1 Conclusions

Landslide hazards are present in many places around the world, leading to severe damages and fatalities. Proper assessment of the risks due to landslide hazards requires a rigorous probabilistic modeling of the input uncertainties in soil parameters and rainfall conditions. This thesis focuses on shallow slope failures and presents an approach for probabilistic assessment of slope stability of infinite slopes subjected to intense rainfall events. Two different physical-based infiltration models are studied. The first is a multi-layered extension of the Green and Ampt model and assumes a distinct wetting front between “wetted” and “dry” zones. The second infiltration model is based on a numerical solution of Richards equation. The spatial variability of permeability parameters of the soil is represented with random fields. In addition, the randomness in the rainfall patterns is modeled with self-similar random process theory. The reliability of the slope is evaluated with Subset Simulation, which is an adaptive Monte Carlo method that is efficient in estimating failure probabilities in high dimensions. Finally, the updating of predictions with field measurements is investigated through application of Bayesian analysis. Bayesian updating is performed using an efficient sampling technique, namely the BUS approach combined with Subset Simulation.

In the first case study, the extended Green and Ampt model is applied and the spatial variability of saturated hydraulic conductivity and suction head is modelled with correlated lognormal random fields. The mean behavior of the wetting front development and the factor of safety of the slope are evaluated with Monte Carlo simulation and the cumulative probability of failure for different wetting front depths is computed with Subset Simulation. In a case study, we investigate the influence of the scale of fluctuation and the standard deviation of the logarithm of the hydraulic conductivity and the suction head on the wetting front development, the mean factor of safety and the probability of failure of the slope. It is shown that decreasing the scale of fluctuation or increasing the

7.1 Conclusions

standard deviation of saturated hydraulic conductivity will increase the variability of the soil layer permeability. This increases the likelihood of occurrence of low permeability values, which decreases the effective hydraulic conductivity within the wetting zone, thus leading to slower movement of the wetting front. A decrease in the scale of fluctuation has a significant influence on the transient behavior of the factor of safety. In particular, it is shown that a decrease in the scale of fluctuation leads to faster decrease in the mean factor of safety with the wetting front development, due to larger pore pressure build-up at shallow depths, which favors shallow slope failure. This leads to large failure probabilities at shallow depths of the wetting front. A change in the standard deviation of the random fields does not have significant influence on the mean depth of the critical slip surface within the wetted zone. The probability of failure increases faster with the development of the wetting front at the beginning of the infiltration with increasing standard deviation. However, the impact of the latter on the maximum value of the probability of failure is shown to be significant.

The second case study presents the reliability assessment of an infinite slope subjected to random rainfall events, employing a numerical solution of Richards equation to model the infiltration process. The spatial variability of the saturated hydraulic conductivity is again modeled with a lognormal random field. In addition, the random rainfall patterns are modeled by application of self-similar random process theory. The reliability analysis is performed with Subset Simulation. The probability of slope failure is evaluated conditional on different average intensities and durations of the rainfall event for different values of the scale of fluctuation of the hydraulic conductivity and the parameters of the self-similar random process modeling the rainfall event. This case study shows that in short duration rainfall events, the probability of failure increases as the scale of fluctuation of the saturated hydraulic conductivity decreases. This is because in slopes with small scale of fluctuation, the critical slip surface is likely to be located in shallow depths. Moreover, it is shown that more uniform rainfall patterns lead to higher infiltration volume and result in higher pore water pressure buildup that increases the probability of failure of the infinite slope. However, the influence of water capacity of the infinite slope cannot be ignored, because the runoff part of rainwater will not affect the slope reliability. This effect is more pronounced in soils with small scale of fluctuation

where layers with low hydraulic conductivity that may result in saturated flow are more likely to occur. In rainfall events with long duration, the water capacity of slopes with large scale of fluctuation remains high throughout the rainfall event, which leads to a larger probability of failure as compared to slopes with small scale of fluctuation.

Finally, the third case study presents an application of Bayesian analysis to learn the probability distribution of hydraulic conductivity with measurements of the pore water pressure and update the factor of safety of the infinite slope. Here, the infiltration model used is again based on the numerical solution of the Richards equation. The Bayesian updating is performed with the BUS approach combined with Subset Simulation. In order to make better use of the measurements, only the data points above the wetting front development are used in the Bayesian analysis, since the effect of the rainwater infiltration on the pore water pressure is stronger above the wetting front. However, to avoid the oscillatory terms that are present in the numerical solution of the infiltration model close to the wetting front, the observation points should not be located too close to the wetting front. The results demonstrate how measurements of the pore water pressure could potentially influence the posterior statistics of the factor of safety. In particular, it is shown that pore water pressure measurements provide little information for updating the factor of safety within saturated zones. In order to perform accurate updating within saturated zones, it is necessary to include additional sources of information, e.g. monitoring data from soil deformation or inclination.

7.2 Discussion and outlook

The Green and Ampt model assumes that a well defined wetting front separates the wetted and dry zone during rainwater infiltration. This approximation is good for sandy soil types, in which the rainwater is driven by gravity with uniform water content (Bear 1972). For other soil types, such as clayey soil, the water flow will not move like a piston and the shape of the wetting front is not as sharp as in sandy soils. Therefore, the accuracy of the Green and Ampt model is higher for sandy soils. In addition, the proposed extension of the Green and Ampt model for dealing with multiple layers is more accurate with decreasing saturated hydraulic conductivities along depth of the soil

7.2 Discussion and outlook

column. The advantage of the extended Green and Ampt model over the model based on Richards equation is its computational efficiency. On the other hand, the model based on the numerical solution of the Richards equation is accurate independent of the soil type and the spatial distribution of hydraulic conductivity. It should be pointed out that the stability of the numerical solution of Richards equation for the pressure head close to the wetting front is not guaranteed for all time steps and mesh sizes. Numerical stability is not an issue for the extended Green and Ampt model because the suction head concept defines the solution at the wetting front. The upper boundary condition in the current implementation of the extended Green and Ampt model are uninterrupted intense rainfall events, whereas arbitrary rainfall patterns (e.g. generated based on self similar random process theory) can be applied to the infinite slope in the model based on Richards equation.

The BUS approach with Subset Simulation, as well as most sampling based Bayesian methods, encounters difficulties in problems that are not uniquely identifiable. This issue occurs in the infiltration model based on Richards equation, because its numerical solution involves periodic terms. This problem appears to be less severe in cases where the saturated hydraulic conductivities are gradually decreasing along the depth. Such cases are commonly observed in real sites due to the natural soil deposition process. In addition, the numerical solution of Richards equation is not stable near the wetting front. Therefore, the data points used in the Bayesian updating process should be selected based on the following principles: 1) Not too many points within the rapid-changing area; 2) no points too close to the wetting front.

Based on the above discussion, the following possible future research topics have been identified:

- Modification of the extended Green and Ampt model in order to deal with arbitrary rainfall boundary conditions, such as random rainfall patterns.
- Consideration of the uncertainty of additional parameters, such as the initial and saturated water content.
- Study of the effect of pore water pressure as well as other types of measurements

on the probability of failure of the infinite slope.

- Combination of the reliability analysis and Bayesian updating method with a surrogate model (e.g. based on Neural Networks or Gaussian process models) of the infiltration model to enhance computational efficiency and achieve real time assessment.
- Study of the reliability of slope stability for cases where the hydraulic conductivity is modeled with a non-stationary random field. As an example, the performance of the two infiltration models could be compared for the case where the mean value of the hydraulic conductivity decreases with depth.
- The Green and Ampt model is expected to be more accurate for cases where the hydraulic conductivity decreases with depth. Therefore, it becomes interesting to study the performance of the Green and Ampt model in Bayesian updating of such cases.
- Ultimately, it would be of interest to extend this study to $2D$ infiltration models combined with $2D$ finite element analysis for determining the slope stability. This would also enable employing measurements of soil deformations to learn the distribution of permeability parameters with Bayesian updating.

Annex A. Numerical solutions for Richards equation

This Annex discusses a method for the numerical solution of the one dimensional Richards equation. Before introducing the numerical solution, two fundamental strategies for simplifying Eq. (2.27) are presented here, namely the head-based formulation and the saturation-based formulation.

Here we only concentrate on the one dimension case, whereby flow is assumed along the z' direction [see Figure 2.1(a)]. The head-based formulation is given as follows

$$C(h) \frac{\partial h}{\partial t} = \frac{\partial}{\partial z'} \left(K \frac{\partial h}{\partial z'} \right) \quad (\text{A.1})$$

in which $C(h)$ is a function describing the rate of change of saturation with respect to the hydraulic head, i.e. $C(h) = \frac{\partial \theta}{\partial h}$.

The saturation-based formulation is given as,

$$\frac{\partial \theta}{\partial t} = \frac{\partial}{\partial z'} \left[D(\theta) \frac{\partial \theta}{\partial z'} \right] \quad (\text{A.2})$$

in which $D(\theta)$ is the soil water diffusivity, i.e. $D(\theta) = K(\theta) \cdot \frac{\partial h}{\partial \theta}$.

In the following, an example is given for solving 1D horizontal flow by applying saturated-based formulation. Consider the case where the soil water diffusivity $D(\theta)$ is constant throughout the entire soil column, i.e. $D(\theta) = \text{constant}$. According to Eq. (A.2), Richards equation can be further simplified to:

$$\frac{\partial \theta}{\partial t} = D(\theta) \frac{\partial^2 \theta}{\partial z'^2} \quad (\text{A.3})$$

Expanding Eq. (A.3) by means of first order finite difference method, it yields,

$$\frac{\theta_{i,j+1} - \theta_{i,j}}{\Delta t} = D(\theta) \frac{\theta_{i-1,j} - 2\theta_{i,j} + \theta_{i+1,j}}{\Delta x^2} \quad (\text{A.4})$$

in which $\theta_{i,j}$ is the water content at the i th computational layer and j th time step; Δt is the length of time step; Δx is the length of the computational layer.

By rearranging terms, the following form can be obtained:

$$\theta_{i,j+1} - \theta_{i,j} = D(\theta) \frac{\Delta t}{\Delta x^2} (\theta_{i-1,j} - 2\theta_{i,j} + \theta_{i+1,j}) \quad (\text{A.5})$$

By substituting $\lambda = D(\theta) \frac{\Delta t}{\Delta x^2}$ into Eq. (A.5), we get

$$\theta_{i,j+1} = \lambda\theta_{i-1,j} + (1 - 2\lambda)\theta_{i,j} + \lambda\theta_{i+1,j} \quad (\text{A.6})$$

Using the backward difference method, i.e. replacing $j + 1$ by j , the following equation can be obtained

$$\theta_{i,j} = \lambda\theta_{i-1,j-1} + (1 - 2\lambda)\theta_{i,j-1} + \lambda\theta_{i+1,j-1} \quad (\text{A.7})$$

Thus, the water content for a given time $t = j\Delta t$ and location $x = i\Delta x$ is expressed as a function of the moisture content at the previous step ($j - 1$) at the same (i) as well as adjacent ($i - 1$ and $i + 1$) locations. Because the initial boundary locations are known, $\theta_{i,j}$ can be computed directly (thus explicitly) at all time and locations by repeated application of the above equation starting from $t = 0$.

Notice that the stability of the solution from the explicit scheme is dependent on the value of lambda. For $0 \leq \lambda \leq 0.5$ the solution remains stable (e.g. Caputo and Stepanyants 2008). For values outside this range, stability is not guaranteed.

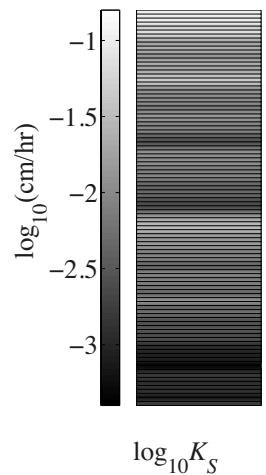
Annex B. Validation of the extended Green and Ampt model

This Annex discusses the performance of the extended Green and Ampt model with the help of a numerical example. We consider an infinite slope in a sandy subsoil subject to an intense rainfall event. The soil column is 5m deep with idealized free-draining lower boundary. The slope angle is $\beta = 18^\circ$. The unit weight of water is 10kN/m^3 . The direct effects of matric suction on the effective stress, and as such the stability of the slope, are neglected in the extended Green and Ampt model. The saturated vertical hydraulic conductivity K_s is modelled by a statistically homogeneous lognormal random fields with median $M_{K_s} = 3.6 \text{ cm/hr}$. The suction head S is a constant at $S = 15\text{cm}$. These values are typical for loamy sands (Rawls et al. 1983). The standard deviation and the scale of fluctuation of the decimal logarithm of the random field are taken as 0.5 and 5m, respectively. The random field is discretized into 100 layers with thickness $\Delta z = 0.05\text{m}$. The deterministic parameters of the Green and Ampt model for loamy sand are taken from Rawls et al. (1982) and Rawls et al. (1983) and are summarized in Tab. 1.

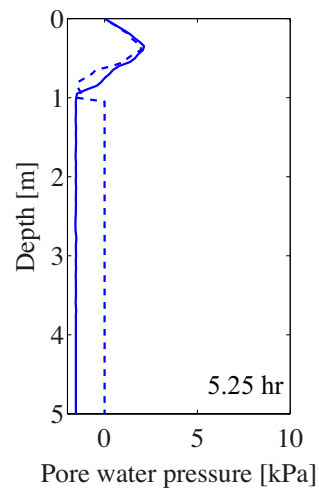
Table B.1 Parameters for Green and Ampt model.

Parameters	Definition	Value
K_s	Saturated hydraulic conductivity	$M_{K_s} = 3.6\text{cm/hr}$
$ S $	Suction head	15 cm
θ_s	Saturated water content	0.437
θ_0	Initial water content	0.125

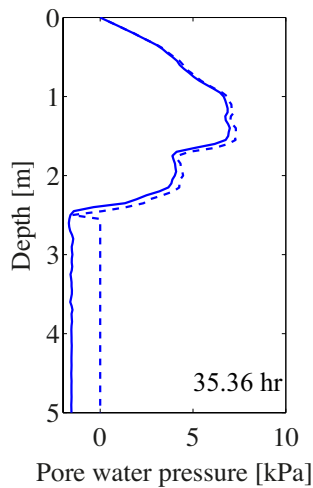
Comparing the two models for the particular realization of the random field shown in Figure B.1. As discussed in Chapter 2, the extended Green and Ampt model computes the cumulative infiltration time and corresponding pore water pressure distribution for each discrete computational layer, whereas Richards equation computes the pore water pressure as a function time. To make the two models comparable, we fix the location of wetting front and obtain the pore water pressure as well as the infiltration time of one realization of the random field through the extended Green and Ampt model and subsequently at the corresponding point in time compute the pore water pressure redistribution by means of HYDRUS-1D.



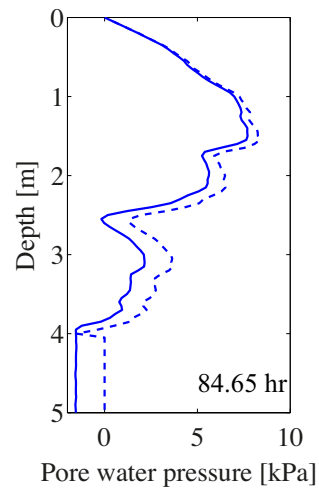
(a) The distribution of saturated hydraulic conductivities



(b) The wetting front is located at 1m by using 5.25hr



(c) The wetting front is located at 2.5m by using 35.36hr



(d) The wetting front is located at 4m by using 84.65hr

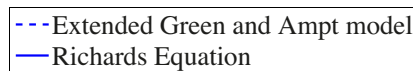


Figure B.1 Comparison between extended GA model and Richards equation.

Figure B. 1 shows the comparison of the pore water redistribution obtained by two models when the wetting front locates at 1, 2.5 and 4m after 5.25, 35.36 and 84.65hr, respectively. In this example, the solutions of the pore water pressure redistribution above

the wetting front by the two models are quite close at three time points. Notice that positive pore water pressure can be well predicated by the extended Green and Ampt model. This is because the assumptions of the model on the wetting front development as well as the pore water pressure are valid when the rainwater flows through the decreasing permeability soil layers. Otherwise, the computation results can lead to errors, particularly in cases with large variability of permeability. Known from Figure B.1(a) that the extended Green and Ampt model is more valid for cases with the permeability decreasing with depth, through which the pore water pressure is easy to be built up.

Annex C. Commonly used distributions

This annex presents two commonly used distributions of continuous random variables.

Normal or Gaussian distribution

The Gaussian distribution is of great importance in the fields of probability and statistics. Moreover, it is one of the most frequently used distributions in engineering problems. A Gaussian random variable $X \sim N(\mu, \sigma)$ is defined by two parameters, the mean value μ and the standard deviation σ . Its PDF is as follows:

$$f_X(x) = \frac{1}{\sigma} \varphi\left(\frac{x-\mu}{\sigma}\right) = \frac{1}{\sigma\sqrt{2\pi}} \exp\left[-\frac{(x-\mu)^2}{2\sigma^2}\right] \quad x \in (-\infty, +\infty) \quad (\text{C.1})$$

where $\varphi(\cdot)$ is the standard normal PDF operator associated with the standard normal random variable $U \sim N(0,1)$:

$$\varphi(u) = \frac{1}{\sqrt{2\pi}} \exp\left(-\frac{u^2}{2}\right) \quad u \in (-\infty, +\infty) \quad (\text{C.2})$$

The CDF of $X \sim N(\mu, \sigma)$ is as follows:

$$F_X(x) = \Phi\left(\frac{x-\mu}{\sigma}\right) \quad (\text{C.3})$$

where $\Phi(\cdot)$ is the standard normal CDF operator:

$$\Phi(u) = \int_{-\infty}^u \frac{1}{\sqrt{2\pi}} \exp\left(-\frac{z^2}{2}\right) dz \quad (\text{C.4})$$

Lognormal distribution

If Y is a random variable with a normal distribution, then $X = \exp(Y)$ has a lognormal distribution; vice versa, if X is lognormally distributed, then $Y = \ln(X)$ has a normal distribution. Assume Y is normal distribution with parameters μ_Y and σ_Y , then the PDF of the lognormal distribution reads:

$$f_X(x) = \frac{1}{x} \cdot \frac{1}{\sigma_Y \sqrt{2\pi}} \cdot \exp \left[-\frac{1}{2} \left(\frac{\ln x - \mu_Y}{\sigma_Y} \right)^2 \right] \quad (\text{C.5})$$

On a logarithmic scale, μ_Y and σ_Y can be called the location parameter and the scale parameter. Alternatively, the PDF and the CDF of the lognormal distribution can also be expressed through the standard Normal PDF and CDF by:

$$f_X(x) = \frac{1}{x} \cdot \varphi \left(\frac{\ln x - \mu_Y}{\sigma_Y} \right) \quad (\text{C.6})$$

$$F_X(x) = \Phi \left(\frac{\ln x - \mu_Y}{\sigma_Y} \right) \quad (\text{C.7})$$

The corresponding mean, variance and standard deviation of X can be computed as follows:

$$E[X] = \exp \left(\mu_Y + \frac{\sigma_Y^2}{2} \right) \quad (\text{C.8})$$

$$\text{Var}[X] = \exp(2\mu_Y + \sigma_Y^2) [\exp(\sigma_Y^2) - 1] \quad (\text{C.9})$$

$$\sigma_X = \exp \left(\mu_Y + \frac{\sigma_Y^2}{2} \right) \sqrt{\exp(\sigma_Y^2) - 1} \quad (\text{C.10})$$

According to Eq. (3.9), the coefficient of variation of a random variable with lognormal distribution is:

$$\text{CV}_X = \frac{\sigma_X}{E[X]} = \sqrt{\exp(\sigma_Y^2) - 1} \quad (\text{C.11})$$

The median and mode of the lognormal distribution are given by:

$$x_{0.5} = \exp \mu_Y \quad (\text{C.12})$$

$$\tilde{x} = \exp (\mu_Y - \sigma_Y^2) \quad (\text{C.13})$$

Likewise, parameters μ_Y and σ_Y can be obtained if the expected value and variance of X are known:

$$\mu_Y = \ln(E[X]) - \frac{1}{2} \ln \left(1 + \frac{\text{Var}[X]}{(E[X])^2} \right) = \ln(E[X]) - \frac{1}{2} \ln(1 + \text{CV}_X^2) \quad (\text{C.14})$$

$$\sigma_Y^2 = \ln \left(1 + \frac{\text{Var}[X]}{(E[X])^2} \right) = \ln(1 + \text{CV}_X^2) \quad (\text{C.15})$$

For calculation, other parameters can be obtained in the light of the coefficient of variation. Moreover, lognormal distribution is usually applied to the description of variables that can only take positive values.

List of tables

Table 6.1 Parameters for Green and Ampt model.

Table 6.2 Permeability parameters.

Table 6.3 Durations of rainfall events and random variables.

Table B.1 Parameters for Green and Ampt model.

List of figures

Figure 1.1 Two typical idealized rainfall events.

Figure 1.2 Flow chat of the approach developed in this thesis.

Figure 2.1 Failure modes of the soil.

Figure 2.2 Unit slice in an infinite slope.

Figure 2.3 Classical Green and Ampt model.

Figure 2.4 Infiltration process on the unit slice based on Green and Ampt assumptions.

Figure 2.5 Relative hydraulic conductivities in terms of pressure head for silty and sandy soils.

Figure 3.1 Midpoints of the element Ω_i .

Figure 3.2 Realizations of $\log_{10}K_s$ for different scales of fluctuation.

Figure 3.3 Random rainfall generation process by means of the break down coefficient concept.

Figure 3.4 One realization of a random rainfall event with $N = 5$ downscaling steps and total duration $2^N s_0 = 3.2$ hr.

Figure 4.1 The basic slope reliability problem.

Figure 4.2 Transformation from a standard normal space $N(0,1)$ to a uniform distribution $U(0,1)$.

Figure 4.3 Monte Carlo Simulation for estimating the probability of failure.

Figure 4.4 Propagation of failure domain with progression of the wetting front from step 1 to n .

Figure 5.1 Two applications of the adaptive BUS-SuS approach.

Figure 5.2 Contour plots of the logarithm of the likelihood function.

Figure 6.1 The mean wetting front development.

Figure 6.2 Pore water pressure distributions for the realizations of the hydraulic conductivity.

Figure 6.3 Mean factor of safety in terms of wetting front development.

Figure 6.4 Critical slip surface distribution within wetted zone.

Figure 6.5 Probability of failure in terms of wetting front development.

Figure 6.6 One realization of random event with duration 25.6hr.

Figure 6.7 The pore water redistribution in the soil column with different values of the scale of fluctuation r and the standard deviation of saturated hydraulic conductivity in decimal logarithm scale $\sigma_{\log_{10} K_s}$.

Figure 6.8 Pore water pressure at depths of 1m, 2m, 3m and 4m of the soil column, for different scales of fluctuation and $\sigma_{\log_{10} K_s}$, i.e. $r = 0.5$ m, $r = 4$ m, $\sigma_{\log_{10} K_s} = 0.1$ and $\sigma_{\log_{10} K_s} = 0.5$.

Figure 6.9 Mean depth of critical slip surface in function of time, for different scales of fluctuation r and $\sigma_{\log_{10}K_S}$.

Figure 6.10 Realizations of pore water redistribution with different random rainfall events.

Figure 6.11 Comparison of probability of failure in cases with different r .

Figure 6.12 Comparison of probability of failure in cases with different r .

Figure 6.13 Comparison of probability of failure in cases with different a_0 , $H = 0.47$.

Figure 6.14 A rainfall event with duration of 51.2hr.

Figure 6.15 Relative hydraulic conductivities in terms of the pressure head for sandy soils, and the parameters are given by $\alpha = 0.145\text{cm}^{-1}$, $n = 2.68$ (Šimůnek 2009).

Figure 6.16 Pore water pressure redistribution with respect to wetting front development.

Figure 6.17 The posterior distributions of saturated hydraulic conductivities.

Figure 6.18 Pore water pressure obtained by the prior, posterior and measurement.

Figure 6.19 Mean factor of safety.

Figure B.1 Comparison between extended GA model and Richards equation.

References

- Ali A., Huang J., Lyamin A.V., Sloan S.W. and Griffiths D.V. (2014). Simplified quantitative risk assessment of rainfall-induced landslides modelled by infinite slopes. *Engineering Geology*, 179: 102-116.
- Ang A. H. -S. and Tang W. H. (1984). *Probability Concepts in Engineering Planning and Design* (Volume 2). John Wiley & Sons.
- Assouline S. and Ben-Hur M. (2006). Effects of rainfall intensity and slope gradient on the dynamics of inter rill erosion during soil surface sealing. *Catena*, 66(3): 211-220.
- Au S. K. and Beck J. L. (2001). Estimation of small failure probabilities in high dimensions by subset simulation. *Probabilistic Engineering Mechanics*, 16(4): 263-277.
- Au S. K. and Wang Y. (2014). *Engineering Risk Assessment with Subset Simulation*. John Wiley & Sons.
- Beck J. L. and Au S. K. (2002). Bayesian updating of structural models and reliability using Markov chain Monte Carlo simulation. *Journal of Engineering Mechanics*, 128(4): 380-391.
- Beck J. L. and Katafygiotis L. S. (1998). Updating models and their uncertainties. I: Bayesian statistical framework. *Journal of Engineering Mechanics*, 124(4): 455-461.
- Betz W., Papaioannou I. and Straub D. (2014). Numerical methods for the discretization of random fields by means of the Karhunen-Loève expansion. *Computer Methods in Applied Mechanics and Engineering*, 271(0): 109-129.
- Betz W., Beck J. L., Papaioannou I. and Straub D. (2016). Bayesian inference with Subset Simulation: strategies and improvements (working paper).
- Borga M., Dalla Fontana G., Da Ros D. and Marchi L. (1998). Shallow landslide hazard assessment using a physically based model and digital elevation data. *Environmental Geology*, 35(2-3): 81-88.
- Breitung K. (2015). 40 years FORM: Some new aspects? *Probabilistic Engineering Mechanics*, 42: 71-77.
- Caputo J. G. and Stepanyants Y. A. (2008). Front solutions of Richards equation. *Transport in Porous Media*, 74(1): 1-20.
- Chae B. G., Lee J. H., Park H. J. and Choi J. (2015). A method for predicting the factor of safety of an infinite slope based on the depth ratio of the wetting front induced by rainfall infiltration. *Natural Hazards and Earth System Sciences*, 15(8): 1835-1849.
- Chen X. L., Zhou Q., Ran H. and Dong R. (2012). Earthquake-triggered landslides in southwest China. *Natural Hazards and Earth System Science*, 12(2): 351-363.
- Chen L. and Young M. H. (2006). Green-Ampt infiltration model for sloping surface. *Water Resources Research*, 42(7): W07420.

- Cho S. E. and Lee S. R. (2002). Evaluation of surficial stability for homogeneous slopes considering rainfall characteristics. *Journal of Geotechnical and Geoenvironmental Engineering*, 128(9): 756-763.
- Cho S. E. (2007). Effects of spatial variability of soil properties on slope stability. *Engineering Geology*, 92(3): 97-109.
- Cho S. E. (2014). Probabilistic stability analysis of rainfall-induced landslides considering spatial variability of permeability. *Engineering Geology*, 171: 11-20.
- Choi K. Y. and Cheung R. W. M. (2013). Landslide disaster prevention and mitigation through works in Hong Kong. *Journal of Rock Mechanics and Geotechnical Engineering*, 5(5): 354-365.
- Chu X. F. and Marino M. A. (2005). Determination of ponding condition and infiltration into layered soils under unsteady rainfall. *Journal of Hydrology*, 313: 195-207.
- Crăciun A. I., Haidu I., Magyari-Sáska Z. and Imbroane A. I. (2009). Estimation of runoff coefficient according to soil moisture using GIS techniques. *Geographia Technica*, 8(1).
- Christian J. T., Ladd C. C. and Baecher G. B. (1994). Reliability applied to slope stability analysis. *Journal of Geotechnical Engineering*, 120(12): 2180-2207.
- Crosta G. B. and Frattini P. (2003). Distributed modelling of shallow landslides triggered by intense rainfall. *Natural Hazards and Earth System Science*, 3(1/2): 81-93.
- Defersha M. B., Quraishi S. and Melesse A. (2011). The effect of slope steepness and antecedent moisture content on interrill erosion, runoff and sediment size distribution in the highlands of Ethiopia. *Hydrology Earth System Science*, 15: 2367-2375.
- Der Kiureghian A. and Ke, J. -B. (1988). The stochastic finite element method in structural reliability. *Probabilistic Engineering Mechanics*, 3(2): 83-91.
- Dietrich W. E., McKean J., Bellugi D. and Perron T. (2007). The prediction of shallow landslide location and size using a multidimensional landslide analysis in a digital terrain model. *Proceedings of the Fourth International Conference on Debris-flow Hazards Mitigation: Mechanics, Prediction, and Assessment (DFHM-4)*, Chengdu, China.
- Ditlevsen, O. and Madsen H. O. (1996). *Structural Reliability Methods*. John Wiley & Sons.
- Dou H., Han T., Gong X., Qiu Z. and Li Z. (2015). Effects of the spatial variability of permeability on rainfall-induced landslides. *Engineering Geology*, 192: 92-100.
- Enrico C. and Antonello T. (2012). Simplified approach for the analysis of rainfall-induced shallow landslides, *Journal of Geotechnical and Geoenvironmental Engineering*, 138: 398-406.
- Fred T. T. (2011). *Analytical and numerical solutions of Richards equation with discussions on relative hydraulic conductivity*. Chapter 11 in: *Hydraulic Conductivity - Issues, Determination and Applications*. InTech Open Access Publisher.
- Fredlund D. G. (1995). The stability of slopes with negative pore-water pressures. *The Ian Boyd Donald*

- Symposium on Modern Developments in Geomechanics*, Melbourne, Australia.
- Freeze R. A. and Cherry J. A. (1979). *Groundwater*. Prentice Hall.
- García-Mayordomo J., Rodríguez Peces M.J., Azañón J.M. and Insúa Arévalo J.M. (2009). Advances and trends on earthquake-triggered landslide research in Spain. *1st INQUA-IGCP-567 International Workshop on Earthquake Archaeology and Palaeoseismology*, Baelo Claudia, Spain.
- Gardner W. R. (1958). Some steady state solutions of unsaturated moisture flow equations with applications to evaporation from a water table. *Soil Science*, 85(4): 228-232.
- Gelhar L. W. (1986). Stochastic subsurface hydrology from theory to application. *Water Resources Research*, 22(9): 135-145.
- Green W. H. and Ampt G. A. (1911). Studies on soil physics, part I - the flow air and water through soils. *Journal of Agricultural Science*, 4(1): 1-24.
- Griffiths D. V. and Fenton G. A. (2004). Probabilistic slope stability analysis by finite elements. *Journal of Geotechnical and Geoenvironmental Engineering*, 130(5): 507-518.
- Griffiths D. V., Huang J. and Fenton G. A. (2011). Probabilistic infinite slope analysis, *Computers and Geotechnics*, 38(4): 577-584.
- Grigoriu M. (2013). *Stochastic Calculus: Applications in Science and Engineering*. Springer Science & Business Media.
- Lemaire M. (2009). *Structural Reliability*. John Wiley & Sons.
- Malgot J. and Baliak F. (2002). Influence of human activity on the development of landslides in Slovakia. *Geografický časopis*, 54(1): 21-38.
- Menabde M., Seed A., Harris D. and Austin G. (1997). Self-similar random fields and rainfall simulation. *Journal of Geophysical Research*, 102: 509-515.
- Menabde M. and Murugesu S. (2000). Modeling of rainfall time series and extremes using bounded random cascades and Levy-stable distributions. *Water Resources Research*, 36(11): 3293-3300.
- Muntohar A. S. and Liao H. (2010). Rainfall infiltration: infinite slope model for landslides triggering by rainstorm. *Natural Hazards*, 54(3): 967-984.
- Hohenbichler M. and Rackwitz R. (1983). First-order concepts in system reliability. *Structural Safety*, 1(3): 177-188.
- Hohenbichler M. and Rackwitz R. (1988). Improvement of second-order reliability estimates by importance sampling. *Journal of Engineering Mechanics*, 114(12): 2195-2199.
- Horn R. and Johnson C. (1985). *Matrix Analysis* (1st Edition). Cambridge University Press.
- Huang R. Q. and Chan L. S. (2004). Human-induced landslides in China: mechanism study and its implications on slope management. *Chinese Journal of Rock Mechanics and Engineering*, 23(16):

2766-2777.

- Huang F. K., Wang G. S. and Tsai Y. L. (2013). Rainfall reliability evaluation for stability of municipal solid waste landfills on slope. *Mathematical Problems in Engineering*, 2013, 12-21.
- Iverson R. M. (2000). Landslide triggering by rain infiltration. *Water Resources Research*, 36(7): 1897-1910.
- Iverson R. M. and Major J. J. (1986). Groundwater seepage vectors and the potential for hillslope failure and debris flow mobilization. *Water Resources Research*, 22(11): 1543-1548.
- Lan H. X., Zhou C. H., Lee C. F., Wang S. J. and Wu F. Q. (2003). Rainfall-induced landslide stability analysis in response to transient pore pressure: A case study of natural terrain landslide in Hong Kong. *Science in China Series E (Technological Science)*, 46: 52-68.
- Lepore C., Kamal S. A., Shanahan P. and Bras R. L. (2012). Rainfall-induced landslide susceptibility zonation of Puerto Rico. *Environmental Earth Sciences*, 66(6): 1667-1681.
- Leynaud D. and Sultan N. (2010). 3-D slope stability analysis: A probability approach applied to the nice slope (SE France). *Marine Geology*, 269(3-4): 89-106.
- Li C. C. and Der Kiureghian A. (1993). Optimal discretization of random fields. *Journal of Engineering Mechanics*, 119(6): 1136-1154.
- Liu P. L. and Der Kiureghian A. (1986). Multivariate distribution models with prescribed marginals and covariances. *Probabilistic Engineering Mechanics*, 1(2): 105-112.
- Liu J. T., Zhang J. B. and Feng J. (2008). Green–Ampt model for layered soils with nonuniform initial water content under unsteady infiltration. *Soil Science Society of America Journal*, 72(4): 1041-1047.
- Lu N. and Godt J.W. (2008). Infinite slope stability under unsaturated seepage conditions. *Water Resources Research*, 44: W11404.
- Menabde M., Seed A., Harris D. and Austin G. (1997). Self-similar random fields and rainfall simulation, *Journal of Geophysical Research*, 102: 509-515.
- Menabde M. and Murugesu S. (2000). Modeling of rainfall time series and extremes using bounded random cascades and Levy-stable distributions. *Water Resources Research*, 36(11): 3293-3300.
- Muntohar A.S. and Liao H. (2010). Rainfall infiltration: infinite slope model for landslides triggering by rainstorm. *Natural Hazards*, 54(3): 967-984.
- Nataf A. (1962). Détermination des distributions de probabilités dont les marges sont données. *Comptes Rendus de l'Académie des Sciences*, 225: 42-43.
- Nilsson B., Højberg A. L., Refsgaard J. C. and Trolldborg L. (2007). Uncertainty in geological and hydrogeological data. *Hydrology and Earth System Sciences Discussions*, 11(5): 1551-1561.
- Onof C., Chandler R. E., Kakou A., Northrop P., Wheeler H. S. and Isham V. (2000). Rainfall modelling using Poisson-cluster processes: a review of developments. *Stochastic Environmental Research and*

- Risk Assessment*, 14(6): 384-411.
- Orense R. P., Shimoma S., Maeda K., and Towhata I. (2004). Instrumented model slope failure due to water seepage. *Journal of Natural Disaster Science*, 26(1): 15-26.
- Papathoma-Köhle M., Zischg A., Fuchs S., Glade T., and Keiler M. (2015). Loss estimation for landslides in mountain areas - an integrated toolbox for vulnerability assessment and damage documentation. *Environmental Modelling & Software*, 63: 156-169.
- Papaioannou I. (2014). *Lecture notes of stochastic finite element methods*. Engineering Risk Analysis Group, Technische Universität München.
- Papaioannou I., Betz W., Zwirgmaier K. and Straub D. (2015). MCMC algorithms for Subset Simulation. *Probabilistic Engineering Mechanics*, 41: 89-103.
- Papaioannou I., Papadimitriou C. and Straub D. (2016). Sequential importance sampling for structural reliability analysis. *Structural Safety*, 62: 66-75.
- Phoon K. K. and Kulhawy F. H. (1999). Characterization of geotechnical variability. *Canadian Geotechnical Journal*, 36(4): 612-624.
- Perrens S. J. and Watson K. K. (1977). Numerical analysis of two-dimensional infiltration and redistribution. *Water Resources Research*, 13(4): 781-790.
- Petley D. N. (2004). The evolution of slope failures: mechanisms of rupture propagation. *Natural Hazards and Earth System Sciences*, 4(1): 147-152.
- Petley D. N., Higuchi T., Petley D. J., Bulmer M. H. and Carey J. (2005). Development of progressive landslide failure in cohesive materials. *Geology*, 33(3): 201-204.
- Petley D. (2012). Global patterns of loss of life from landslides. *Geology*, 40(10): 927-930.
- Rackwitz R. (2001). Reliability analysis - a review and some perspectives. *Structural Safety*, 23: 365-395
- Rahardjo H., Lee T. T., Leong E. C. and Rezaur R. B. (2005). Response of a residual soil slope to rainfall. *Canadian Geotechnical Journal*, 42(2): 340-351.
- Ray R. L., Jacobs J. M. and De Alba P. (2010). Impacts of unsaturated zone soil moisture and groundwater table on slope instability. *Journal of Geotechnical and Geoenvironmental Engineering*, 136(10): 1448-1458.
- Rawls W. J., Brakensiek D. L. and Saxton K. E. (1982). Estimation of soil water properties. *Transactions of the American Society of Agricultural Engineers*, 25(5): 1316-1320 & 1328.
- Rawls W., Brakensiek D. L. and Miller N. (1983). Green-Ampt infiltration parameters from soils data. *Journal of Hydraulic Engineering*, 109(1): 62-70.
- Richards L. A. (1931). Capillary conduction of liquids through porous mediums. *Physics*, 1(5): 318-333.

- Sahis M. K., Bhattacharya G., and Chowdhury R. (2014). Reliability analysis of rainfall induced slope instability of unsaturated soil slopes. Chapter 173 in: *Unsaturated Soils: Research & Application*, CRC Press.
- Santoso A. M., Phoon K. K. and Quek S. T. (2011a). Effects of soil spatial variability on rainfall-induced landslides. *Computers and Structures*, 89(11-12): 893-900.
- Santoso A. M., Phoon K. K. and Quek S. T. (2011b). Effect of 1D infiltration assumption on stability of spatially variable slope. *Georisk*, 2011: 704-711.
- Schuster R. L., Salcedo D. A. and Valenzuela L. (2002). Overview of catastrophic landslides of South America in the twentieth century. *Reviews in Engineering Geology*, 15: 1-34.
- Šimůnek J., Šejna M., Saito H., Sakai M. and van Genuchten M.Th. (2009). *The HYDRUS-1D Software Package for Simulating the One-Dimensional Movement of Water, Heat, and Multiple Solutes in Variably-Saturated Media* (Version 4.08). Department of Environmental Sciences, University of California Riverside.
- Skaggs T. H. and Barry D. A. (1997). The first-order reliability method of predicting cumulative mass flux in heterogeneous porous formations. *Water Resource Research*, 33: 1485-1494.
- Straub D. and Papaioannou I. (2014). Bayesian analysis for learning and updating geotechnical parameters and models with measurements. Chapter 5 in: *Risk and Reliability in Geotechnical Engineering*, CRC Press.
- Straub D. and Papaioannou I. (2015). Bayesian updating with structural reliability methods. *Journal of Engineering Mechanics*, 141(3): 04014134.
- Straub D., Papaioannou I. and Betz W. (2016). Bayesian analysis of rare events. *Journal of Computational Physics*, 314: 538-556.
- Swain S. (1984). Handbook of stochastic methods for physics, chemistry and the natural sciences. *Journal of Modern Optics*, 31(9): 977-978.
- Terzaghi K., Peck R. B. and Mesri G. (1996). *Soil Mechanics in Engineering Practice*. John Wiley & Sons.
- Tofani V., Segoni S., Agostini A., Catani F. and Casagli N. (2013). Technical note: use of remote sensing for landslide studies in Europe. *Natural Hazards and Earth System Sciences*, 13: 299-309.
- Tokdar S. T. and Kass R. E. (2010). Importance sampling: a review. *Wiley Interdisciplinary Reviews: Computational Statistics*, 2: 54-60.
- Ugai K. and Leshchinsky D. (1995). Three-dimensional limit equilibrium and finite element analysis: a comparison of results. *Soils and Foundations (Japanese Geotechnical Society)*, 35(4): 1-7.
- Van Genuchten M. Th. (1980). A closed-form equation for predicting the hydraulic conductivity of unsaturated soils. *Soil Science Society of America Journal*, 44: 892-898.
- Vanmarcke E. H. 1983. *Random Fields: Analysis and Synthesis*. MIT Press.

- Vogel T., Gerke H. H., Zhang R. and Van Genuchten M. Th. (2000). Modeling flow and transport in a two-dimensional dual-permeability system with spatially variable hydraulic properties. *Journal of Hydrology*, 238: 78-89.
- Wu L. Z., Huang R. Q. and Xu Q. (2012). Incorporating hysteresis in one-dimensional seepage modeling in unsaturated soils. *KSCE Journal of Civil Engineering*, 16(1): 69-77.
- Wu T. H. and Abdel-Latif M. A. (2000). Prediction and mapping of landslide hazard. *Canadian Geotechnical Journal*, 37(4): 579-90.
- Yeh H. F., Lee C. C. and Lee C. H. (2008). A rainfall-infiltration model for unsaturated soil slope stability. *Journal of Environmental Engineering Management*, 18(4): 261-268.
- Yuan J., Papaioannou I., Mok C. M. and Straub D. (2013). Reliability analysis of infinite slope under intense rainfall considering soil variability. *International Symposium on Geotechnical Safety and Risk 2013 (ISGSR 2013)*, Hong Kong, China.
- Yuan J., Papaioannou I., Mok C. M. and Straub D. (2015a). Reliability analysis of infinite slope under intense rainfall considering soil variability. *Georisk*, 2015 (submitted paper).
- Yuan J., Papaioannou I., Mok C. M. and Straub D. (2015b). Reliability analysis of infinite slope under random rainfall events. *International Symposium on Geotechnical Safety and Risk 2015 (ISGSR 2015)*, Rotterdam, Holland.
- Zarba R. L., Bouloutas E. T. and Celia M. (1990). General mass-conservative numerical solution for the unsaturated flow equation. *Water Resources Research*, 26(7): 1483-1496.
- Zhang J., Chen H. Z., Huang H. W. and Luo Z. (2015). Efficient response surface method for practical geotechnical reliability analysis. *Computers and Geotechnics*, 69: 496-505.
- Zhang L. L., Zhang L. M. and Tang W. H. (2005). Rainfall-induced slope failure considering variability of soil properties. *Géotechnique*, 55(2): 183-188.
- Zhang K., Cao P. and Bao R. (2013). Progressive failure analysis of slope with strain-softening behavior based on strength reduction method. *Journal of Zhejiang University-Science A (Applied Physics & Engineering)*, 14(2): 101-109.
- Zhan T. and Ng C. (2004). Analytical analysis of rainfall infiltration mechanism in unsaturated soils. *International Journal of Geomechanics*, 4(4): 273-284.
- Zlotnik V. A., Wang T. J., Nieber J. L. and Šimunek J. (2007). Verification of numerical solutions of the Richards equation using a traveling wave solution. *Advances in Water Resources*, 30: 1973-1980.